Fall 2008

Three-dimensional laminar and turbulent convection in separated flow

Magesh Thiruvengadam
Missouri University of Science and Technology, mtwv8@mst.edu

Department: Mechanical and Aerospace Engineering

THREE-DIMENSIONAL LAMINAR AND TURBULENT CONVECTION IN SEPARATED FLOW

by

MAGESH THIRUVENGADAM

A DISSERTATION

Presented to the Faculty of the Graduate School of the

MISSOURI UNIVERSITY OF SCIENCE AND TECHNOLOGY

In Partial Fulfillment of the Requirements for the Degree

DOCTOR OF PHILOSOPHY

IN MECHANICAL ENGINEERING

2008

Approved by

B. F. Armaly, Advisor
K. O. Homan
K. M. Isaac
H. L. Tsai
S. L. Clark

PUBLICATION DISSERTATION OPTION

This dissertation has been prepared in the form of five papers for publication as follows:

Pages 5-41 have been published in INTERNATIONAL JOURNAL OF HEAT AND MASS TRANSFER.

Pages 42-72 have been published in the ASME JOURNAL OF HEAT TRANSFER.

Pages 73-107 have been submitted in INTERNATIONAL JOURNAL OF HEAT AND MASS TRANSFER.

Pages 108-154 are intended for submission to the INTERNATIONAL JOURNAL OF HEAT AND MASS TRANSFER.

Pages 155-179 have been submitted in ENGINEERING APPLICATIONS OF COMPUTATIONAL FLUID MECHANICS.

ABSTRACT

Three-dimensional laminar and turbulent separated flow and heat transfer in plane symmetric sudden expansion and plane backward facing step is examined in this dissertation. In Papers I, II, and III, simulations of 3-D laminar forced convection in plane symmetric expansion is studied. Flow bifurcation could develop in this geometry under specific flow and thermal conditions causing asymmetric temperature and heat transfer distributions in a symmetric geometry with symmetric inlet flow conditions. In Paper I, the forced convection case is examined to establish the critical Reynolds number range; and in Paper II, the mixed convection case is examined to establish the critical wall heat flux range for which bifurcation exists in this geometry. In Paper III, the mixed convection is examined in the symmetric flow regime that also develops in this geometry at higher heating or flow conditions. The results in Papers I and II demonstrate that the maximum Nusselt number on one stepped wall is larger than the one on the other stepped wall. The results in Paper III demonstrate that the recirculation flow regions downstream from the sudden expansion can disappear from the flow when the wall heat flux is increased. In Paper IV, 3-D turbulent flow measurements using Laser Doppler Velocimeter are made in a backward facing step flow and the three velocity components and the Reynolds stresses are measured in the separated and redeveloping flow region. These measurements can be used as benchmark in developing improvements to existing 3-D turbulence models. In Paper V, the 2-D behavior of a thin film that is shear driven by turbulent air flow is simulated. Film thickness decreases but its surface velocity increases with increasing air flow rate, but film thickness increases and surface velocity increases for increasing liquid flow rates. Results compare favorably with measurements.

ACKNOWLEDGMENTS

I wish to express my sincere thanks and deep sense of gratitude to my advisor Dr. Bassem F. Armaly for his invaluable guidance, advice, financial support, constant encouragement, generous help and keen interest showered on me throughout the course of my research work. I am greatly indebted to him for his unwavering commitment, thought provoking discussions and constructive comments to improve my work.

I would like to thank my committee members Dr. Homan, Dr. Isaac, Dr. Tsai and Dr. Clark for their constructive suggestions, encouragement and for their invaluable time and efforts in examining the dissertation.

I wish to express my profound gratitude and sincere thanks to Dr. Drallmeier for his advice and generous help during the research work.

I would also like to thank the staff of the Department of Mechanical Engineering at Missouri S&T for their support in completing the research work.

I would like to acknowledge the Department of Energy and National Science Foundation for supporting this research. I would also like to acknowledge the financial support that I received in the form of Graduate Research Assistantship and Graduate Teaching Assistantship.

Finally, I want to thank my family and friends for their support and interest during the course of my research.

TABLE OF CONTENTS

LIST OF ILLUSTRATIONS

PAPER IV

LIST OF TABLES

1. INTRODUCTION

Flow separation and its subsequent reattachment occurs when there is a sudden expansion in the geometry in both internal and external flow applications like electronic cooling equipment, cooling of turbine blades, combustion chambers and other heat exchanging devices. The flow and heat transfer in these devices exhibit three-dimensional (3-D) behavior but most of the published results deals only with the two-dimensional (2-D) flow geometry. In the present work the 3-D nature of the flow and heat transfer in separated flow is examined by considering two different geometries. The first being the plane symmetric sudden expansion and the second being the plane backward facing step. These particular geometries are relatively simple but they contain all the significant features of other more complex flow and they appear in many applications where heat exchange is taking place. What is learned from these simple geometries can be translated directly to other more complex geometries. The 3-D behavior in these geometries exposes new features that do not appear in 2-D geometries and make the results more relevant to real applications that are mostly three dimensional in nature. Results from these studies can be utilized as benchmark for model development and verification and for improving preliminary designs of heat transfer equipment. For example; the presence of bifurcation in these heat exchanging devices results in non-uniform heat transfer distribution with Nusselt numbers that are significantly higher than the symmetric 2-D flow results and that needs to be accounted for in the design of such equipment in order to prevent/reduce failure.

In the case of the plane symmetric sudden expansion geometry, experimental [1-4] and numerical [3-6] studies have shown symmetric steady laminar flow behavior for Reynolds number lower than a critical value and asymmetric steady laminar flow behavior for Reynolds number higher than a critical value. The majority of published results for this geometry deal with the isothermal two-dimensional flow case. Tsui and Shu [7] and Alimi et al. [8] performed numerical simulations of laminar mixed convection in a 2D plane symmetric sudden expansion geometry. Flow bifurcations and its effects on 3-D laminar forced and mixed convection regimes in this geometry have not been reported in the literature. The only 3-D heat transfer results (forced convection) in

this geometry are limited to the laminar non-bifurcated flow regime reported by Nie and Armaly [9]. Simulations of 3-D bifurcated flow in this geometry are performed for both laminar forced and laminar mixed convection and the influence of such bifurcation on the distributions of the Nusselt number and the friction coefficient are reported. The simulations establish and document the critical Reynolds number for bifurcated flow in the case of laminar forced convection in a duct with a given expansion and aspect ratio, and the critical heat flux that ends the bifurcated flow regime in the case of laminar mixed convection in a duct for a given Reynolds number, expansion and aspect ratio.

For the case of the plane backward-facing step geometry, extensive experimental and numerical studies have been published for 2-D laminar and turbulent flow but to a much lesser extent on 3-D flow and heat transfer. Simulations and measurements of 3-D laminar flow and heat transfer in this geometry have been published by Armaly et al. [10], Nie and Armaly [11, 12] and Li [13] and in references cited in these publications. Very limited 3-D mean turbulent flow measurements have been reported by Nie and Armaly [14]. Measurements and simulations of turbulent flow (three velocity components and their Reynolds stresses) are reported in this dissertation.

The broad objectives of this dissertation are the following:

i) Studying, through numerical simulations, flow bifurcation and its influence on heat transfer in 3-D plane symmetric sudden expansion for laminar, forced and mixed convection flow regimes.

ii) Measuring and simulating the 3-D separated turbulent flow adjacent to plane backward-facing step and reporting the results for the three velocity components and their Reynolds stresses.

The other topic that is discussed in this dissertation is 2-D flow of thin liquid film that is shear driven by turbulent air flow in a duct. In this work the thickness and the velocity distribution in thin liquid film are simulated for different air flow rates and different liquid flow rates and compared with the measured results of Wittig et al [15].

The simulation phase of the work utilized the commercial computational fluid dynamics (CFD) code FLUENT 6.2. Mesh is generated using FLUENT's preprocessor GAMBIT. The appropriate governing steady-state Navier-Stokes, energy and continuity equations for incompressible flow are utilized in these simulations. The Reynolds Stress

Model, AKN low Reynolds number model and SST k-ω turbulence models are utilized when simulating turbulent flow. For the measurement phase of this work a three-component Laser Doppler Velocimeter (LDV) is used to measure the three-velocity components and their turbulent fluctuations as needed in the flow regime.

This dissertation is divided into five papers. Paper I, II and III deal with the studies of laminar flow and heat transfer in plane symmetric sudden expansion. Paper IV is concerned with the measurements and predictions of laminar and turbulent flow adjacent to plane backward facing step. Paper V is concerned with the simulation of the shear driven liquid film in a duct.

Paper I presents the simulations of bifurcated 3-D forced convection in a horizontal duct with plane symmetric sudden expansion. The geometry has an expansion ratio (ER) of 2 and an upstream aspect ratio (AR) of 4. The effect of bifurcation on flow and heat transfer is examined for the Reynolds number of 400-800. Uniform and constant wall heat flux of 5 W/m^2 is applied on the two stepped walls and all the other walls are treated as adiabatic surfaces. The buoyancy effect on the flow is assumed to be negligible for this value of heat flux. The general three dimensional flow features that develop downstream from the sudden expansion, distributions of reattachment lines, Nusselt number and friction coefficient are reported and discussed.

Paper II is an extension of the paper I and deals with the study of 3-D laminar mixed convection in a vertical duct with plane symmetric sudden expansion in the bifurcated flow regime. The geometry is similar to the one reported in paper I but is placed in vertical orientation for buoyancy assisting flow. The Reynolds number of the flow is fixed at Re = 800 and uniform wall heat flux is applied on the two stepped walls while the other walls are treated as adiabatic surfaces. The magnitude of uniform wall heat flux on the stepped walls is varied for a given aspect ratio to examine the effect of buoyancy assisting force on the reattachment lines, Nusselt number and friction coefficient. Similarly the duct's aspect ratio is varied and its effect on the results is examined for a given wall heat flux on the stepped walls. The critical wall heat flux above which bifurcation stops to occur for this Reynolds number for different duct's aspect ratio is established.

Paper III is the continuation of paper II and examines the 3-D laminar mixed convection in the same geometry but in a regime where the flow is symmetric (no bifurcation). The wall heat flux on the two stepped walls for this study is much higher than the critical wall heat flux for bifurcation in the flow to occur in this geometry at Re = 800. Uniform wall heat flux and duct's aspect ratio is varied to examine its influence on the distributions of velocity, temperature, Nusselt number and reattachment line.

Paper IV presents LDV measurements and simulations of 3-D turbulent air flow adjacent to backward facing step in a vertical duct. The backward facing step geometry in the duct has a step height of 1.06 cm with an aspect ratio (AR) of 8.25 and expansion ratio (ER) of 1.91. Reattachment length measurements are reported for different Reynolds number ($300 < Re < 8631$) covering laminar, transition and turbulent flow regimes. Measurements of the three turbulent mean velocity components and their Reynolds stresses along with the turbulent kinetic energy for a Reynolds number of Re = 8631 representing the fully turbulent flow regime for this geometry. Simulations are reported and compared with measurements.

Paper V presents the results of simulating the 2-D fully developed thickness and velocity distribution in a thin liquid film that is shear-driven by turbulent air flow in a duct. The Volume of Fluid Model (VOF) for multi-phase flow that is available in the FLUENT CFD code is used in these simulations. The effects of liquid film flow rate and the air flow rate on the film behavior is reported and compared with existing measured results.

PAPER

I. Bifurcated three-dimensional forced convection in plane symmetric sudden expansion

M. Thiruvengadam, J.H. Nie, B.F. Armaly
Department of Mechanical and Aerospace Engineering
Missouri University of Science and Technology, Rolla, MO 65401, United States
Email: mtwv8@mst.edu, armaly@mst.edu and drallmei@mst.edu

Abstract

Simulations of bifurcated three-dimensional laminar forced convection in horizontal duct with plane symmetric sudden expansion are presented to illustrate the effects of flow bifurcations on temperature and heat transfer distributions. The stable bifurcated flow that develops in this symmetric geometry leads to non-symmetric temperature and heat transfer distributions in the transverse direction, but symmetric distributions with respect to the center width of the duct in the spanwise directions for the Reynolds number of 400 to 800. A strong downwash develops at the corner of the step and a smaller reverse flow region develops adjacent to the lower stepped wall than the one that develops adjacent to the upper stepped wall. The downwash and the "jet-like" flow that develop near the sidewall create a strong swirling spanwise flow in the primary recirculating flow regions downstream from the sudden expansion. The magnitude of maximum Nusselt number that develops on the lower stepped walls is higher than the one that develops on the upper stepped wall. The locations of these maximum Nusselt numbers on the stepped walls are near the sidewalls and are upstream of the "jet-like" flow impingement regions. Results reveal that the locations where the streamwise component of wall shear stress is zero on the stepped walls do not coincide with the outer

edge of the recirculation flow region near the sidewalls. Velocity, temperature, Nusselt number, and friction coefficient distributions are presented.

Nomenclature

AR Upstream aspect ratio = W/h

AR_1 Downstream aspect ratio = W/H

C_f Skin friction coefficient = $2\tau_w / \rho u_0^2$

C_p Specific heat

ER Expansion ratio = H/h

H Duct height downstream from the step

h Duct height upstream from the step

k Thermal conductivity

L Half width of the duct

Nu Nusselt number = $q_w S/k(T_w-T_0)$

q_w Wall heat flux = $-k\partial T/\partial n$ at the wall

Re Reynolds number = $2\rho u_0 h/\mu$

S Step height

T Temperature

T_0 Inlet fluid temperature

u Velocity component in the x- coordinate direction

u_0 Average inlet velocity

v Velocity component in the y- coordinate direction

W Width of the duct

w Velocity component in the z- coordinate direction

x Streamwise coordinate

y Transverse coordinate

z Spanwise coordinate

x_b Outer boundary of the primary recirculation region

x_u Locations where the streamwise velocity gradient is zero ($\partial u / \partial y = 0$)

μ Dynamic viscosity

ρ Density

τ_w Wall shear stress $= \mu\sqrt{(\partial u / \partial y)^2 + (\partial w / \partial y)^2}$ on the stepped wall, and
$= \mu\sqrt{(\partial u / \partial z)^2 + (\partial v / \partial z)^2}$ on the sidewall

1. Introduction

Flow separation and reattachment due to sudden changes in geometry in internal flow occur in many engineering applications where heating or cooling is required. These applications appear in electronic cooling equipment, cooling of turbine blades, combustion chambers, and many other heat exchanging devices. The flow and the heat transfer in most of these applications exhibit three-dimensional (3-D) behavior, but most of the published heat transfer results deals only with the two-dimensional (2-D) behavior. Experimental and numerical studies [1-5] have shown that laminar flow in plane symmetric sudden expansion exhibits symmetric steady laminar flow behaviors for Reynolds number lower than a critical value, and asymmetric steady laminar flow behavior for Reynolds number higher than the critical value. Results have also shown that the flow becomes unsteady as the Reynolds number continues to increase.

Fearn et al. [1] presented the measured and predicted results for flow in a duct with an expansion ratio of 3 and downstream aspect ratio of 8 and determined that the

critical Reynolds number is 108. They observed a laminar and stable bifurcated flow regime for Reynolds number ranging between 108 and 413, and unsteady laminar flow regime for Reynolds number higher than 413. Durst et al. [2] measured streamwise velocity distributions for Re = 75, 152, and 344 in a duct with an expansion ratio of 3 and downstream aspect ratio of 9.2. This range of Reynolds number covered the laminar symmetric flow regime for Re = 75 and the laminar stable bifurcated flow regime for Re = 152 and 344. They demonstrated experimentally that the asymmetry can flip flop from one stepped wall to the other due to disturbances in the inlet flow and instabilities that develop in the separated shear layer. Similarly, Durst et al. [3] measured and predicted results for an expansion ratio of 2 and downstream aspect ratio of 8, and established the critical Reynolds number for this geometry to be 167. Cherdron et al. [4] demonstrated experimentally that the critical Reynolds number increases both with decreasing the aspect ratio and the expansion ratio. They reported critical Reynolds numbers as a function of downstream aspect ratio for expansion ratios of 2 and 3. Hawa and Rusak [5] used asymptotic linear instability analyses, and numerical simulations to study in details the dynamics and the instabilities of the bifurcated 2-D flow in this geometry. Battaglia et al. [6] demonstrated numerically that the critical Reynolds number is a function of the expansion ratio (decreases with increasing expansion ratio), and they established that the convergence time of the numerical solution increases significantly as the critical Reynolds number is approached. Drikakis [7] concluded from numerical studies that the critical Reynolds number decreases with the increase of the expansion ratio and the asymmetry increases with the increase of the Reynolds number. Patel and Drikakis [8] demonstrated numerically that the critical Reynolds number is influenced by the

discretization scheme of the advective flux terms that appear in the governing equations and recommended a second or higher order finite difference scheme for accurate simulations. Chiang et al. [9] demonstrated numerically that the critical Reynolds number is a function of the duct's aspect ratio (3-D simulation). They established that for an expansion ratio of 3 and a Reynolds number equal to or smaller than 160, the flow will be symmetric when the upstream aspect ratio is smaller than 3.5. Schreck and Schafer [10] used a parallel multi-grid finite volume solver to simulate 3-D bifurcation in a duct with expansion ratio of 3, and reported critical Reynolds numbers for downstream aspect ratio of 5 and 2. All of the above studies were limited to the isothermal flow case.

Tsui and Shu [11] examined numerically the 2-D laminar mixed convection in an inclined duct with an expansion ratio of 3. The buoyancy assisted flow, with vertical orientation, remained symmetric for $Re \leq 75$ and Grashof numbers in the range of 1000 - 3000 (where the Grashof number is based on the upstream duct height and the walls-inlet flow temperature difference). When the Reynolds number increased to 152 (thus lowering the buoyancy force), the flow field was either symmetric or asymmetric depending on the magnitude of the Grashof number. The buoyancy opposing flow resulted in a wavy non-symmetric structure with several recirculation flow regions that increased the heat transfer. Nie and Armaly [12] examined numerically the three-dimensional forced convection in a duct with expansion ratio of 2 and upstream aspect ratio of 4, but that study was limited to Reynolds number below the critical value, i.e. symmetric flow regime.

The majority of published results for plane symmetric sudden expansion in a duct have dealt with the isothermal two-dimensional flow case. To the authors' knowledge the

only published three-dimensional heat transfer results have been limited to the non-bifurcated flow regime [12]. This fact, along with the realization that such geometry appears regularly in many industrial heat transfer devices, motivated the present study.

2. Problem statement and solution procedure

Three-dimensional laminar forced convection in a horizontal duct with a plane symmetric sudden expansion is simulated, and a schematic of the computational domain is presented in Fig.1. The duct's heights (H) and (h) downstream and upstream of the expansion respectively are 0.04m and 0.02m. The step height (S) and the duct's width (W) are maintained as 0.01m and 0.08m respectively. This geometry provides a configuration with an expansion ratio ($ER = H/h$) of 2, an upstream aspect ratio ($AR = W/h$) of 4, and a downstream aspect ratio ($AR_1 = W/H$) of 2. The origin of the coordinate system is located at the bottom corner of the step where the sidewall, the backward-facing step and the lower stepped-wall intersect, as shown in Fig. 1. The directions of the streamwise (x), spanwise (z), and transverse (y) coordinates are shown in that figure. The length of the computational domain is 0.8m downstream and 0.02m upstream of the step, respectively, i.e. $-2 \le x/S \le 80$. This choice was made to insure that the flow at the inlet section of the duct ($x/S = -2$) is not affected by the sudden expansion in geometry, and the flow at the exit section of the duct ($x/S = 80$) can be treated as fully developed. It was confirmed that the use of a longer computational domain did not change the flow or the thermal behavior in the region downstream from the step ($x/S < 40$). The three-dimensional steady, and also the transient Navier-Stokes, energy, and continuity equations for laminar incompressible flow are solved numerically using the finite volume method. The physical properties are treated as constants and evaluated for air at the inlet

temperature of $T_0 = 20^{\circ}C$ (i.e., density (ρ) is 1.205 kg/m^3, specific heat (C_p) is 1005 J/Kg.^{o}C, dynamic viscosity (μ) is 1.81x10^{-5} kg/m.s, and thermal conductivity (k) equals to 0.0259W/m.^{o}C). Inlet flow (x/S = -2, $1 \le y/S \le 3$, for all z) is considered to be isothermal ($T_0 = 20^{\circ}C$), hydrodynamically steady and fully developed with a distribution for the streamwise velocity component (u) equal to the one described by Shah and London [13]. The other velocity components (v and w) are set to be equal to zero at that inlet section. The no-slip boundary condition (zero velocities) is applied to all of the wall surfaces. Uniform and constant wall heat flux (q_w = 5W/m^2) is specified for the stepped walls (y/S = 0 and 4, $0 \le x/S \le 80$, for all z), while other walls are treated as adiabatic surfaces. At this low wall heat flux and for this horizontal orientation of the duct, the buoyancy effects can be, and was, neglected in the simulations. Fully developed flow and thermal conditions are imposed at the exit section (x/S = 80, for all y and z) of the calculation domain.

Numerical solution of the governing equations and boundary conditions was performed by utilizing the commercial computational fluid dynamics (CFD) code FLUENT 6.0. The mesh is generated using FLUENT's preprocessor GAMBIT. Hexahedron volume elements were used in the simulation. At the end of each iteration, the residual sum for each of the conserved variables was computed and stored, thus recording the convergence history. The convergence criterion required that the scaled residuals be smaller than 10^{-10} for the mass and the momentum equations and smaller than 10^{-11} for the energy equation. Calculations were performed on DELL workstations, and the CPU time for converged solution for Re = 600 is approximately 24 hours. The SIMPLEC algorithm is used for the pressure velocity coupling, and the momentum and

energy equations are discretized with the Second Order Upwind scheme in order to improve the accuracy of the simulations. Detailed descriptions of the CFD code and the solution procedures may be found in the FLUENT manual.

3. Code and model validations

Numerical simulations of the velocity and temperature distribution in this geometry revealed a symmetric behavior relative to the center width of the duct as can be seen in Figs. 2 and 3 for $Re = 600$. The results in these figures show that the velocity and temperature distributions are symmetric in the spanwise direction and un-symmetric in the transverse direction. As a result of the spanwise symmetry, the width of the computational domain is chosen as half of the actual width of the duct, $L = 0.04$m, and symmetry boundary conditions are applied at the center plane of the duct, i.e. at $z = 0.04$m, $w = 0$, and the gradient of all the other quantities with respect to z are set equal to zero. Results that were generated using this smaller domain (half width) compared exactly with the results that were generated using the full width domain.

The computational grid distribution was selected to ensure high density near all of the bounding walls and in the regions of the step where high gradients exist, in order to ensure the accuracy of the simulations. Grid independence tests were performed using eight different grid densities and distributions downstream of the sudden expansion for $Re = 600$. Comparisons of these results show that using a grid of (200 x 64 x 50) downstream of the sudden expansion ($0 \le x/S \le 80$) and a grid of (20 x 32 x 50) upstream of the sudden expansion ($-2 \le x/S \le 0$) for half of the duct's width ($0 \le z/L \le 1$) provides a grid independent results, and this grid was used for all the results that are presented in this paper.

The use of both the steady and the transient Navier-Stokes equations for simulating the steady bifurcated flow that develops in this geometry was examined. The distributions of the resulting steady streamwise velocity component simulated by these two schemes were compared for Re = 800, and the excellent agreements between the results from the two simulation schemes (steady and transient) justify the use of the steady Navier-Stokes equations for simulating the steady bifurcated flow regime. Our predicted distributions for the streamwise velocity component in the same geometry as the one used in the experiment by Fearn et al. [1] compare very favorably with his published measurements, thus validating the accuracy of the simulation code.

4. Results and discussion

Simulations of the flow and heat transfer were performed for Reynolds numbers of 150, 350, 400, 450, 600, and 800 in the geometry that is presented in Fig. 1. The flow at these Reynolds numbers is laminar and steady with flow bifurcation developing for Re > 400, and symmetric non-bifurcated flow developing for Re < 400. This study will focus on presenting flow and heat transfer results in the bifurcated flow regime (Re > 400). The bifurcated flow that developed in our simulations resulted in stable bifurcated states where the reverse flow region that develops adjacent to the lower stepped wall is smaller than the one that develops adjacent to the upper stepped wall. Due to space limitations and due to the fact that the results are similar for different Reynolds numbers, most of the presented results are for Re = 600. Results for other Reynolds numbers are presented, when warranted, to illustrate the effects of the Reynolds number.

The general flow features that develop downstream from the sudden expansion are presented in Fig. 4 for Re = 600. A primary recirculation flow region develops

adjacent to the lower stepped wall and a larger recirculation flow region develops adjacent to the upper stepped wall. A third but smaller recirculation flow region develops further downstream on the lower stepped wall but that reverse flow region exists only close to the sidewall and does not extend to the center of the duct as can be seen in Fig. 4*c*. A downwash and several "jet-like" flow regions develop adjacent to the sidewall. The downwash flows in a counter-clockwise swirling motion towards the lower stepped wall and into the primary reverse flow region while moving in the spanwise direction toward the center of the duct. Three "jet-like" flow impingement regions can be seen in Fig. 4*a*, with one on the upper stepped wall (at $x/S = 29.24$, $z/L = 0.185$) and two on the lower stepped wall (at $x/S = 5.684$, $z/L = 0.165$, *and* $x/S = 32.0$, $z/L = 0.039$). A reverse flow region develops in the neighborhood of each impingement region as can be seen in Fig. 4*a*. Streamlines at different spanwise planes are presented in Fig. 4*c* to demonstrate the flow behavior near the sidewall. The general flow features that develop in the region of $0.20 < z/L < 1$ (close to the center of the duct) do not change significantly, and for that reason are not represented in Fig. 4*c*. Similar results are available for other Reynolds numbers but are not presented due to space limitations. The locations of the "jet-like" flow impingement for $Re = 450$ on the lower stepped wall are $x/S = 7.426$, $z/L = 0.311$, and on the upper stepped wall they are at $x/S = 17.475$, $z/L = 0.346$. The locations of the "jet-like" flow impingement for $Re = 800$ on the lower stepped wall are $x/S = 5.403$, $z/L = 0.130$, and $x/S = 43.171$, $z/L = 0.042$, and on the upper stepped wall they are at $x/S = 38.844$, $z/L = 0.129$.

Limiting streamlines adjacent to the upper stepped wall, lower stepped wall and sidewall are presented in Fig. 5 to illustrate additional flow features downstream of the

sudden expansion. There are two "jet-like" flow impingement locations that appear on the lower stepped wall and one that appear on the upper stepped wall as was discussed in the previous paragraph but can be seen more clearly in this figure for Re = 600. At these points, the streamwise and the spanwise components of the wall shear stress, $(\mu\partial u/\partial y)$ and $(\mu\partial w/\partial y)$, are zero. The impingement point acts as a source from which streamlines originate. Some of these streamlines flow downstream and later reverses their direction while moving toward the sidewall and in that process a reverse flow region develops adjacent to the sidewall as can be seen in Fig. 5. The saddle points that develop on the lower stepped wall and on the sidewall represent critical points in the flow where two streamlines approach that point from different angles and rebound to form the boundaries of four different flow regions around the saddle point. The three Focal points that develop on the sidewall represent critical points in the flow where infinite number of streamlines spiral around. Two of these focal points are attractive and one is repelling. The repelling focal point is the one located farthest downstream from the sudden expansion as shown in Fig. 5. The bold solid lines that are shown in Fig. 5 represent the locations where the streamwise component of the wall shear stress $(\mu\partial u/\partial y)$ is zero (x_u-line) for the two stepped walls and $(\mu\partial u/\partial z)$ is zero for the sidewall.

Distributions of the x_u-lines are presented in Fig. 6 for both y/S = 0.01 and 3.99 (the two stepped walls). The locations of the saddle points and the "jet-like" flow impingement points are included on this figure. This definition (x_u-line) is commonly used to identify the reattachment length in two-dimensional separated-reattached flow. The x_u-line moves further downstream as the Reynolds number increases and its maximum develop at the sidewall for both the upper and the lower stepped walls. A

minimum develops in the x_u-line on the lower stepped wall near the sidewall and that minimum moves closer to the sidewall and closer to the step as the Reynolds number increases, i.e. behaving in a similar fashion as to the impingement location of the "jet-like" flow. It is interesting to note that in the center region of the duct $0.8 < z/L < 1.0$ the effect of the Reynolds number on the x_u-line for the lower wall is negligible. Two "jet-like" flow impingement regions develop on the lower stepped wall for $Re = 600$ and 800, but only one develops for $Re = 450$.

The limiting streamlines that are presented in Fig. 5 are also used to identify the outer boundary of the recirculation regions (x_b-lines) that develop adjacent to the bounding walls. These boundary lines, (x_b-lines) are determined by the criterion that streamlines on both sides of these boundary lines move in opposite directions: streamlines upstream from this line flow upstream toward the step, and streamlines downstream from this line flow downstream and away from the step. Distributions of the x_b-lines on the planes of $y/S = 0.01$ and 3.99 adjacent to the two stepped walls are presented in Fig. 7. The x_b-line differs from the x_u-line for three-dimensional flow (especially near the sidewall), but they are identical to each other for two-dimensional flow (i.e. at the center of a duct with large aspect ratio). The x_b-lines on the upper stepped wall move further downstream from the step as the Reynolds number increases. It is interesting, however, to note that in the center region of the duct ($0.8 < z/L < 1.0$) the effect of the Reynolds number on the x_b-line for the lower stepped wall is negligible, but near the sidewall the x_b-lines on the lower stepped wall move upstream or closer to the step as the Reynolds number increases. Two separated reverse flow regions develop for $Re = 800$, but only one develop for $Re = 450$ and 600.

Transverse distributions of velocity and temperature at different streamwise locations are presented in Fig. 8 for Re = 600. These figures illustrate the non-symmetric behaviors that develop in these distributions inside this symmetric geometry. The non-symmetric behaviors that appear in the bifurcated flow region disappear in the fully developed flow. In the bifurcated flow region the distribution of streamwise velocity component tilts towards the wall that has the smaller reverse flow region (the lower stepped wall in this case). This asymmetric flow behavior leads to a lower fluid temperature in that region, and to asymmetric temperature distribution. These features influence the magnitude and the distribution of the Nusselt number on the stepped walls.

Distributions of the velocity and temperature fields are presented in Fig. 9 for those streamwise intersectional planes where the "jet-like" flow impinges on the lower and upper stepped walls. The velocity vectors in this figure represent the sum of the transverse and spanwise velocity components. The wall temperature decreases and the spanwise velocity component increases in the "jet-like" flow impingement regions. It is interesting to note that the lower stepped wall is at a lower temperature than the upper stepped wall at x/S = 5.684 (where the "jet like" flow impinges on the lower wall), and also at x/S = 29.24 (where the "jet-like" flow impinges on the upper wall).

Results in Fig. 10 represent the velocity field on a plane adjacent to the lower stepped wall (y/S = 0.01). The velocity vectors in this figure represent the sum of the spanwise and streamwise velocity components and the color in this figure represents the magnitude of the transverse (normal) velocity component. The locations where "jet-like" flow impinges on the stepped wall and the location where the Nusselt number is a maximum are identified in this figure. It can be seen that the location of the maximum

Nusselt number does not coincides with the location where the "jet-like" flow impinges on this stepped wall. The x_u-line is also presented in this figure, and it passes through a region where the transverse velocity component is positive near the sidewall, thus indicating that the x_u-line in that region of the flow does not represent a reattachment of the separating shear layer on the stepped wall. It is also interesting to note that the location where the maximum Nusselt number develops on the stepped wall is in the same region where the magnitude of the transverse velocity component is a maximum.

Results in Fig. 11 represent the velocity field on a plane adjacent to the upper stepped wall (y/S = 3.99). The location where "jet-like" flow impinges on this stepped wall and the location where the Nusselt number is a maximum are identified in this figure. The location of the maximum Nusselt number is significantly upstream from the "jet-like" impingement location, inside the primary recirculation flow region. The x_u-line is also presented in this figure, and it passes through a region where the transverse velocity component is positive (near the sidewall), thus indicating that the x_u-line in that region of the flow does not represent a reattachment of the separating shear layer. The maximum Nusselt number develops on this stepped wall is in the same general region where the magnitude of the transverse velocity component incident on that wall is a maximum. Results in Fig. 12 represent the velocity field on a plane adjacent to the sidewall (z/L = 0.01). The velocity vectors in this figure represent the sum of the streamwise and transverse velocity components and the color represents the magnitude of the spanwise velocity component. The downwash that develops at the corner of the step can be seen in this figure. The locations of the saddle point and the Focal points that develop on this plane along with the line that locates the minimum temperature on this

plane are identified in this figure. It is interesting to note that the minimum sidewall temperature develops in the general region where the magnitude of the spanwise velocity component (velocity normal to the sidewall) is a maximum.

Nusselt number $(Nu = q_w S / k\left(T_w - T_0\right))$ distributions on the two stepped walls are presented in Figs. 13 and 14 for *Re* = 600. The results show that the maximum Nusselt number develops near the sidewall and not at the center of the duct. The maximum Nusselt number that develops on the lower stepped wall (the wall with the smaller recirculation flow region) is higher than the maximum Nusselt number that develops on the upper stepped wall (the wall with the larger recirculation flow region). Similarly the location of that maximum on the lower stepped wall is significantly closer to the sudden expansion than the one on the upper stepped wall. The spanwise distributions of the Nu_{max}-line (locations where the Nusselt number is a maximum), and the x_u–line are presented in these figures. The Nu_{max}-line moves further downstream from the step and the maximum Nusselt number moves closer to the sidewall as the Reynolds number increases. The maximum Nusselt numbers on the lower stepped wall are 1.191 (at *x/S* = 4.785*, z/L* = 0.271), 1.813 (at *x/S* = 5.45, *z/L* = 0.248) *and* 2.332 (at *x/S* = 5.728, *z/L* = 0.248) for *Re* = 450, 600 and 800, and on the upper stepped wall they are 0.763 (at *x/S* = 11.377*, z/L* = 0.271), 0.804 (at *x/S* = 15.508*, z/L* = 0.167) and 0.885 (at *x/S* = 27.0*, z/L* = 0.186), respectively. The magnitude of the maximum Nusselt number that develops on the lower stepped wall is larger than the magnitude of the Nusselt number that develops on the upper stepped wall. Similarly, the distance from the sudden expansion where that maximum develops on the upper stepped wall is more than twice the distance that the maximum develops on the lower stepped wall. The results in Figs. 13*b* and 14*b* illustrate

the rapid increase of the Nusselt number to a peak value after the sudden expansion, and that peak develops near the sidewall. The Nusselt number gradually decreases after the peak point as the flow approaches the fully developed region where the location of the maximum Nusselt number gradually moves from the sidewall toward the center of the duct as the streamwise distance from the sudden expansion continues to increase. The second "jet-like" flow that impinges on the lower stepped wall is relatively small in magnitude and for that reason it does not appear to affect significantly the Nusselt number distribution in that region. It should be noted that the Nusselt number is inversely proportional to the wall temperature.

Distributions of the friction coefficient on the two stepped walls are presented in Figs. 15 and 16 for $Re = 600$. These results illustrate that the friction coefficient increases rapidly after the sudden expansion and a maximum develops inside the primary recirculating flow region (upstream of the x_u–line). The location of that maximum is in the center of the duct for the lower stepped wall and closer to the sidewall for the upper stepped wall. The location of the maximum in that region moves farther downstream from the sudden expansion as the Reynolds number increases. The magnitude of the friction coefficient then decreases rapidly to a minimum, and the spanwise locations of that minimum are designated by the x_u–lines that are presented in these figures. The friction coefficient increases rapidly after the x_u–lines, developing a local peak near the sidewall on the lower stepped wall, and a maximum at the center of the duct in the fully developed region. The Nu_{max}-line is presented in these figures to illustrate its relative location as compared with the x_u–line.

Temperature distributions on the sidewall are presented in Fig. 17 for Re = 600. The lack of symmetry relative to the center height of the sidewall near the sudden expansion (in the bifurcated flow region) can be seen in these figures. The temperature distribution is skewed towards the lower stepped wall (the wall with the smaller recirculating flow region), thus creating a lower temperature in that region of the flow. A line identifying the location where the wall temperature is a minimum is included in this figure. The wall temperature increases as the distance from the duct's center increases due to its proximity to the heated stepped walls. Similarly the temperature increases as the distance from the sudden expansion increases due to the added energy from the heated bounding walls. Symmetry develops in the sidewall temperature distribution as the fully developed flow region is approached. Distributions of the friction coefficient on the sidewall are presented in Fig. 18 for Re = 600. Several peaks develop in this distribution and their magnitude decreases as the Reynolds number increases. The local peaks that develop in that distribution and its general streamwise behavior can be seen in Fig. 18*b*.

5. Conclusions

Simulations of three-dimensional laminar forced convection in plane symmetric sudden expansion in rectangular duct with an expansion ratio of two and downstream aspect ratio of two are presented for Re = 450, 600 and 800. The bifurcated flow for this Reynolds number range is laminar, steady and asymmetric in the transverse directions, but symmetric relative to the center width of the duct in the spanwise direction. A strong downwash develops at the corner of the step near the sidewall causing the reverse flow region that develops adjacent to the lower stepped wall to be smaller than the one that develops adjacent to the upper stepped wall. The "jet-like" flow that impinges on the

lower stepped wall originates from the top corner of the inlet section, but that flow develops a reversed spiral flow region adjacent to the sidewall before its impingement on the lower stepped wall. The maximum Nusselt number that occurs on the lower stepped wall is larger than the one that develops on the upper stepped walls. The maximum Nusselt number develops near the sidewall and not at the center of the duct. Its location on the lower stepped wall is closer to the sudden expansion than its location on the upper stepped wall. The maximum Nusselt numbers on the stepped walls do not develop at the impingement location of the "jet-like" flow, but in the region where the magnitude of the transverse velocity component incident on the wall is a maximum. The second "jet-like" flow impingement on the lower stepped walls has little effect on the Nusselt number distribution due to its relatively very small magnitude. The friction coefficient is slightly higher on the lower stepped wall in comparison with the upper stepped wall in the bifurcated flow region. The results also reveal that the locations where the streamwise component of wall shear stress is zero on the stepped walls (x_u–line) do not coincide with the outer edge of the primary recirculation flow region (x_b-lines) near the sidewalls.

Acknowledgement

This work was supported in part by a DOE-Basic Energy Sciences Grant No. DE-FG02-03ER46067.

References

[1] R.M. Fearn, T. Mullin, K.A. Cliffe, Nonlinear flow phenomena in a symmetric sudden expansion, J. Fluid Mech. 211 (1990) 595-608.

[2] F. Durst, A. Melling, J.H. Whitelaw, Low Reynolds number flow over a plane symmetric sudden expansion, J. Fluid Mech. 64 (1974) 111-128.

[3] F. Durst, J.C.F. Pereira, C. Tropea, The plane symmetric sudden-expansion flow at low Reynolds numbers, J. Fluid Mech. 248 (1993) 567-581.

[4] W. Cherdron, F. Durst, J.H. Whitelaw, Asymmetric flows and instabilities in symmetric ducts with sudden expansions, J. Fluid Mech. 84 (1978) 13-31.

[5] T. Hawa, Z. Rusak, The dynamics of a laminar flow in a symmetric channel with a sudden expansion, J. Fluid Mech. 436 (2001) 283-320.

[6] F. Battaglia, S.J. Travener, A.K. Kulkarni, C.L. Merkle, Bifurcation of low Reynolds number flows in symmetric channels, AIAA J 35 (1997) 99-105.

[7] D. Drikakis, Bifurcation phenomena in incompressible sudden expansion flows, Phys. Fluids 9 (1997) 76-87.

[8] S. Patel, D. Drikakis, Numerical effects on the prediction of flow instabilities in channels with sudden-expansions, Proceedings of IMECE'03, ASME-IMECE2003-55616, Washington, DC, 2003, pp. 16-21.

[9] T.P. Chiang, T.W.H. Sheu, S.K. Wang, Side wall effects on the structure of laminar flow over a plane-symmetric sudden expansion, Comput. Fluids 29 (2000) 467-492.

[10] E. Schreck, M. Schafer, Numerical study of bifurcation in three-dimensional sudden channel expansions, Comput. Fluids 29 (2000) 583-593.

[11] Y.Y. Tsui, S.J. Shu, Effects of buoyancy and orientation on the flow in a duct with a double-step expansion, Int. J. Heat Mass Transfer 41 (1998) 2687-2695.

[12] J.H. Nie, B.F. Armaly, Three-dimensional forced convection in plane symmetric sudden expansion, ASME J. Heat Transfer 126 (2004) 836-839.

[13] R.K Shah, A.L. London, Laminar Forced Convection in Ducts, Academic Press, New York, 1978, pp. 196-198.

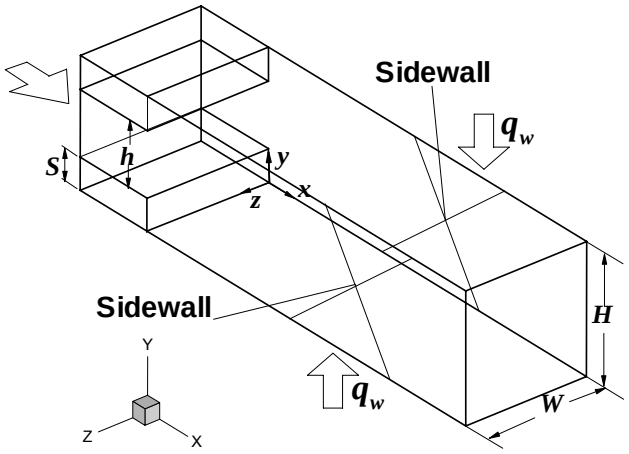

Fig. 1 Schematic of the computational domain

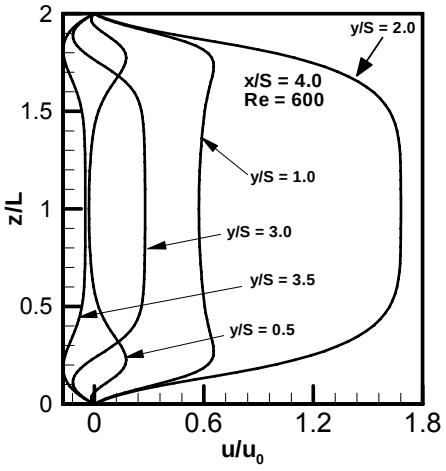

(a)

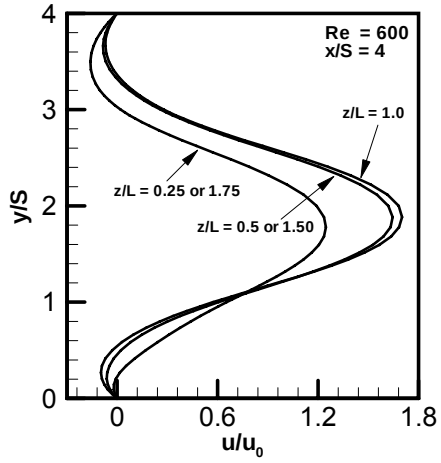

(b)

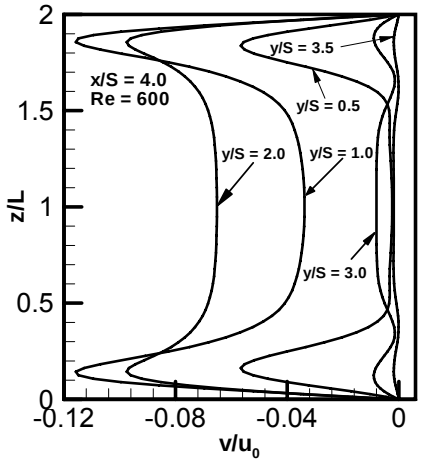

(c)

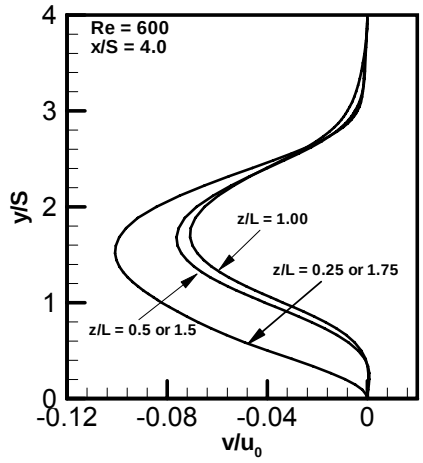

(d)

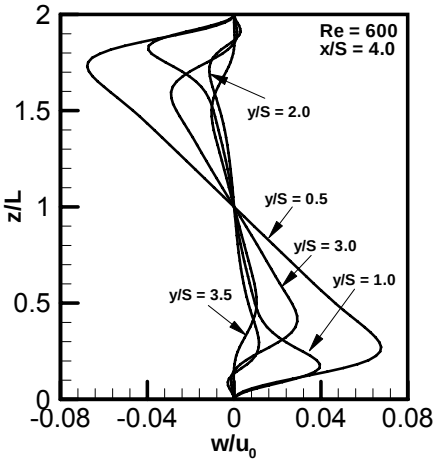

(e)

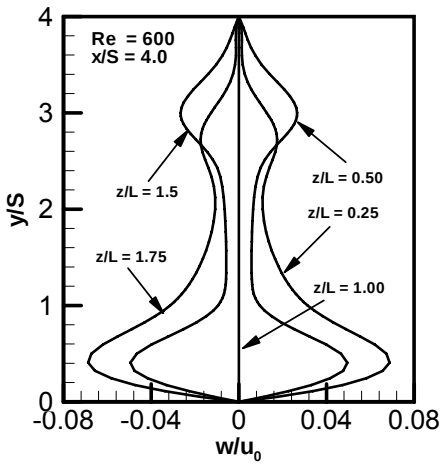

(f)

Along the spanwise direction Along the transverse direction

Fig. 2 Velocity distributions for *Re* = 600

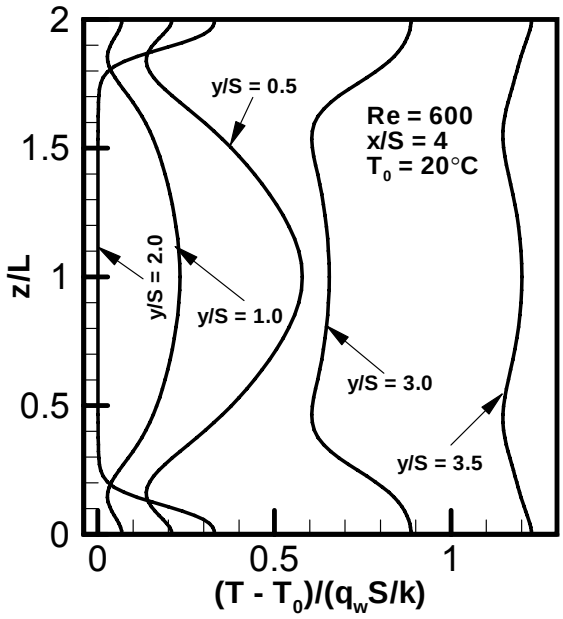

(*a*)

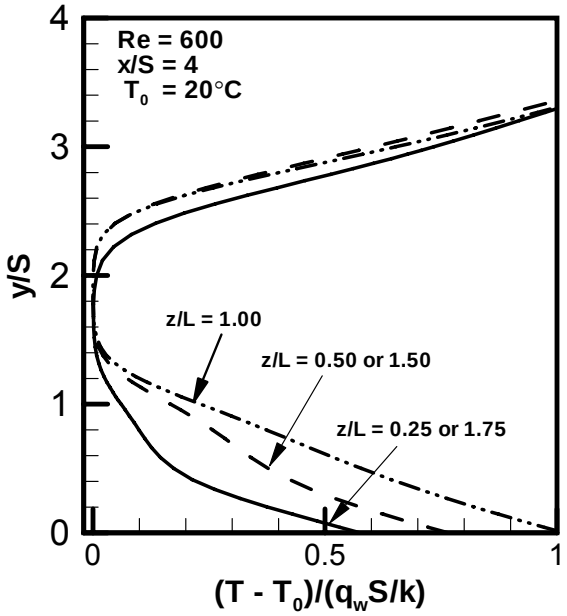

(*b*)

Fig. 3 Temperature distributions for *Re* = 600

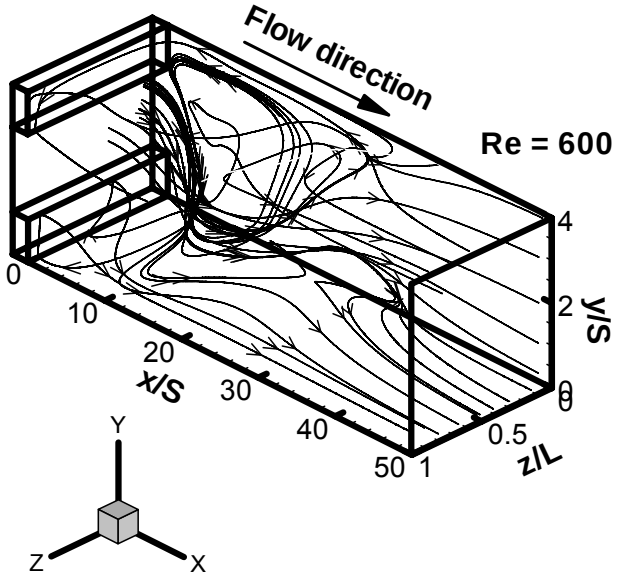

(a)

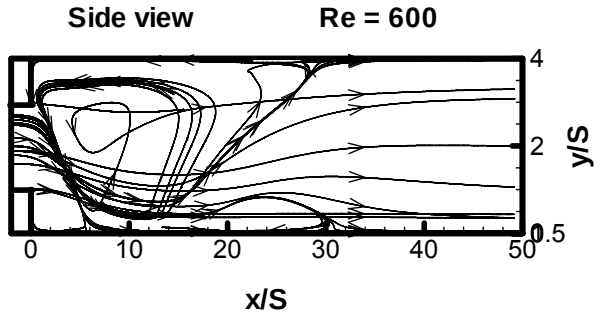

(b)

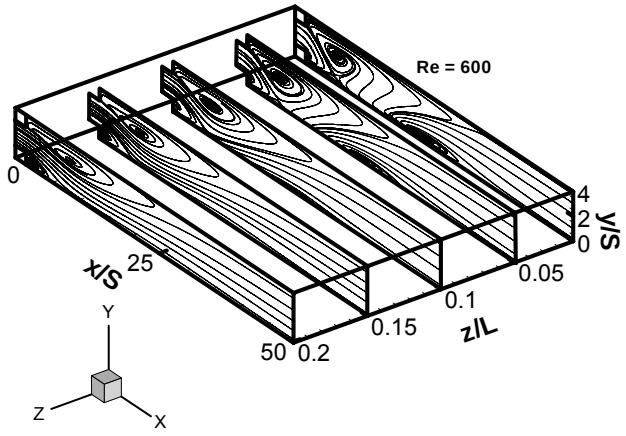

(*c*)

Fig. 4 Streamlines demonstrating general flow features

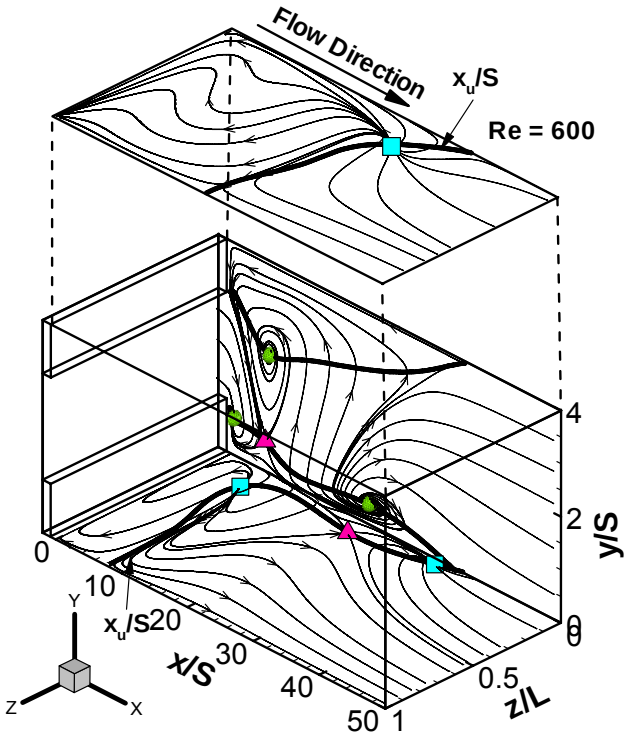

Fig. 5 Limiting streamlines adjacent to the bounding walls
(▲Saddle point; □ "jet-impingement"; and ● Focal Point locations)

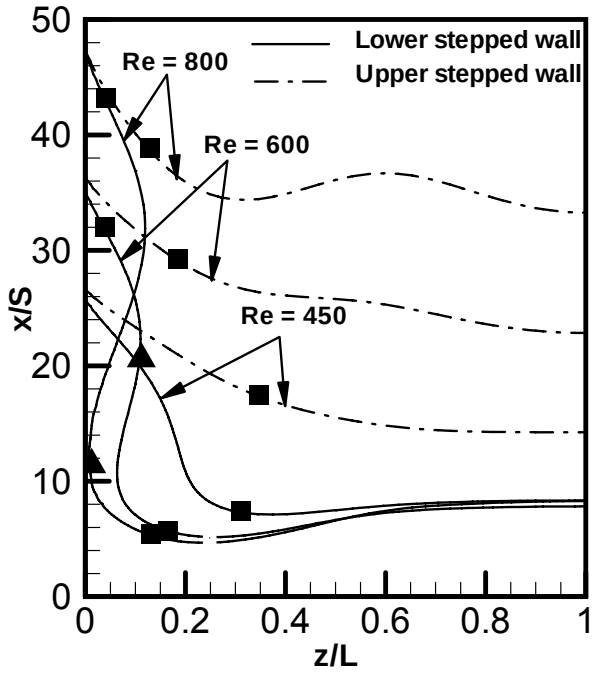

Fig. 6 Distributions of x_u-lines adjacent to the two stepped walls (y/S = 0.01 and 3.99)
(▲ Saddle point; ■ "jet-impingement" locations

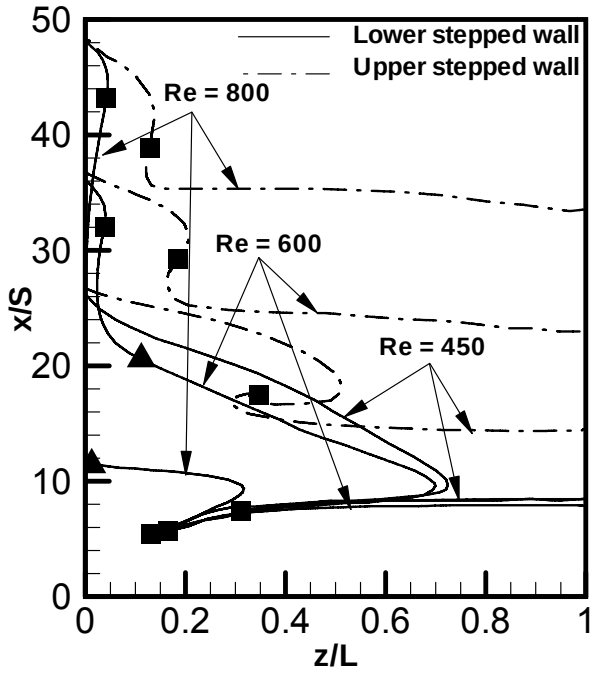

Fig. 7 Distributions of x_b-lines adjacent to the two stepped walls (y/S = 0.01 and 3.99)
(▲ Saddle point; ■ "jet-impingement" locations)

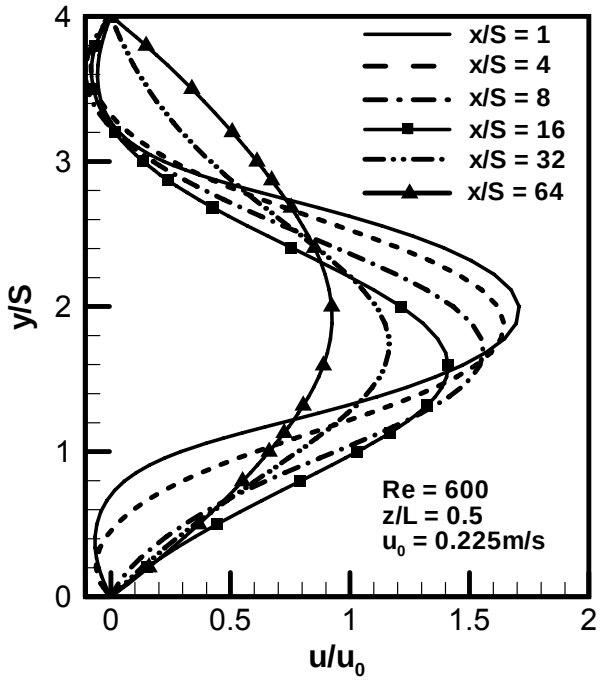

(*a*) Streamwise velocity component

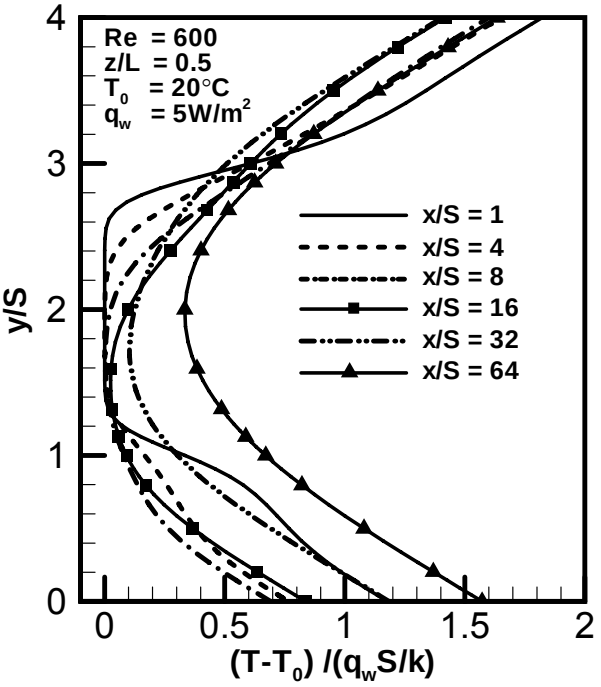

(*b*) Temperature distributions

Fig. 8 Transverse distributions of the temperature and streamwise velocity component at different streamwise locations

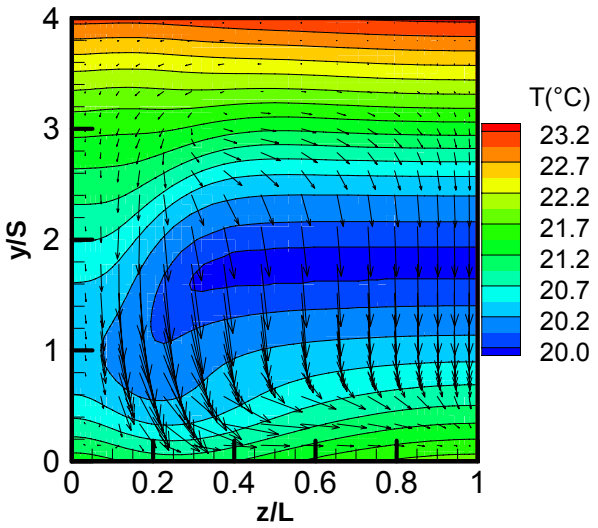

(*a*) At $x/S = 5.684$

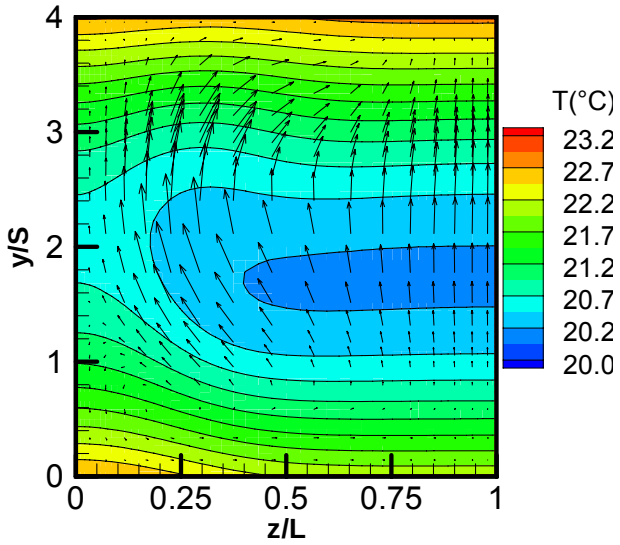

(*b*) At $x/S = 29.24$

Fig. 9 Velocity and temperature fields for $Re = 600$

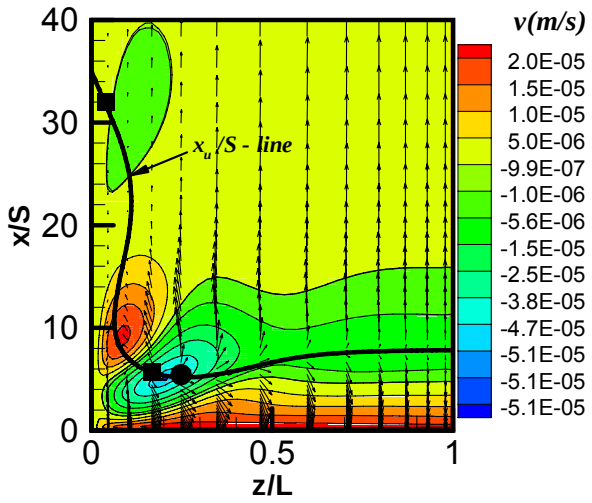

Fig. 10 Velocity field on a *y*-plane adjacent to the lower stepped wall (y/S = 0.01), Re = 600 (● Maximum Nusselt number; ■ "jet-impingements" locations)

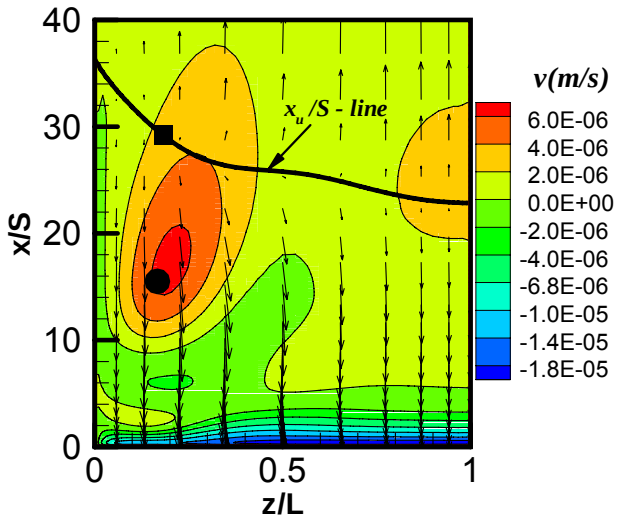

Fig. 11 Velocity field on a *y*-plane adjacent to the upper stepped wall (*y*/*S* = 3.99), *Re* = 600 (● Maximum Nusselt number; ■ "jet-impingement" locations)

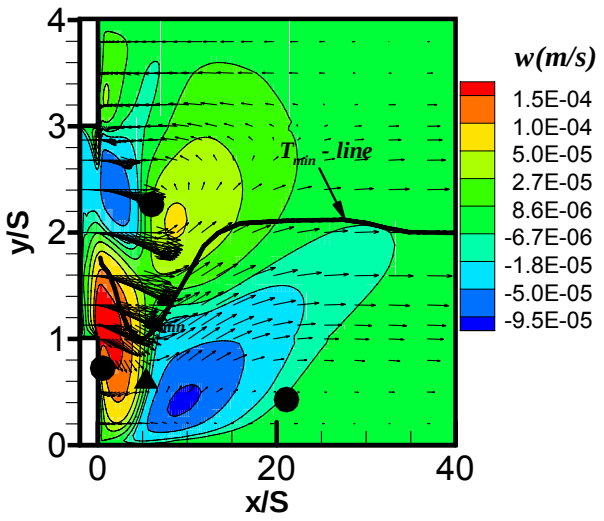

Fig. 12 Velocity field on a *z*-plane adjacent to the side wall ($z/L = 0.01$), $Re = 600$ (▲ Saddle point; ● Focal point locations)

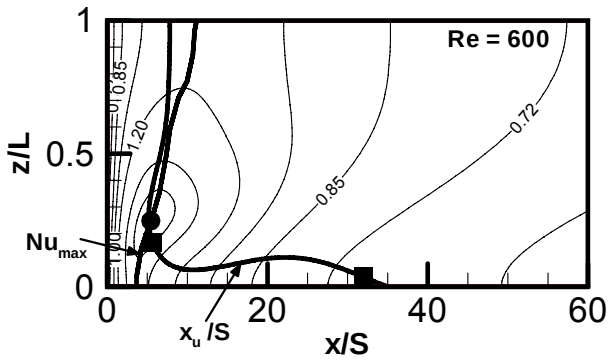

(*a*)

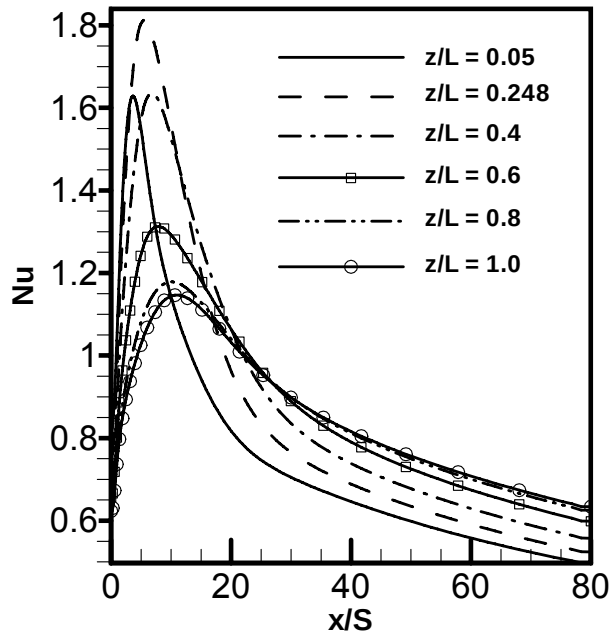

(*b*)

Fig. 13 Nusselt number distribution on the lower stepped wall ($y/S = 0$)
(● Maximum Nusselt number; ■ "jet-impingement" locations)

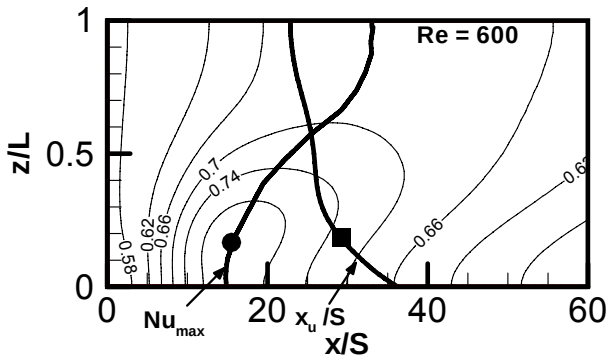

(*a*)

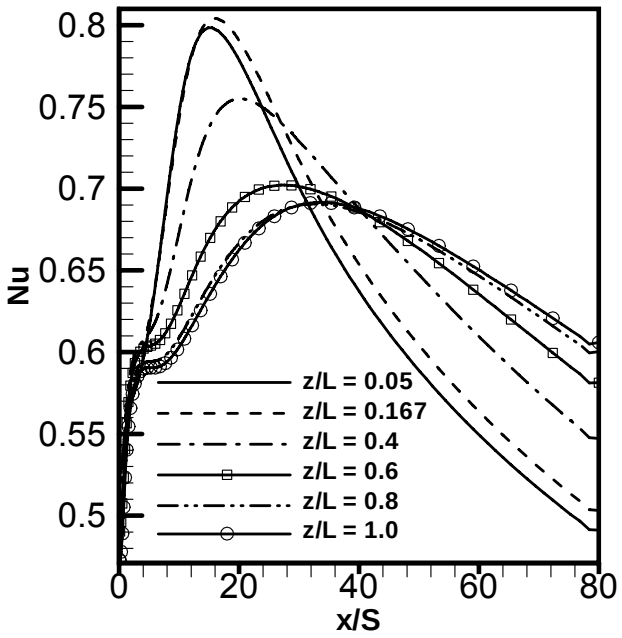

(*b*)

Fig. 14 Nusselt number distribution on the upper stepped wall ($y/S = 4$)
(● Maximum Nusselt number; ■ "jet-impingement" locations)

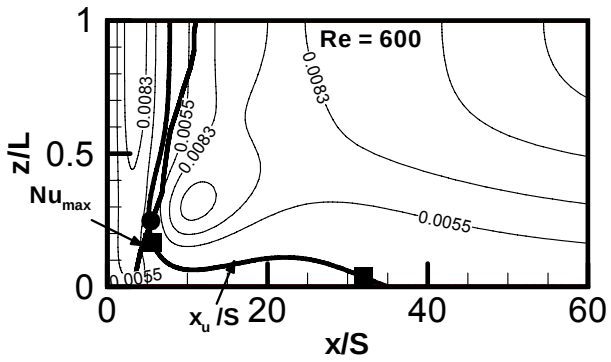

(*a*)

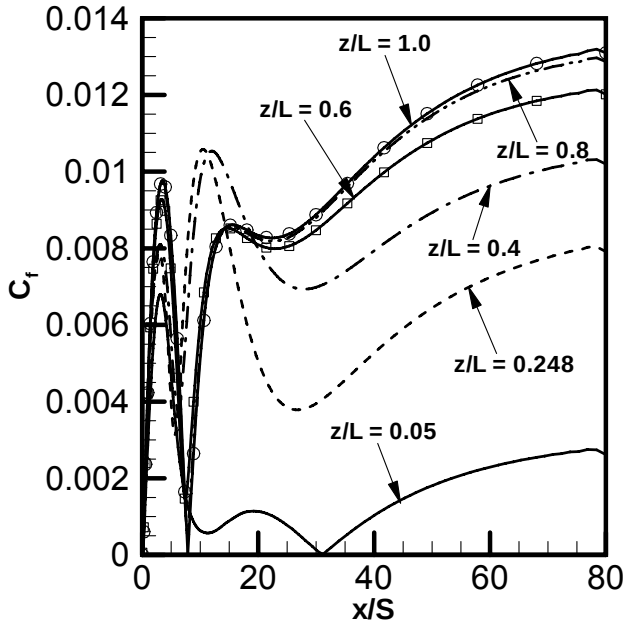

(*b*)

Fig. 15 Friction coefficient distribution on the lower stepped wall ($y/S = 0$) for $Re = 600$
(● Maximum Nusselt number; ■ "jet-impingement" locations)

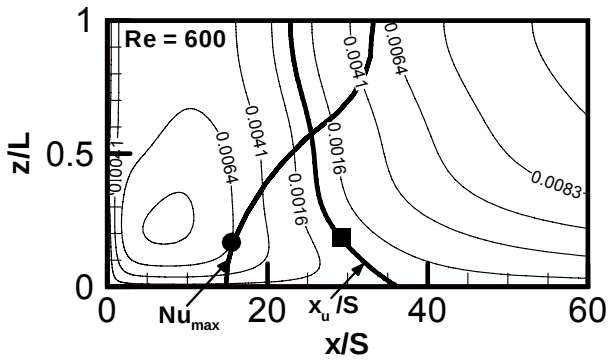

(*a*)

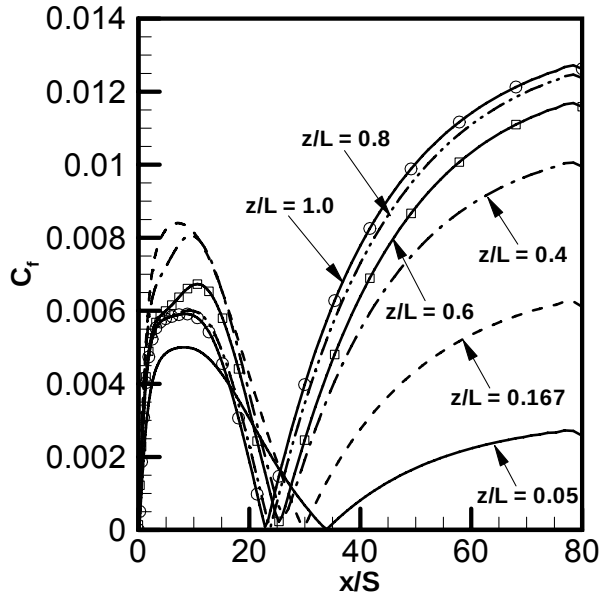

(*b*)

Fig. 16 Friction coefficient distribution on the upper stepped wall ($y/S = 4$) for $Re = 600$ (● Maximum Nusselt number; ■ "jet-impingement" locations)

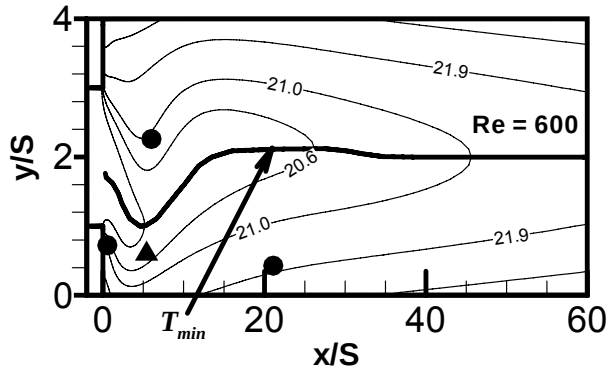

(*a*)

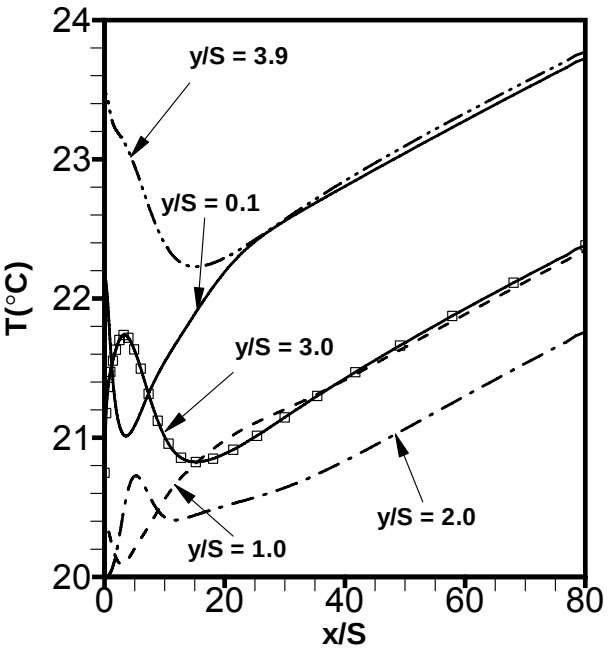

(b)

Fig. 17 Sidewall temperature distribution ($z/L = 0$) for $Re = 600$
(▲ Saddle point; ● "Focal point" locations)

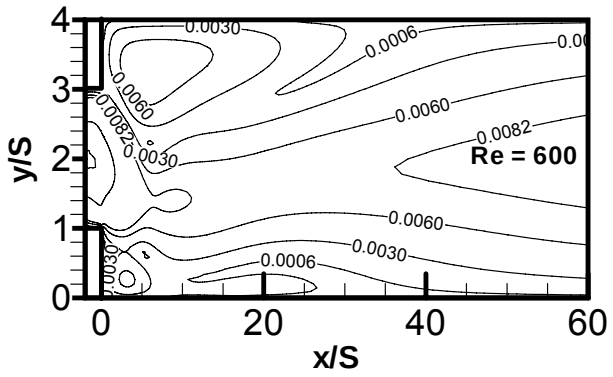

(*a*)

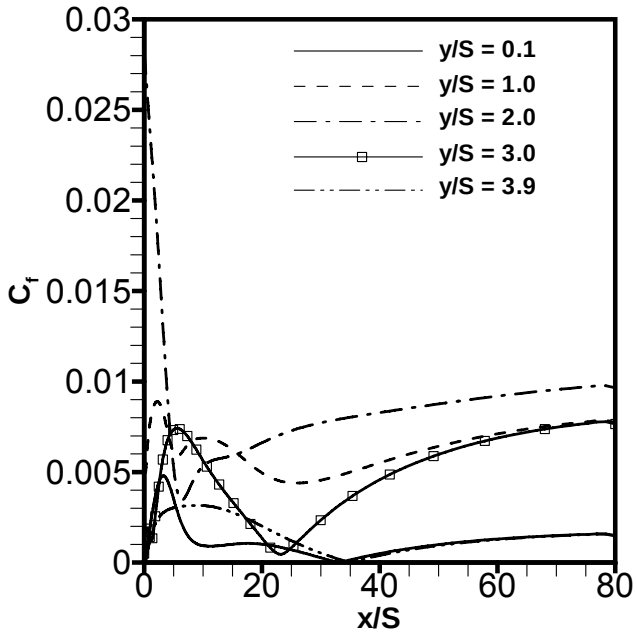

(*b*)

Fig. 18 Friction coefficient distribution on the side wall ($z/L = 0$) for $Re = 600$

II. Three-Dimensional Mixed Convection in Plane Symmetric-Sudden Expansion: Bifurcated Flow Regime

M. Thiruvengadam, B. F. Armaly and J. A. Drallmeier
Department of Mechanical and Aerospace Engineering
Missouri University of Science and Technology, Rolla, MO 65401, United States
Email: mtwv8@mst.edu, armaly@mst.edu and drallmei@mst.edu

Abstract

Simulations of three-dimensional laminar mixed convection in a vertical duct with plane symmetric sudden expansion are presented to illustrate the effects of the buoyancy assisting force and the duct's aspect ratio on flow bifurcation and heat transfer. The stable laminar bifurcated flow regime that develops in this geometry at low buoyancy levels leads to non-symmetric temperature and heat transfer distributions in the transverse direction, but symmetric distribution with respect to the center width of the duct in the spanwise direction. As the buoyancy force increases, due to increases in wall heat flux, flow bifurcation diminishes and both the flow and the thermal fields become symmetric at a critical wall heat flux. The size of the primary recirculation flow region adjacent to the sudden expansion increases on one of the stepped walls and decreases on the other stepped wall as the wall heat flux increases. The maximum Nusselt number that develops on one of the stepped walls in the bifurcated flow regime is significantly larger than the one that develops on the other stepped wall. The critical wall heat flux increases as the duct's aspect ratio increases for fixed Reynolds number. The maximum Nusselt number that develops in the bifurcated flow regime increases as the duct's aspect ratio increases for fixed wall heat flux and Reynolds number.

Introduction

Flow separation and reattachment due to sudden changes in geometry occur in many engineering applications where heating or cooling is required. These applications appear in electronic cooling equipment, cooling of turbine blades, combustion chambers, and many other heat exchanging devices. The flow and the heat transfer in most of these applications exhibit three-dimensional (3-D) flow behavior, but most of the published heat transfer results deal only with the two-dimensional (2-D) flow. Experimental (Durst et al. [1], Cherdron et al. [2], Durst et al. [3], and Fearn et al. [4]) and numerical (Durst et al. [3], Fearn et al. [4], Drikakis [5], and Hawa and Rusak [6]) studies have shown that laminar isothermal flow in plane symmetric sudden expansion exhibits symmetric steady laminar flow behavior for Reynolds number lower than the critical value, and asymmetric steady laminar bifurcated flow behavior for Reynolds number higher than the critical value. As the Reynolds number continues to increase the stable laminar bifurcated flow regime transforms into unsteady bifurcated flow regime and moves toward turbulent transition at higher Reynolds number. Tsui and Shu [7] and Alimi et al. [8] reported results from simulating laminar mixed convection in a 2-D plane symmetric sudden expansion. Three dimensional simulations of laminar mixed convection adjacent to backward-facing step are presented by Li and Armaly [9] and the governing equations are cited in that reference. Nie and Armaly [10] simulated three-dimensional forced convection in plane symmetric sudden expansion in symmetric flow regime. They reported the presence of swirling jet-like flow near the side wall in the separating shear layer and its influence on the Nusselt number distribution and friction coefficient on the stepped walls. Bifurcated forced convection results in 3-D plane symmetric sudden

expansion were published by Thiruvengadam et al. [11], and to the authors' knowledge none has been published on the effects of buoyancy force on the bifurcated 3-D flow and the heat transfer in this geometry. This fact, along with the realization that such geometry appears regularly in many industrial heat transfer devices, motivated the present study.

Problem Statement and Solution Procedure

The problem that is treated in this study is an extension to the one reported by Thiruvengadam et al. [11] on bifurcated forced convection in similar geometry. Their study illustrated the development of several jet-like flows that develop at the corners of the sudden expansion near the side walls which impinges on the stepped wall to form several recirculation flow regions. The jet-like flow impingement location is a critical point on the stepped walls from which streamlines originate and where the streamwise and the spanwise components of the wall shear stress (i.e. $\mu \partial u / \partial y$ and $\mu \partial w / \partial y$) are zero. The jet-like flow impingement on the stepped walls is responsible for the peak that develops in the Nusselt number distribution in that area near the side wall. They illustrated the development of several focal and saddle points in the flow region downstream from the sudden expansion. They presented the effects of the Reynolds number on the x_u-lines (where $\partial u/\partial y_{\ at\ wall} = 0$) distributions and pointed out that the region that is bounded by the x_u-line represents approximately the size of the primary recirculation flow region that develops adjacent to the two stepped walls downstream from the sudden expansion. In the present study the effects of buoyancy assisting force and the duct's aspect ratio on the flow and heat transfer are examined, and a schematic of the computational domain is presented in Fig. 1. The duct's heights (H) and (h)

downstream and upstream of the sudden expansion respectively are fixed at 0.04m and 0.02m resulting in an expansion ratio ($ER = H/h$) of 2. The step height (S) is fixed at 0.01m and different duct's width (W) are considered to examine the effects of duct's aspect ratio (upstream aspect ratio ($AR = W/h$)) on the results. The origin of the coordinate system is located at the bottom corner of the sudden expansion as shown in Fig. 1. The directions of the streamwise (x), transverse (y), and spanwise (z) coordinates are shown in that figure. The length of the computational domain is 1m downstream and 0.02m upstream of the sudden expansion, respectively, i.e. $-2 \le x/S \le 100$. This choice is made to insure that the flow at the inlet section of the duct (x/S = -2) is not affected by the sudden expansion in geometry, and the flow at the exit section of the duct (x/S = 100) can be treated as fully developed. The use of a longer computational domain did not change the flow or the thermal behavior in the important region downstream from the sudden expansion (x/S < 50). The governing equations for laminar, incompressible, three-dimensional, buoyancy assisting mixed convection (with gravity, g, in the streamwise direction) with constant properties under both steady and unsteady conditions are formulated for continuity, momentum and energy conservation. Thermal buoyancy effects are modeled using the Boussinesq approximation. The full elliptic 3-D coupled governing equations are solved numerically using a finite volume method to simulate the flow and the temperature fields in this computation domain. The results from the solution of the steady form of the governing equations compared very well with the results from the solution of the unsteady form of the governing equations. Details of the formulation and the solution can be found in Li and Armaly [9] as applied to the backward facing step geometry and will not be restated here due to space limitations.

The physical properties are treated as constants and evaluated for air at the inlet temperature of $T_0 = 20^{\circ}C$ (i.e., density (ρ) is 1.205 kg/m^3, specific heat (C_p) is 1005 J/Kg.^{o}C, dynamic viscosity (μ) is 1.81x10^{-5} kg/m.s, thermal conductivity (k) is 0.0259 W/m.^{o}C, and volumetric coefficient of thermal expansion (β) is 0.00341 1/K). Inlet flow (at x/S = -2, $1 \leq y/S \leq 3$, for all z) is considered to be isothermal ($T_0 = 20^{\circ}C$), hydrodynamically steady and fully developed with a distribution for the streamwise velocity component (u) equal to the one described by Shah and London [12]. The other velocity components (transverse (v) and spanwise (w)) are set to be equal to zero at that inlet section. The no-slip boundary condition (zero velocities) is applied to all of the wall surfaces. Uniform wall heat flux ($q_w = -k\,\partial T / \partial y\big|_{y=0\,and\,y=0.04}$) is specified, and it is the same for the two stepped walls (at y/S = 0 and 4, $0 \leq x/S \leq 100$, for all z), while the other walls are treated as adiabatic surfaces. The magnitude of the uniform wall heat flux is varied while keeping the Reynolds number ($Re = 2\rho u_0 h/\mu$, where u_0 is the average inlet velocity) fixed at 800 to investigate the effects of the buoyancy assisting force on the flow and heat transfer. Similarly, the magnitudes of the wall heat flux is fixed at 3 W/m^2, and the Reynolds number is fixed at 800 while the aspect ratio is varied to investigate its effect on the flow and heat transfer. Due to the symmetry in the spanwise direction in this geometry, the width of the computation domain is chosen as half of the actual width of the duct, $L = W/2$, and symmetry boundary conditions are applied at the center plane of the duct, i.e. at $z = L$, w = 0, and the gradient of all the other quantities with respect to z are set equal to zero. Fully developed flow and thermal conditions are imposed at the exit section (at x/S = 100, for all y and z) of the calculation domain.

Numerical solution of the governing equations and boundary conditions are performed by utilizing the commercial computational fluid dynamics (CFD) code FLUENT 6.2. The mesh is generated using FLUENT's preprocessor GAMBIT. Hexahedron volume elements are used in the simulation. At the end of each iteration, the residuals for each of the conserved variables is computed and stored, thus recording the convergence history. The convergence criterion required that the scaled residuals be smaller than 10^{-10} for the mass and the momentum equations and smaller than 10^{-11} for the energy equation. Calculations are performed on DELL workstation, and the CPU time for converged solution for Re = 800 is approximately 24 hours. Significantly longer time is needed for cases where the wall heat flux is very close to the critical value and where the stable bifurcated flow regime changes to a stable symmetric flow regime. The SIMPLEC algorithm is used for the pressure velocity coupling, and the momentum and energy equations are discretized with the Second Order Upwind scheme in order to improve the accuracy of the simulations. Detailed descriptions of the CFD code and the solution procedures may be found in the FLUENT manual.

The computational grid distribution is selected to ensure high density near the bounding walls and in the regions of the sudden expansion where high gradients exist, in order to ensure the accuracy of the simulation. Grid independence tests were performed using different grid densities for Re = 800 for all aspect ratios. The velocities in x, y and z directions, temperatures at the location x/S = 5, y/S = 0.5, and z/L = 0.25 and the reattachment length at z/L = 1 and y/S = 0.01 in the computational domain are presented in Table 1 for different grid densities for the aspect ratio AR = 8. Comparisons of these results from grid 4 and grid 5 show a difference of less than 1%. For that reason grid 4

(220 x 64 x 50) is used downstream of the sudden expansion ($0 \le x/S \le 100$) and a grid of (20 x 32 x 50) is used upstream of the sudden expansion ($-2 \le x/S \le 0$) for half of the duct's width ($0 \le z/L \le 1$). This grid size is used for aspect ratios smaller or equal to 8 ($AR \le 8$). Similarly grid independent studies for AR = 16 show that a grid of (220 x 64 x 60) provides grid independent results for that aspect ratio and this grid size is used downstream of sudden expansion for $8 < AR \le 16$. The very favorable comparison that is shown in Fig. 2 between measured results by Fearn et al. [4] and the simulated results validate the simulation code. Additional results on code validation could be found in Thiruvengadam et al. [11].

Table 1 Velocities and temperatures at x/S = 5, y/S = 0.5, and z/L = 0.25 for different computational grids (Re = 800 and AR = 8 for q_w = 3 W/m^2)

Grid	x x y x z Grid size (downstream)	u (m/s)	v (m/s)	w (m/s)	T (K)	x_u/S at z/L = 1 and y/S = 0.01
1	100 x 32 x 20	0.0376303	-0.0024823	0.0226579	293.226	9.62730
2	150 x 40 x 30	0.0328437	-0.0019410	0.0232115	293.219	9.50386
3	180 x 52 x 40	0.0334497	-0.0020106	0.0236612	293.219	9.50456
4	220 x 64 x 50	0.0319877	-0.0017685	0.0239029	293.219	9.51968
5	240 x 72 x 60	0.0320299	-0.0018307	0.0241013	293.218	9.51878

Results and Discussion

Effects of Buoyancy. The results presented in this study focus on the laminar steady bifurcated flow regime that develops in this geometry. Due to space limitations and the fact that the results exhibit similar behavior for different Reynolds numbers, all of the presented results are for Re = 800. The uniform wall heat flux on the two stepped walls is varied to examine the influence of the buoyancy assisting force, and the duct's

aspect ratio is varied to examine its effect on the results. The effects of the buoyancy assisting force is examined by fixing the Reynolds number at 800 and the duct's aspect ratio at 4 (AR = 4) while varying the wall heat flux (q_w) from 0 – 5 W/m^2, thus covering the bifurcated and the non-bifurcated flow regimes for this aspect ratio and Reynolds number. The general flow features in the bifurcated mixed convection flow regime are similar to the ones presented by Thiruvengadam et al. [11] for bifurcated forced convection flow regime. The general flow features are presented in Fig. 3a for q_w = 1 W/m^2 and in Fig. 3b for q_w = 5 W/m^2. For this aspect ratio and Reynolds number, the bifurcated flow regime exists only for q_w < 3.52 W/m^2. When the wall heat flux exceeds that critical value, the flow bifurcation disappears and a symmetric non-bifurcated flow develops as illustrated in Fig. 3b. Increasing the buoyancy force by increasing the wall heat flux increases the streamwise velocity component adjacent to the two stepped walls and that reduces the length of the primary recirculation flow region. Changes in the length of the recirculation flow region influence the pressure distribution in that streamwise location. The resulting change in the pressure distribution causes the length of the recirculation region to decrease on one stepped wall and increase on the other stepped wall with increasing buoyancy force until symmetric flow is reached. The buoyancy assisting force in the neighborhood of the bifurcation flow region (at x/S = 6) at the critical wall heat flux as defined by Gr_x/Re^2 (where Gr_x is the local Grashof Number = $\rho^2 g\beta q_w x^4/\mu^2 k$) is equal to 0.41.

The effects of the wall heat flux on the distributions of the x_u-lines (where $\partial u/\partial y_{\,at\ wall}$ = 0) are presented in Fig. 4. The region that is bounded by this line represents approximately the size of the primary recirculation flow region that develops adjacent to

the two stepped walls downstream from the sudden expansion. The size of that region at the duct's center decreases on one of the stepped walls and increases on the other stepped wall as the wall heat flux increases until the bifurcated flow regime is transformed into a symmetric flow regime when $q_w \geq 3.52$ W/m^2. Near the side wall, however, the size of that region decreases on both of the stepped walls as the wall heat flux increases. The jet-like flow that develops near the side wall impinges on the stepped walls and its impingement locations are identified in that figure. The jet-like flow impingement location is a critical point on the stepped walls from which streamlines originate and where the streamwise and the spanwise components of the wall shear stress (i.e. $\mu \partial u / \partial y$ and $\mu \partial w / \partial y$) are zero. The jet-like flow impingement on the stepped walls is responsible for the peak that develops in the Nusselt number distribution in that area near the side wall. Two jet-like flow impingement locations develop on one of the stepped walls (at $y/S = 0$) when $q_w \leq 2$ W/m^2, but only one impingement location develops when $q_w > 2$ W/m^2 as shown in Fig. 4. The first jet-like flow impingement location is close to the sudden expansion and the second location develops farther downstream. The first jet-like flow impingement location on the two stepped walls moves away from the side wall, while the second impingement location that develops on one of the stepped walls at $y/S = 0$ moves toward the side wall when the wall heat flux increases.

The effects of the wall heat flux on the streamwise distributions of the Nusselt number ($Nu = q_w S/k(T_w - T_0)$, where T_w is the local wall temperature) on the two stepped walls are presented at the center of the duct (at $z/L = 1$) and near the side wall (at $z/L = 0.1$) in Fig. 5. The Nusselt number increases rapidly after the sudden expansion, reaches a peak value and then decreases asymptotically to its fully developed value as x/S

continues to increase. The peak in that distribution is higher near the side wall and on the stepped wall with the smaller primary recirculation flow region (i.e. at $y/S = 0$). On this stepped wall, the peak in the Nusselt number distribution increases as the wall heat flux decreases in the bifurcated flow regime, and it is higher than the one that develops in the symmetric non-bifurcated flow regime (i.e. at $q_w = 4$ W/m^2). The peak in the Nusselt number is due to the jet-like flow impingement in that region (higher transverse velocity impinges on the stepped wall in that region) causing the wall temperature to decrease. This decrease in wall temperature causes the Nusselt number to increase locally in that region (the Nusselt number is inversely proportional to the wall temperature). The transverse velocity component that impinges on the stepped wall with smaller recirculation flow region ($y/S = 0$) is one magnitude higher than the one that impinges on the other stepped wall ($y/S = 4$) with the larger recirculation flow region and that is why a lower Nusselt number develops on that stepped wall in the bifurcated flow regime. Smaller recirculation flow region produces higher jet impingement velocity and that results in a higher Nusselt number. The Nusselt number that develops on that wall in the bifurcated flow regime is lower than the one that develops in the symmetric non-bifurcated flow regime. The differences in the Nusselt number for the two stepped walls disappear when bifurcation ceases to exist and symmetric flow develops for higher wall heat flux. In the symmetric non-bifurcated mixed convection flow regime the maximum Nusselt number increases as the wall heat flux increases.

The effects of the wall heat flux on the spanwise distributions of the local Nusselt number on the two stepped walls are presented at three streamwise locations of $x/S = 2$, 6 and 25 in Fig. 6. These streamwise locations are selected to represent one location inside

the primary recirculation flow region, a second location in the region of flow reattachment on one of the stepped walls ($y/S = 0$), and a third location in the region of flow reattachment on the other stepped wall (at $y/S = 4$). Inside the recirculation flow region and upstream of the jet-like flow impingement region, i.e. at $x/S = 2$, a maximum in the spanwise Nusselt number distribution develops near the side wall, and decreases gradually to its value at the center of the duct. On the other hand a peak in the spanwise Nusselt number distribution develops near the sidewall in the region of the jet-like flow impingement region, i.e. at $x/S = 6$ for $y/S = 0$ and $x/S = 25$ for $y/S = 4$, and that peak moves toward the center of the duct as the streamwise location increases beyond the jet-like flow impingement region, i.e. at $x/S = 25$ for $y/S = 0$. The influence of the buoyancy force, or wall heat flux, on the magnitude of the Nusselt number is the same as discussed previously for Fig. 5, which is decreasing as the wall heat flux increasing for the wall at $y/S = 0$ and the reverse is true for the wall at $y/S = 4$.

The effects of the wall heat flux on the streamwise distributions of the friction coefficient ($C_f = 2\tau_w / \rho u_0^2$, where τ_w is the local wall shear stress $= \mu\sqrt{(\partial u/\partial y)^2 + (\partial w/\partial y)^2}$) on the two stepped walls are presented at the center of the duct (at $z/L = 1$) and near the side wall (at $z/L = 0.1$) in Fig. 7. The friction coefficient increases rapidly after the sudden expansion and a local maximum develops inside the primary recirculation flow region. Its magnitude decreases rapidly after that peak as x/S continues to increase until it reaches its minimum value at the x_u-line (the approximate edge of the recirculation flow region). The gradient of the streamwise velocity component ($\partial u/\partial y\big|_{y=0 \text{ and } y=0.04} = 0$) is zero on this line causing the friction coefficient to reach its minimum value in that region. The distribution of the friction coefficient at a

given location is dependent on its closeness to the x_u-line. Its magnitude then increases rapidly as x/S continues to increase and develops a maximum at the center of the duct in the fully developed flow region. In that region (at large x/S), its magnitude increases as the wall heat flux increases, and the maximum that develops adjacent to the side wall is smaller than the maximum that develops at the center of the duct. The increase in friction coefficient in the fully developed region with increasing wall heat flux is due to the increased streamwise velocity and its gradient at higher buoyancy force. Inside the primary recirculation flow region at the center of the duct, the maximum friction coefficient decreases as the wall heat flux increases. This is expected because increased buoyancy force reduces the reversed streamwise velocity component in the recirculation region. The presence of the second recirculation flow region on the stepped wall (y/S = 0) near the sidewall for lower values of wall heat flux influences significantly the distribution of the friction coefficient as can be seen in the figure, but does not influence the Nusselt number distribution. Velocity and temperature distributions in the bifurcated flow regime are generally similar to the ones presented by Thiruvengadam et al. [11], and they illustrate the bifurcated nature on the velocity and thermal fields. They are not presented here due to space limitations.

Effects of Duct's Aspect Ratio. Flow bifurcation that develops for a given Reynolds number in this geometry ceases to exist when the wall heat flux exceeds a critical value. The critical wall heat flux for each aspect ratio is determined by using the bifurcation diagram that was described by Drikakis [5]. A sample of a bifurcation diagram is shown in Fig. 8 for the case of AR = 8. The difference in the reattachment length on the two stepped walls (Δx_u) is plotted against the wall heat flux. It can be seen

that the critical wall heat flux for this aspect ratio is 5.61 W/m^2. Similar diagrams can be plotted for other aspect ratios and the results show that this critical wall heat flux increases with increasing aspect ratio reaching its maximum when $AR = \infty$ (i.e. 2-D flow) as tabulated in Table 2 for this geometry at Reynolds number of 800.

Table 2 Critical wall heat flux (*Re* = 800)

Duct's aspect ratio	4	6	8	12	16	2-D
Critical wall heat flux (W/m^2)	3.52	4.83	5.61	6.14	6.18	6.21

The effects of the aspect ratio are examined by fixing the Reynolds number at 800 and the wall heat flux at 3 W/m^2 while varying only its magnitude between 4 and infinity. Its effects on the x_u-lines are presented in Fig. 9, and the jet-like flow impingement locations on the two stepped walls are identified on this figure. The level of bifurcation increases as the aspect ratio increases for a fixed wall heat flux. It should be noted that the level of bifurcation is relatively smaller for the case of $AR = 4$ at the selected wall heat flux of $q_w = 3$ W/m^2 because this heat flux is relatively close to the critical wall heat flux for this aspect ratio, which is 3.52 W/m^2. The primary jet-like flow impingement locations move toward the center of the duct as the aspect ratio decreases or with decreasing level of bifurcation. These jet-like flow impingements influence significantly the magnitude and the distributions of the Nusselt number. The secondary jet-like flow impingement locations that appear on one of the stepped walls (at $y/S = 0$) downstream from the primary ones (for some of the aspect ratios) are relatively weak and do not have significant influence on the Nusselt number. They appear to move closer to the side wall as the aspect ratio decreases and disappear as the bifurcation level decreases.

The effects of the aspect ratio on the streamwise distributions of the local Nusselt number on the two stepped walls are presented at the center of the duct (at $z/L = 1$) and near the side wall (at $z/L = 0.1$) in Fig. 10. The general streamwise behavior is similar to the one presented in Fig. 5. The peak value of the Nusselt number that develops near the side wall increases with increasing aspect ratio. This is due to the increased level of bifurcation for higher aspect ratios. Significant three-dimensional effects (influence of the side walls) continue to exist for the largest duct's aspect ratio of 16, as can be seen when comparing its results with those for the two-dimensional flow. The Nusselt number increases as the duct's aspect ratio decreases at the center of the duct (at $z/L = 1$), but a reverse trend develops in the region near the side wall (at $z/L = 0.1$) in the fully developed flow region. The magnitude of the Nusselt number on one of the stepped walls (at $y/S = 0$) is significantly greater than what develops on the other stepped wall (at $y/S = 4$) for all duct's aspect ratios due to the higher jet-like flow impingement velocity when the recirculation flow region is smaller (as discussed previously). The magnitudes of the maximum Nusselt number and the locations where it occurs are listed in Tables 3 and 4 for Reynolds number of 800 and wall heat flux of 3 W/m^2 for different duct's aspect ratios.

Table 3 Locations of Nu_{max} on $y/S = 0$ for $q_w = 3$ W/m^2

x/S	y/S	z/L	Nu_{max}	AR
6.17	0	0.205	1.4	4
6.38	0	0.185	2.16	6
5.77	0	0.149	2.47	8
6.03	0	0.117	2.76	12
6.47	0	0.092	2.82	16
10.42	0		1.54	2-D

Table 4 Locations of Nu_{max} on y/S = 4 for q_w = 3 W/m^2

x/S	*y/S*	*z/L*	Nu_{max}	*AR*
15.16	4	0.186	0.830	4
23.56	4	0.116	0.822	6
25.27	4	0.085	0.888	8
24.12	4	0.0613	0.938	12
24.69	4	0.0512	0.973	16
29.02	4		0.927	2-D

The effects of the duct's aspect ratio on the spanwise distributions of the local Nusselt number on the two stepped walls are presented at three streamwise locations of x/S = 2, 6 and 25 in Fig. 11. These streamwise locations are selected at the same locations as in Fig. 6. The spanwise distributions of Nusselt number develops a peak near the side wall in the jet-like flow impingement region, i.e. x/S = 6 for y/S = 0 and x/S = 25 for y/S = 4, but that peak decreases as the aspect ratio decreases due to decreasing level of the bifurcation. At the center of the duct in these regions the Nusselt number increases as the aspect ratio increases with noted exception for aspect ratios between 4 and 6 at y/S = 4 and x/S = 25. The level of bifurcations for this range of aspect ratios is low due to the proximity of the wall heat flux to the critical value, and that is the reason for such a deviation. Upstream of the jet-like flow impingement region (inside the primary recirculation flow region, i.e. x/S = 2 for y/S = 0 and x/S = 2 and 6 for y/S = 4) and at the center of the duct, the Nusselt number increases with aspect ratio on one of the stepped walls (y/S = 0) but the reverse trend develops on the other stepped wall (y/S = 4). The changing trends in the size of the recirculation flow regions with aspect ratio are responsible for that behavior. Downstream from the jet-like flow impingement region for

y/S = 0, i.e. x/S = 25 at the center of the duct, the Nusselt number decreases with increasing aspect ratio.

The effects of the duct's aspect ratio on the streamwise distributions of the friction coefficient on the two stepped walls are presented at the center of the duct (at z/L = 1) and near the side wall (at z/L = 0.1) in Fig. 12. The streamwise behavior is similar to the one presented in Fig. 7. In the fully developed flow region its magnitude increases as the aspect ratio increases near the side wall (at z/L = 0.1) but at the center of the duct (at z/L = 1) that trend is reversed. The level of bifurcation and the location where the jet-like flow impinges on the stepped walls influence significantly the magnitude and the distributions of the friction coefficient.

Conclusions

The effects of buoyancy assisting force and duct's aspect ratio on flow bifurcation and on heat transfer for three-dimensional laminar mixed convection in a vertical plane symmetric sudden expansion is simulated, and results are presented for a duct with expansion ratio of two at a Reynolds number of 800. Flow bifurcation that develops for a given Reynolds number in this geometry decreases as the wall heat flux (buoyancy force) increases, and bifurcation ceases to exist when the wall heat flux exceeds a critical value. This critical wall heat flux increases with increasing duct's aspect ratio, reaching its maximum value of 6.21 W/m^2 for the two-dimensional flow ($AR = \infty$) in the geometry that is considered in this study. In the bifurcated flow regime, the flow and the thermal fields are not symmetric in the transverse direction but are symmetric relative to the center of the duct in the spanwise direction. The maximum Nusselt number, that increases as the duct's aspect ratio increases, decreases as the wall heat flux increases.

For a given aspect ratio at the center of the duct, the Nusselt number increases on one of the stepped walls (the wall with larger primary recirculation flow region), and decreases on the other stepped wall as the wall heat flux increases. For a given wall heat flux at the center of the duct and inside the recirculation flow region, the Nusselt number decreases on one of the stepped walls (the wall with larger primary recirculation flow region), and increases on the other stepped wall as the aspect ratio increases. The presented results illustrate the effects of buoyancy assisting force and duct's aspect ratio on the distributions of the Nusselt number and the friction coefficient on the two stepped walls in the bifurcated flow regime.

Acknowledgement

This work was supported in part by a DOE-Basic Energy Sciences grant No. DE-FG02-03ER46067, and by an NSF grant No. CTS-0352135.

Nomenclature

AR = Upstream aspect ratio = W/h

C_f = Skin friction coefficient = $2\tau_w / \rho u_0^2$

C_p = Specific heat

ER = Expansion ratio = H/h

H = Duct height downstream from the step

h = Duct height upstream from the step

k = Thermal conductivity

L = Half width of the duct

Nu = Nusselt number = $q_w S/k(T_w - T_0)$

q_w = Wall heat flux = $q_w = -k\,\partial T / \partial y\big|_{y=0 \text{ and } y=0.04}$

Gr_x = Local Grashof Number = $\rho^2 g\beta q_w x^4/\mu^2 k$

Re = Reynolds number = $2\rho u_0 h/\mu$

S = Step height

T_w = Local wall Temperature

T_0 = Inlet fluid temperature

u = Velocity component in the x- coordinate direction

u_0 = Average inlet velocity

v = Velocity component in the y- coordinate direction

W = Width of the duct

w = Velocity component in the z- coordinate direction

x = Streamwise coordinate

y = Transverse coordinate

z = Spanwise coordinate

x_u = Locations where the streamwise velocity gradient is zero ($\partial u / \partial y_{\text{ at wall}} = 0$)

Δx_u = Difference in the reattachment length for the two stepped walls

Greek letters

β = Volumetric coefficient of thermal expansion

μ = Dynamic viscosity

ρ = Density

τ_w = Wall shear stress $= \mu\sqrt{(\partial u/\partial y)^2 + (\partial w/\partial y)^2}$ on the stepped walls

References

[1] Durst, F., Melling, A., and Whitelaw, J.H., 1974, "Low Reynolds Number Flow over a Plane Symmetric Sudden Expansion," J. Fluid Mech., 64, pp. 111-128.

[2] Cherdron, W., Durst, F., and Whitelaw, J.H., 1978, "Asymmetric Flows and Instabilities in Symmetric Ducts with Sudden Expansions," J. Fluid Mech., 84, pp. 13-31.

[3] Durst, F., Pereira, J.C.F., and Tropea, C., 1993, "The Plane Symmetric Sudden-Expansion Flow at Low Reynolds Numbers," J. Fluid Mech., 248, pp. 567-581.

[4] Fearn, R.M., Mullin, T., and Cliffe, K.A., 1990, "Nonlinear Flow Phenomena in a Symmetric Sudden Expansion," J. Fluid Mech., 211, pp. 595-608.

[5] Drikakis, D., 1997, "Bifurcation Phenomena in Incompressible Sudden Expansion Flows," Phys. Fluids, 9(1), pp. 76-87.

[6] Hawa, T., and Rusak, Z., 2001, "The Dynamics of a Laminar Flow in a Symmetric Channel with a Sudden Expansion," J. Fluid Mech., 436, pp. 283-320.

[7] Tsui, Y.Y., and Shu, S.J., 1998, "Effects of Buoyancy and Orientation on the Flow in a Duct Preceded with a Double-Step Expansion," Int. J. Heat Mass Transfer, 41, pp. 2687-2695.

[8] Alimi, S.E., Orfi, J., and Nasrallah, S.B., 2005, "Buoyancy Effects on Mixed Convection Heat and Mass Transfer in a Duct with Sudden Expansions," Heat Mass Transfer, 41, pp. 559-567.

[9] Li, A., and Armaly, B. F., 2000, "Mixed Convection Adjacent to 3-D Backward-Facing Step," *Proceedings of the ASME-IMECE Conference*, ASME HTD, 366-2, pp. 51-58.

[10] Nie, J.H., and Armaly, B.F., 2004, "Three-Dimensional Forced Convection in Plane Symmetric Sudden Expansion," ASME J. Heat Transfer, 126, pp. 836-839.

[11] Thiruvengadam, M., Nie, J.H., and Armaly, B.F., 2005, "Bifurcated Three-Dimensional Forced Convection in Plane Symmetric Sudden Expansion," Int. J. Heat Mass Transfer, 48, pp. 3128-3139.

[12] Shah, R.K., and London, A.L., 1978, *Laminar Forced Convection in Ducts*, Academic Press, New York, pp. 196-198.

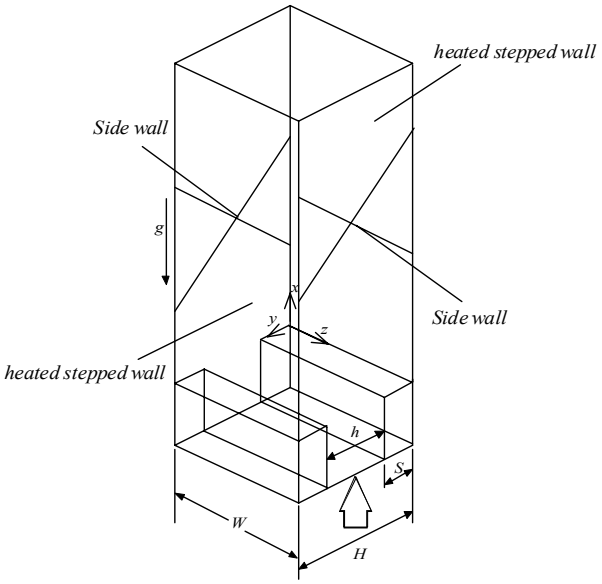

Fig. 1 Schematic of the computational domain

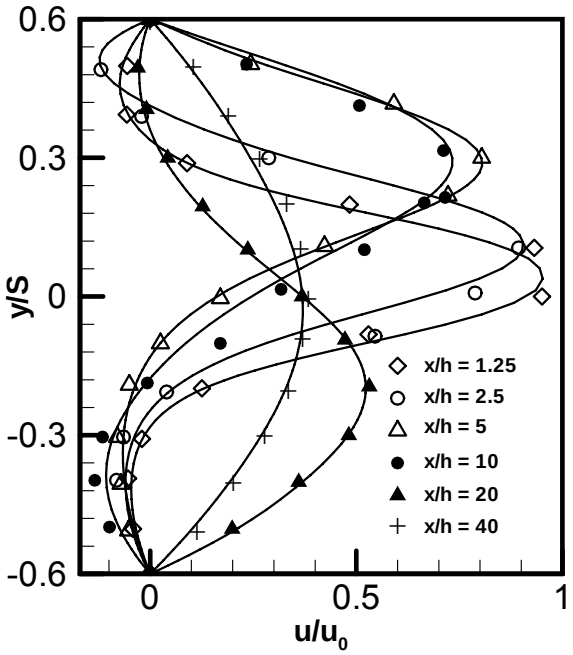

Fig. 2 Comparison with measured results of Fearn et al. [4]
(solid lines represent simulated values)

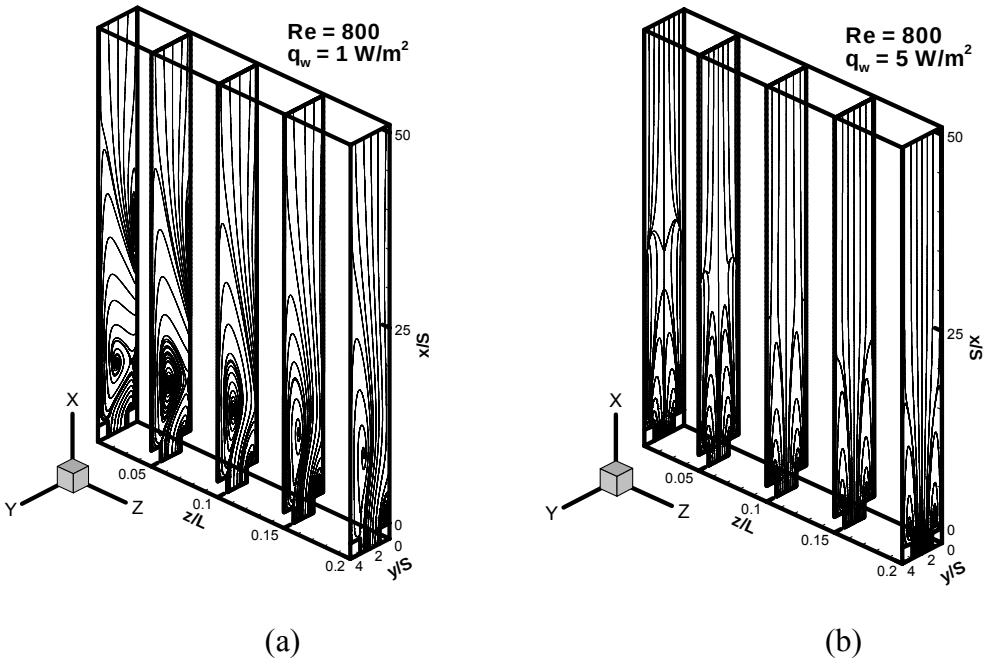

(a) (b)

Fig. 3 Streamlines in the bifurcated and non-bifurcated flow regimes (AR = 4)

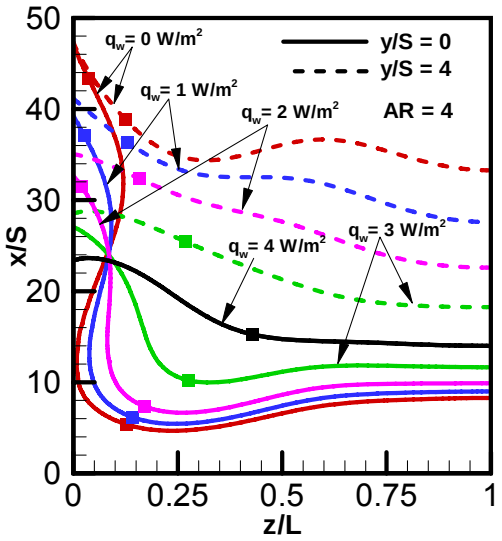

Fig. 4 Effects of wall heat flux on the x_u-lines (■ Locations of the jet-like flow impingement)

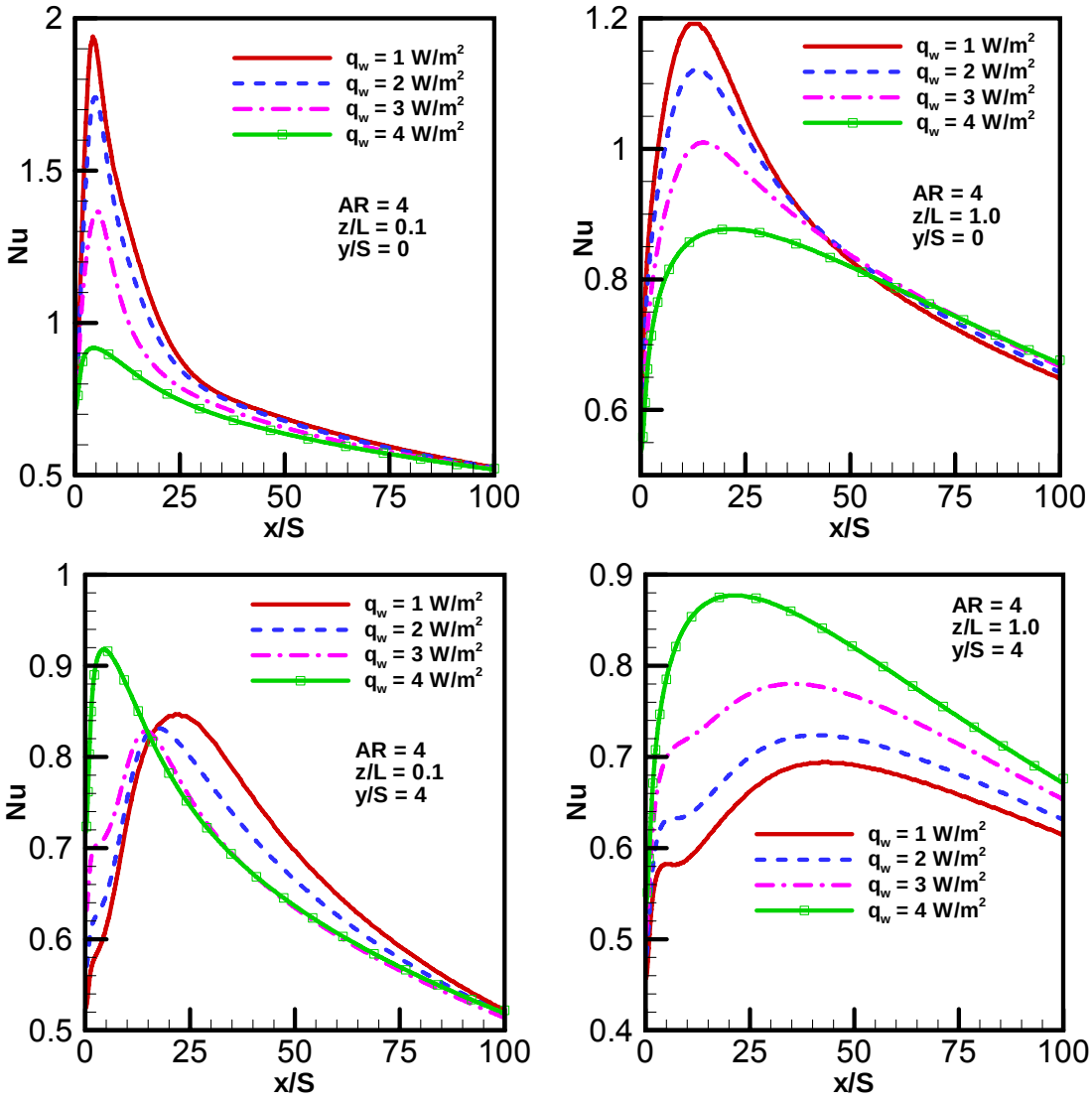

Fig. 5 Effects of wall heat flux on the streamwise distributions of the Nusselt number

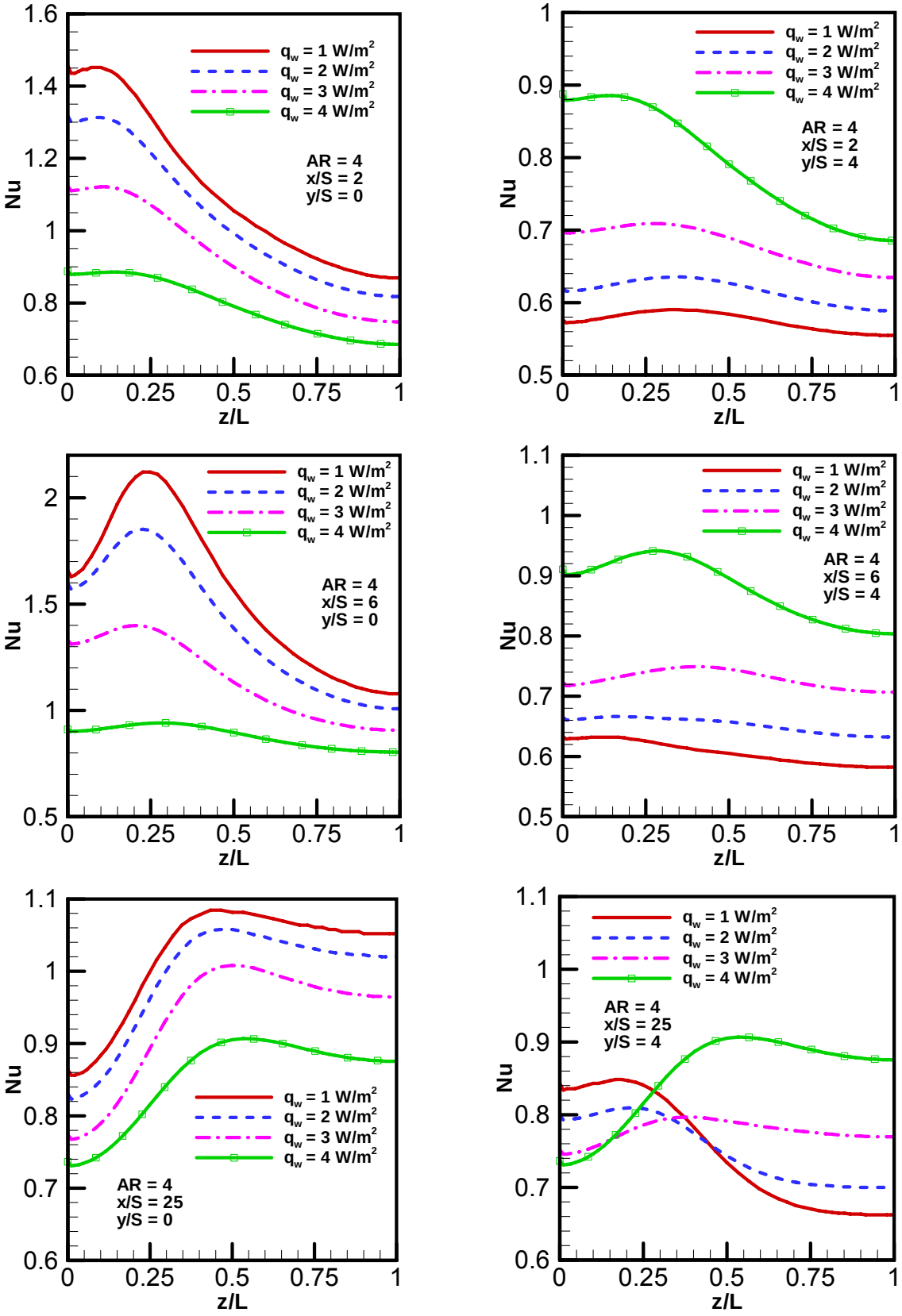

Fig. 6 Effects of wall heat flux on the spanwise distributions of the Nusselt number

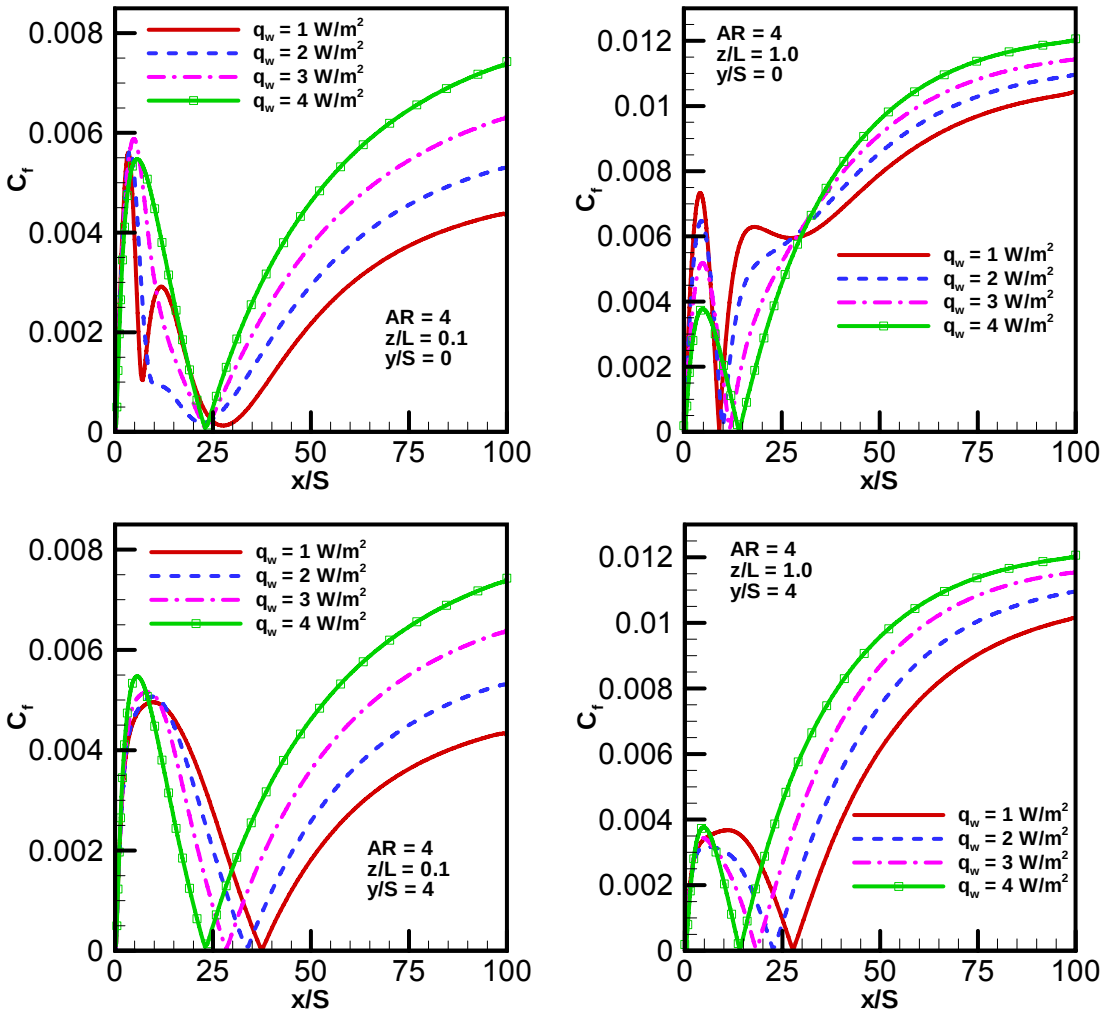

Fig. 7 Effects of wall heat flux on the streamwise distributions of the friction coefficient

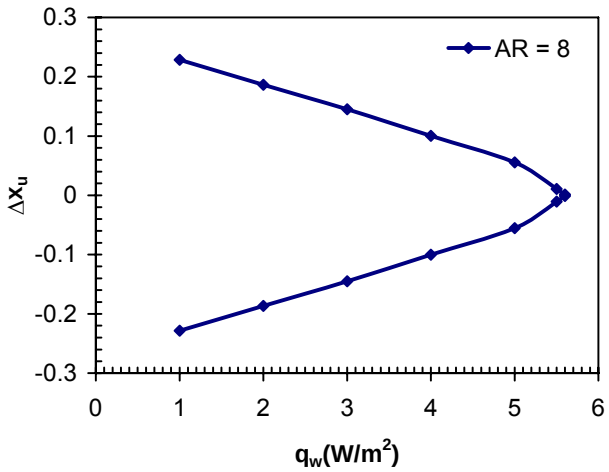

Fig. 8 Bifurcation diagram for $AR = 8$

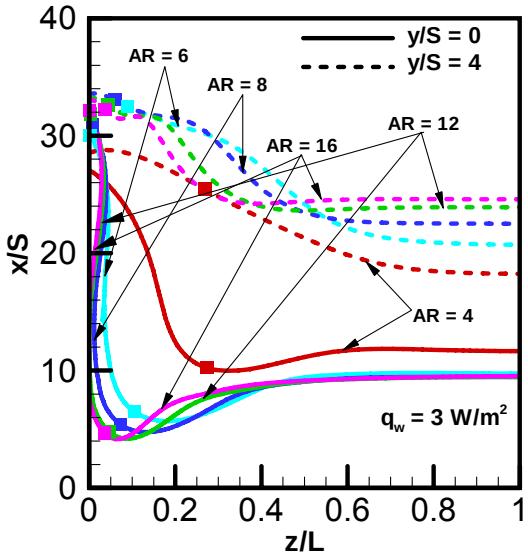

Fig. 9 Effects of duct's aspect ratio on x_u- lines (■ Locations of the jet-like flow impingement)

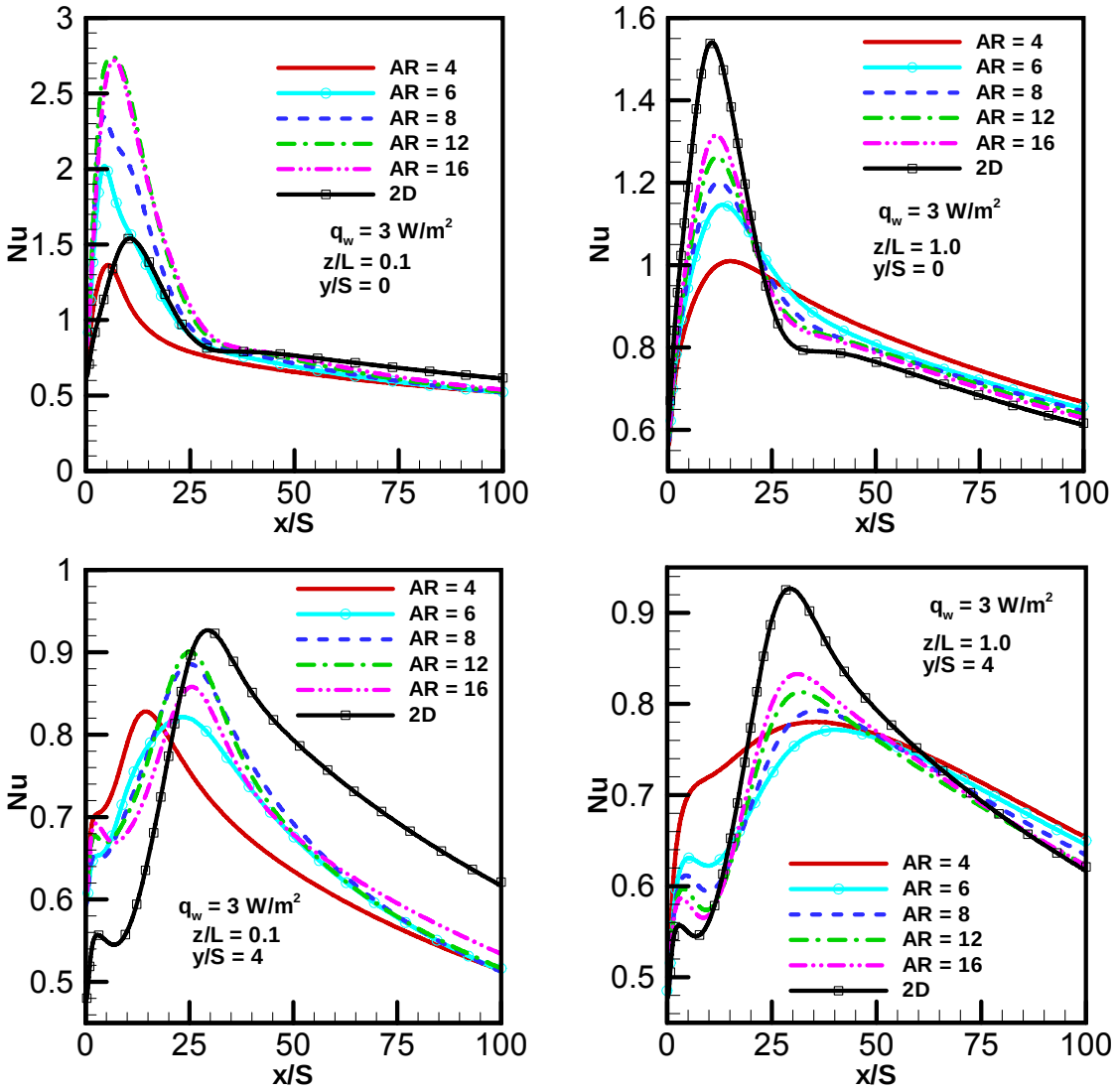

Fig. 10 Effects of duct's aspect ratio on the streamwise distributions of the Nusselt number

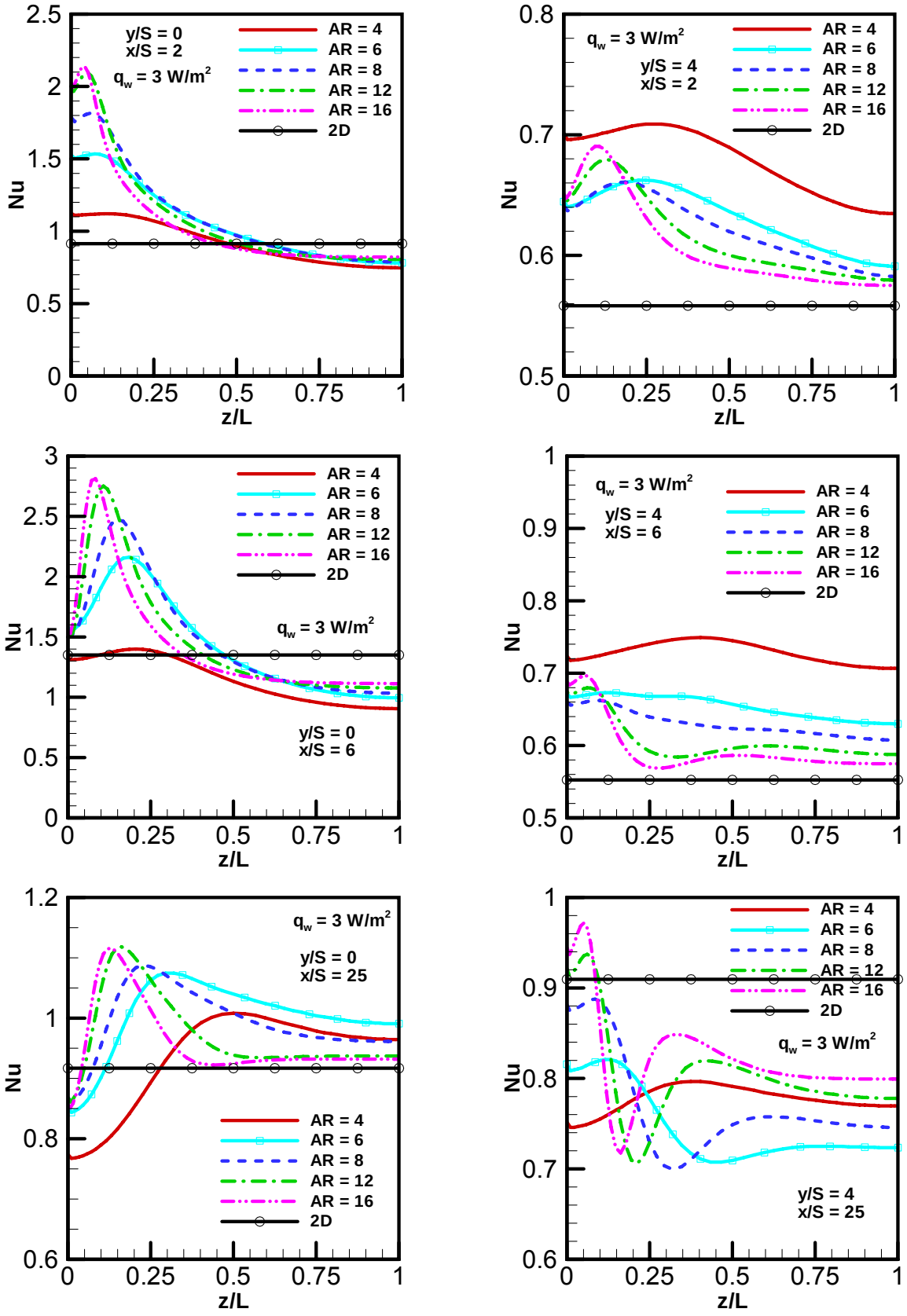

Fig. 11 Effects of duct's aspect ratio on the spanwise distributions of the Nusselt number

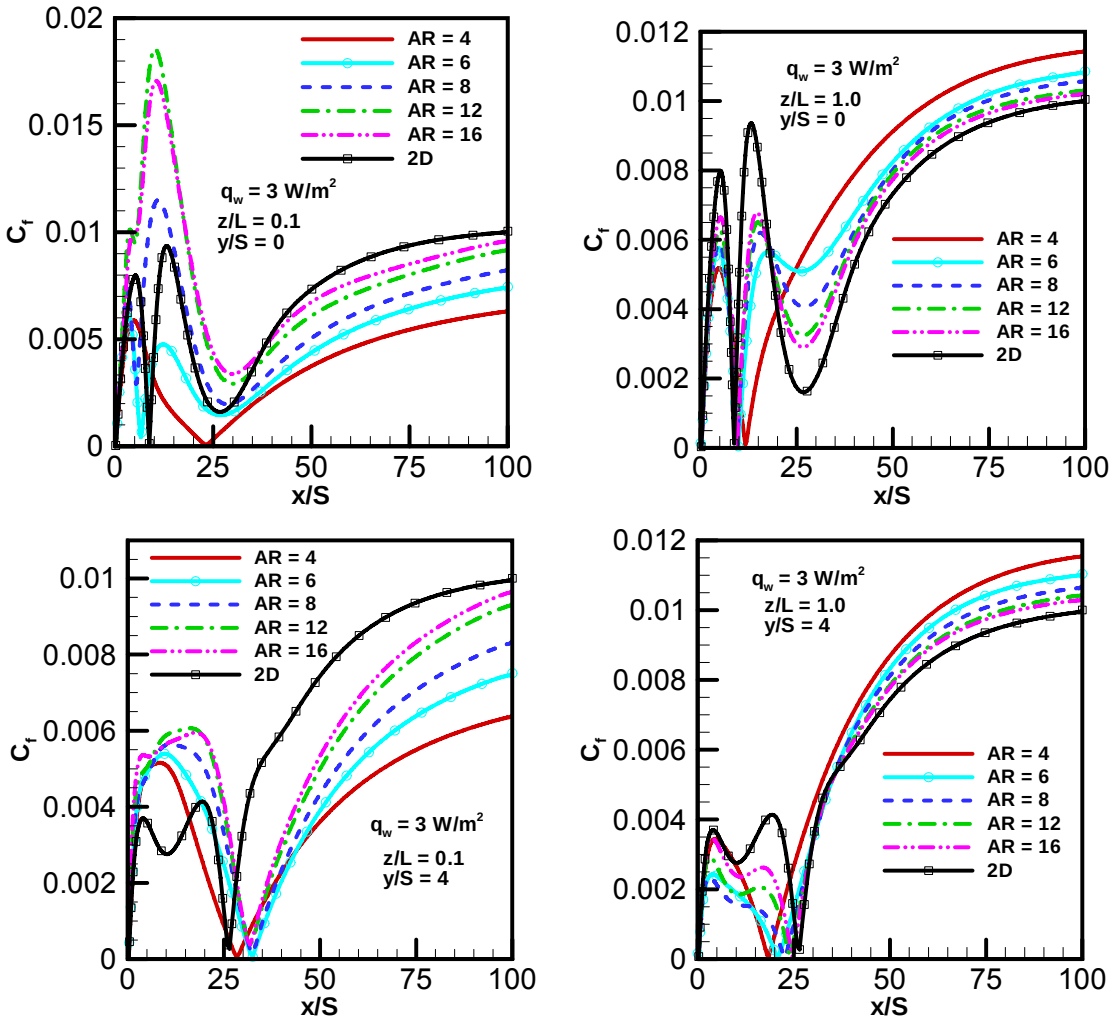

Fig. 12 Effects of duct's aspect ratio on the streamwise distributions of the friction coefficient

III. Three dimensional mixed convection in plane symmetric-sudden expansion: Symmetric flow regime

M. Thiruvengadam, B. F. Armaly and J. A. Drallmeier
Department of Mechanical and Aerospace Engineering
Missouri University of Science and Technology, Rolla, MO 65401, United States
Email: mtwv8@mst.edu, armaly@mst.edu and drallmei@mst.edu

Abstract

Three-dimensional simulations of laminar buoyancy assisting mixed convection in a vertical duct with a plane symmetric sudden expansion are presented to illustrate the effects of the buoyancy assisting force and the duct's aspect ratio on the flow and heat transfer. This geometry and flow conditions appear in many engineering applications, but 3-D heat transfer results have not appeared in the literature. This study focuses on the regime where the flow and thermal fields are symmetric in this geometry. The buoyancy force is varied by changing the heat flux on the stepped walls that are downstream from the sudden expansion, and the duct's aspect ratio is varied by changing the width of the duct while keeping the expansion ratio constant. Results are presented for duct's aspect ratio of 4, 8, 12, 16 and ∞ (2-D flow), and for wall heat fluxes between 5 – 35 W/m^2. The Reynolds number and the range of wall heat flux are selected to insure that the flow remains laminar and symmetric in this geometry and reverse flow does not develop at the exit section of the duct. Results for the velocity, temperature, and the Nusselt number distributions are presented, and the effects of the buoyancy force and the duct's aspect ratio on these results are discussed.

Key words: Laminar mixed convection, Internal flow, Separated flow, Heat transfer, 3-D Numerical simulation

Nomenclature

AR	Upstream aspect ratio = W/h
ER	Expansion ratio = H/h
H	Duct height downstream from the sudden expansion
h	Duct height upstream from the sudden expansion
k	Thermal conductivity
L	Half width of the duct = $W/2$
Nu	Local Nusselt number = $q_w S/k(T_w - T_0)$
$Nu_{step,avg}$	Average Nusselt number on the stepped wall = $q_w S/k(T_{step,avg} - T_b)$
q_w	Wall heat flux = $-k\partial T/\partial n$ at the wall
Re	Reynolds number = $2\rho u_0 h/\mu$
S	Step height
T	Temperature
T_b	Bulk fluid temperature = $\dfrac{\int_0^W \int_0^H u(x,y,z)T(x,y,z)\,dydz}{\int_0^W \int_0^H u(x,y,z)\,dydz}$
T_w	Local wall Temperature
T_0	Inlet fluid temperature
$T_{step,avg}$	Average stepped wall temperature = $\dfrac{1}{L}\int_0^L T_{w,step}\,dz$
$T_{side,avg}$	Average side wall temperature = $\dfrac{1}{H}\int_0^H T_{w,side}\,dy$
u	Velocity component in the x- coordinate direction
u_0	Average inlet velocity

v Velocity component in the y- coordinate direction

W Width of the duct

w Velocity component in the z- coordinate direction

x Streamwise coordinate

x_u Locations where the streamwise velocity gradient is zero ($\partial u/\partial y_{\,at\ wall} = 0$)

y Transverse coordinate

z Spanwise coordinate

Greek symbols

β Volumetric coefficient of thermal expansion

μ Dynamic viscosity

ρ Density

1. Introduction

The separation of flow and its subsequent reattachment due to sudden changes in geometry is a common phenomenon that occurs in many engineering applications such as in electronic cooling equipment, cooling of turbine blades, combustion chambers, and many other heat exchanging devices. Studies for isothermal laminar flow [1-6] in plane symmetric sudden expansion have shown that the flow is steady and symmetric for Reynolds number lower than a critical value, and asymmetric and steady for Reynolds number higher than the critical value. These studies also show that the critical Reynolds number increases with decreasing the aspect ratio and also with decreasing the expansion ratio of the duct. Tsui and Shu [7] and Alimi et al. [8] reported results for 2-D laminar mixed convection for the asymmetric flow regime. Thiruvengadam et al. [9] simulated the bifurcated 3-D forced convection, and in [10] they reported the effect of the buoyancy

force and duct's aspect ratio on that asymmetric flow regime. The introduction of low levels of heating at the stepped walls (buoyancy assisting) caused the level of asymmetry in the flow to decrease for a fixed Reynolds number. The asymmetry ceases to exist in the flow and thermal fields, and a symmetric mixed convection flow regime develops at and beyond a critical level of buoyancy assisting force. The critical value of the buoyancy assisting force (or the wall heat flux) increases as the duct's aspect ratio increases thus reaching its maximum value for a duct with infinite aspect ratio (i.e. 2-D flow) for a fixed Reynolds number. For example, for the geometry and flow conditions that are considered in this study, i.e. duct's expansion ratio of two and Reynolds number of 800, symmetric buoyancy assisting mixed convection flow regime develops for wall heat flux larger than 6.21 W/m^2 for any of the aspect ratios. To the authors knowledge the effects of buoyancy force and duct's aspect ratio on the 3-D laminar symmetric mixed convection flow regime that develops in this geometry has not appeared in the literature and that motivated the present study.

2. Problem and solution procedure

This work, which focuses on the symmetric flow regime, is an extension of the work by Thiruvengadam et al. [9, 10] where the asymmetric flow regime was examined. A schematic of the vertical plane symmetric sudden expansion geometry and the computational domain that is used in this simulation is presented in Fig. 1. The upstream duct height (h) is 0.02 m and the downstream duct height (H) is 0.04 m respectively, resulting in expansion ratio ($ER = H/h$) of 2. The step height (S) is maintained at 0.01 m and the duct's width (W) is varied to examine the effect of upstream aspect ratio ($AR = W/h$) on the results. The origin of the coordinate system is located at the bottom corner of

the sudden expansion as shown in Fig. 1. The directions of the streamwise (x), transverse (y), and spanwise (z) coordinates are shown in that figure. The length of the computational domain is 1.0 m downstream and 0.02 m upstream of the sudden expansion, respectively, i.e. $-2 \le x/S \le 100$. This choice is made to insure that the flow at the inlet section of the duct (x/S = -2) is not affected by the sudden expansion in geometry, and reverse flow does not develop at the exit section of the duct (i.e. starved flow condition at the higher wall heat flux) and can be treated as fully developed. The governing equations for steady laminar, incompressible, three-dimensional, buoyancy assisting mixed convection with constant properties are formulated for the continuity, momentum and energy conservation. Thermal buoyancy effects are modeled using the Boussinesq approximation. Details of the governing equations can be found in Li and Armaly [11] who studied laminar mixed convection effects in 3-D backward facing step and these equations will not be re-stated here due to space limitations. The full elliptic 3-D coupled governing equations are solved numerically using finite volume method to simulate the flow and the temperature fields in this computational domain.

The physical properties are treated as constants and evaluated for air at the inlet temperature of $T_0 = 20^\circ C$ (i.e., density (ρ) is 1.205 kg/m^3, specific heat (C_p) is 1005 J/kg.K, dynamic viscosity (μ) is 1.81x10^{-5} kg/m.s, thermal conductivity (k) is 0.0259W/m.K, and volumetric coefficient of thermal expansion (β) is 0.00341 1/K). Inlet flow (at x/S = -2, $1 \le y/S \le 3$, for all z) is considered to be isothermal ($T_0 = 20^\circ C$), steady, and fully developed. The distribution for the isothermal fully developed streamwise velocity component (u) in rectangular duct that was used in this study is given by Shah and Bhatti [12] and is not repeated here due to space limitations. The other velocity

components (transverse (*v)* and spanwise (*w*)) are set to be equal to zero at that inlet section. The no-slip boundary condition (zero velocities) is applied to all of the wall surfaces. Uniform and constant wall heat flux (q_w) is specified at the two stepped walls (at $y/S = 0$ and 4, $0 \leq x/S \leq 100$, for all z), while other walls (side walls) are treated as adiabatic surfaces. The magnitude of that wall heat flux is varied between 5-35 W/m^2 while keeping the Reynolds number ($Re = 2\rho u_0 h/\mu$, where u_0 is the average inlet velocity) fixed at 800 in order to investigate the effects of the buoyancy assisting force on the flow and heat transfer. Similarly, the magnitude of the wall heat flux is fixed at 15 W/m^2, and the Reynolds number is fixed at 800 while the aspect ratio is varied in order to investigate its effect on the flow and heat transfer. Due to the symmetry of the flow and thermal fields in the spanwise direction for the stated conditions in this geometry, the width of the computational domain is chosen as half of the actual width of the duct, $L = W/2$, and symmetry boundary conditions are applied at the center width of the duct, i.e. at $z = L$, $w = 0$, and the gradient of all the other quantities with respect to z are set equal to zero. Fully developed flow and thermal conditions are imposed at the exit section (at $x/S = 100$, for all y and z) of the calculation domain.

Numerical solution of the governing equations and boundary conditions are performed by utilizing the commercial computational fluid dynamics (CFD) code FLUENT 6.2. The mesh is generated using FLUENT's preprocessor GAMBIT. Hexahedron volume elements are used in the simulation. The residual sum for each of the conserved variables is computed and stored at the end of each iteration, thus recording the convergence history. The convergence criterion required that the scaled residuals be smaller than 10^{-10} for the mass and the momentum equations and smaller than 10^{-11} for

the energy equation. Calculations are performed on DELL workstation, and the CPU time for converged solution for *Re* = 800 is approximately 24 hours. The SIMPLEC algorithm is used for the pressure velocity coupling, and the momentum and energy equations are discretized with the Second Order Upwind scheme in order to improve the accuracy of the simulations. Detailed descriptions of the CFD code may be found in the FLUENT manual.

The computational grid distribution is selected to insure high density near the bounding walls and in the regions of the sudden expansion where high gradients exist, in order to insure the accuracy of the simulation. Grid independence tests were performed using different grid densities for *Re* = 800 for all aspect ratios and the results of the study are reported in [10]. From the grid study for *AR* = 8 a grid of (220 x 64 x 50) is used downstream of the sudden expansion ($0 \le x/S \le 100$) and a grid of (20 x 32 x 50) is used upstream of the sudden expansion ($-2 \le x/S \le 0$) for half of the duct's width ($0 \le z/L \le 1$). This grid size is used for aspect ratios smaller or equal to 8 ($AR \le 8$). A grid of (20x32x60) upstream of the sudden expansion and a grid of (220 x 64 x 60) downstream of the sudden expansion provides grid independent results for aspect ratio *AR* = 16 and this grid size is used for $8 < AR \le 16$. The results for code validation could be found in Thiruvengadam et al. [9, 10].

3. Results and Discussion

3.1. Effects of buoyancy

The effects of buoyancy are examined by fixing the aspect ratio to four (*AR* = 4), expansion ratio to two (*ER* = 2), and the Reynolds number to 800 (*Re* = 800) while changing the magnitude of the constant and uniform wall heat flux (q_w) from 5 to 35

W/m^2. Results for other aspect ratios and Reynolds numbers exhibited similar trend and for that reason they are not presented in this study. Thiruvengadam et al. [10] have shown that for this specific geometry (ER = 2, AR = 4 and Re = 800) a symmetric flow develops when the wall heat flux is larger than 3.52 W/m^2 and asymmetric flow develops for smaller wall heat flux. The complex flow behavior that develops downstream of the sudden expansion has been discussed in detail by Thiruvengadam et al. [9, 10]. A "jet-like" flow develops adjacent to the side walls, in the separating shear layer after the sudden expansion in this geometry, which impinges on the stepped walls to form several recirculation flow regions.

The general flow features in this geometry are presented in Fig. 2 by streamlines at different spanwise planes near the side walls. The primary recirculation flow region that develops downstream from the sudden expansion can be clearly seen in this figure, and its size decreases as the distance from the sidewall toward the center width of the duct increases. The effect of the wall heat flux on the size of the recirculation flow region is presented in Fig. 3 by a presentation of the x_u-lines. The x_u-lines represent the locations where the streamwise component of the wall shear stress is zero ($\mu \frac{\partial u}{\partial y}_{wall} = 0$), and that definition is commonly used to identify the reattachment length in two-dimensional separated flow. The locations of the "jet-like" flow impingement on the stepped wall are shown in Fig. 3 for different levels of wall heat flux. When the heat flux is increased to 35 W/m^2 there is no "jet-like" flow impingement on the stepped walls. Increasing the wall heat flux decreases the size of the recirculation flow region. This is due to the buoyancy induced streamwise velocity component in the recirculation flow region which increases with increasing buoyancy force. The results in Fig. 3 show that

for low wall heat flux of 5 and 10 W/m^2, two reattachment lines are identified with one appearing very close to the sudden expansion region. Increasing the wall heat flux causes one of the reattachment line to move downstream and the other reattachment line to move upstream. Higher wall heat flux causes the recirculation flow region to start lifting partially up and away from the stepped wall at the center width of the duct. Further lifting of the recirculation flow region away from the stepped wall continues as the wall heat flux continues to increase.

The effect of wall heat flux on the transverse distributions of the streamwise velocity and temperature at the center width of the duct and at streamwise locations inside (x/S = 7.0) and outside the recirculation flow region (x/S = 40) are presented in Figs. 4 and 5. The velocity distribution exhibits similar behavior but the effect of buoyancy is more pronounced at larger streamwise location. Increasing the buoyancy force increases the velocity and its gradient near the stepped walls, and in order to maintain mass balance its magnitude at the center height of the duct decreases. Higher buoyancy force results in higher wall and fluid temperature as shown in Fig. 5. The temperature at the center height of the duct, however, is not affected significantly by the increasing buoyancy force in the range of parameters that are examined in this study at the selected streamwise location.

The resulting spanwise distributions of the wall temperature are presented for a fixed wall heat flux (q_w = 15 W/m^2) at different streamwise locations, and for different wall heat flux at a fixed streamwise location (x/S = 7) in Fig. 6. Significant wall temperature variations develop in the spanwise direction, particularly at high wall heat flux. It is interesting to note the difference between the distributions at x/S = 1 and at x/S

= 40. In the fully developed flow regime the wall temperature near the sidewall is higher than that at the center width of the duct, and that is due to the higher streamwise velocity at the center width of the duct. On the other hand near the sudden expansion at $x/S = 1$, the lower wall temperature is near the sidewall and that is due to the relatively strong recirculation flow that develops near the bottom corner and adjacent to the side wall in this geometry. The relatively lower velocity that develops at the center width of the duct at that plane ($x/S = 1$) results in a higher temperature at the center width of the duct. The local minimum that appears in the other distributions is due to the "jet-like" flow impingement on the stepped wall, and a higher wall heat flux results in a higher wall temperature

The effect of wall heat flux on the streamwise distribution of local Nusselt number (based on the inlet fluid temperature) is presented at $z/L = 0.1$ and 1.0 in Fig. 7. The expected streamwise distribution of a developing peak in the neighborhood of the reattachment region followed by a gradual decrease with increasing distance from the sudden expansion is observed. The results show that a higher Nusselt number occurs near the side wall ($z/L = 0.1$) than at the center width of the duct. Higher wall heat flux is associated with a higher Nusselt number. The local minimum that develops near the sudden expansion in these distributions for higher wall heat flux is due to the partial lifting of the recirculation flow region away from the stepped wall as shown in Fig. 3 and the resulting higher fluid temperature that flows adjacent to the wall in that region. The difference in the local Nusselt number distributions at $z/L = 0.1$ and at $z/L = 1$ demonstrates the significant effect of the three-dimensional flow behavior on the results.

The effect of wall heat flux on the streamwise distributions of the average stepped wall temperature ($T_{step,avg}$) and the average side wall temperature ($T_{side,avg}$) are shown in Figs. 8 and 9 respectively. These temperatures increase with increasing wall heat flux and show a linear increase downstream from the reattachment region that is similar to what is observed in fully developed flow region in a duct. The average sidewall temperature is lower than the average stepped wall temperature and the "jet-like" flow impingement is associated with the minimum that appears in these distributions. The effect of wall heat flux on the streamwise distribution of the bulk fluid temperature (T_b) is shown in Fig. 10. It increases with increasing wall heat flux and streamwise distance, and develops a constant slope after the reattachment region. The small non-linearity that appears in that distribution after the sudden expansion is due to the recirculation flow that develops in that region.

The effect of wall heat flux on the streamwise distribution of the average Nusselt number on the stepped wall (based on the bulk fluid temperature) is presented in Fig. 11. Its magnitude increases with increasing wall heat flux and it has a linear variation in the fully developed region of the flow. For the lower wall heat flux cases of $q_w \leq 15$ W/m^2, its magnitude increases rapidly with distance from the sudden expansion then gradually continues to increase as the distance increases. The results in Fig. 11 show a different trend than those in Fig. 7 and that is due to the fact that the bulk fluid temperature, that varies with distance from the sudden expansion, is used in the calculations of the average Nusselt Number (Fig. 11) while the inlet fluid temperature, that is fixed at 20^{o}C, is used in the calculations of the local Nusselt number (Fig. 7).

3.2. Effects of aspect ratio

The effect of aspect ratio on the flow and heat transfer in this geometry is examined by keeping the expansion ratio, the Reynolds number and the wall heat flux constant at $ER = 2.0$, $Re = 800$, and $q_w = 15$ W/m^2 respectively, while varying the aspect ratio (AR) between 4 and infinity (2-D) by selecting different duct's width of the duct. The effect of the aspect ratio on the size of the recirculation flow region is shown in Fig. 12 by presenting the distribution of the x_u-lines. These results show that the recirculation flow region is totally attached to the stepped wall for the cases with higher aspect ratios but start to partially lift away from the stepped wall as the aspect ratio decreases. These results show that a higher level of wall heat flux is required to partially lift the recirculation flow region away from the stepped wall as the aspect ratio increases. The "jet-like" flow impingement locations that are identified in this figure move downstream and closer to the side wall as the aspect ratio increases.

The effect of aspect ratio on the transverse distribution of the streamwise velocity component at the center width of the duct and at streamwise locations of $x/S = 7$ and 40 are presented in Fig. 13. A smaller reattachment length and a higher center line velocity develop for smaller aspect ratios. The effect of the aspect ratio on the fluid temperature at the center width of the duct at these planes is negligible, and for that reason it is not presented graphically. The effect of aspect ratio on the spanwise distribution of the wall temperature at $x/S = 7$ is presented in Fig. 14. The minimum that appears in these distributions close to the side wall is due to the "jet-like" flow impingement on the wall in that region. That minimum decreases and moves closer toward the center width of the duct as the aspect ratio decreases.

The streamwise distribution of the local Nusselt number (based on the inlet fluid temperature) at a location near the side wall (z/L = 0.1) and at the center width of the duct (z/L = 1) is presented in Fig 15. A peak develops in its distribution near the reattachment region and that peak increases as the aspect ratio increases. The aspect ratio continues to significantly influence the results near the side wall for ducts with large aspect ratio. The 2-D simulation results are presented in these figures for comparison and they show that the results from the AR = 16, relatively wide duct, are approaching those from the 2-D simulations at the center width of the duct but that is not the case near the side wall. The relatively lower stepped wall temperature that develops near the side wall, as compared to its center width value (3-D effects), contributes to this behavior and that effect continues to be significant in this region for ducts with large aspect ratio. In the fully developed flow region the local Nusselt number increases with the increase in the aspect ratio near the side wall, but that trend is reversed at the center width of the duct as shown in Fig. 15. The maximum local Nusselt number increases and its location moves closer toward the side wall as the aspect ratio increases as can be seen from the results that are tabulated in Table 1 for wall heat flux of 15 W/m^2.

Table 1 Magnitudes and locations of maximum local Nusselt number (for q_w = 15 W/m^2 & Re = 800)

x/S	y/S	z/L	Nu_{max}	AR
8.494	0	0.3464	1.079	4
8.752	0	0.2707	1.122	6
8.752	0	0.2053	1.14	8
9.560	0	0.1475	1.153	12
9.840	0	0.1069	1.154	16
16.362	0		0.976	2-D

The effect of the duct's aspect ratio on the streamwise distribution of the average stepped wall temperature ($T_{step,avg}$) is presented in Fig 16. These results show that this temperature decreases rapidly after the sudden expansion, reaching a minimum near the flow reattachment region, and increasing linearly in the fully developed flow region. The results show that the average stepped wall temperature is not affected significantly by the duct aspect ratio. There is a slight decrease with increasing the aspect ratio in the fully developed flow region. The streamwise distribution of the bulk fluid temperature (T_b) is presented in Fig. 17 and it exhibits a linear behavior after the reattachment region, and as expected it is independent of the aspect ratio. The changes in the streamwise distribution of the average side wall temperature due to changes in the aspect ratio is insignificant for aspect ratio larger than 6 and for that reason that behavior is not presented graphically.

The effect of the aspect ratio on the streamwise distribution of the average Nusselt number ($Nu_{step,avg}$) is presented in Fig 18. The results show a steep increase in its magnitude in the recirculation flow region followed by a lower rate of increase after that region. The local maximum that appears normally in the local Nusselt number distribution (that uses the constant inlet fluid temperature in its definition) as shown in Fig.15, does not appear in the distribution of the average Nusselt number ($Nu_{step,avg}$) due to the use of the bulk fluid temperature in its definition. These results approach the 2-D values as the aspect ratio increases. A slightly higher average Nusselt number develops in the region near the sudden expansion for ducts with lower aspect ratio but that trend is reversed in the fully developed region of the flow. The change in the aspect ratio has only small effect on the average Nusselt number distribution.

4. Conclusions

The effect of buoyancy force and duct's aspect ratio on the flow and heat transfer in laminar 3-D buoyancy assisting mixed convection in plane symmetric sudden expansion is presented for the case when the flow and thermal fields are symmetric. As buoyancy level increases the size of the recirculation flow region decreases and the reattachment line moves toward the sudden expansion. A partial lifting of the reattached flow starts to develop at the center width of the duct and the lifting continues to increase with increasing level of buoyancy. Higher buoyancy level results in a higher wall and bulk fluid temperature and also a higher local and average Nusselt number. The maximum local Nusselt number develops in a region close to the side walls. Increasing buoyancy level increases the velocity and its gradient near to the stepped wall but decreases its magnitude at the center height of the duct. The temperature at the center height of the duct is not affected significantly by increasing the buoyancy level in the range of parameters that are examined in this study.

Decreasing the aspect ratio for a fixed buoyancy level causes the reattachment line to move upstream closer to the sudden expansion and initiating partial lifting of the recirculation flow region away from the stepped wall. A higher aspect ratio requires a higher buoyancy level to partially lift the recirculation flow region away from the stepped wall. The effect of the aspect ratio on the local Nusselt number near the side wall continues to be significant for ducts with large aspect ratio but that is not the case at the center width of the duct. Increasing the aspect ratio increases the local Nusselt number in the fully developed flow region near the side wall but that trend is reversed at the center width of the duct. Increasing the aspect ratio increases the maximum local Nusselt

number and moves its location closer toward the side wall. The aspect ratio does not affect the bulk fluid temperature and has only a small effect on the average Nusselt number.

Acknowledgement

This work has been supported in part by a DOE-Basic Energy Sciences grant No. DE-FG02-03ER46067, and by an NSF grant No. CTS-0352135.

References

[1] F. Durst, A. Melling, J.H. Whitelaw, Low Reynolds number flow over a plane symmetric sudden expansion, J. Fluid Mech. 64 (1974) 111-128.

[2] W. Cherdron, F. Durst, J.H. Whitelaw, Asymmetric flows and instabilities in symmetric ducts with sudden expansions, J. Fluid Mech. 84 (1978) 13-31.

[3] F. Durst, J.C.F. Pereira, C. Tropea, The plane symmetric sudden-expansion flow at low Reynolds numbers, J. Fluid Mech. 248 (1993) 567-581.

[4] R.M. Fearn, T. Mullin, K.A. Cliffe, Nonlinear flow phenomena in a symmetric sudden expansion, J. Fluid Mech. 211 (1990) 595-608.

[5] D. Drikakis, Bifurcation phenomena in incompressible sudden expansion flows, Phys. Fluids 9 (1997) 76-87.

[6] T. Hawa, Z. Rusak, The dynamics of a laminar flow in a symmetric channel with a sudden expansion, J. Fluid Mech. 436 (2001) 283-320.

[7] Y.Y. Tsui, S.J. Shu, Effects of buoyancy and orientation on the flow in a duct preceded with a double-step expansion, Int. J. Heat Mass Transfer 41 (17) (1998) 2687-2695.

[8] S.E. Alimi, J. Orfi, S.B. Nasrallah, Buoyancy effects on mixed convection heat and mass transfer in a duct with sudden expansions, Heat Mass Transfer 41 (2005) 559-567.

[9] M. Thiruvengadam, J.H. Nie, B.F. Armaly, Bifurcated three-dimensional forced convection in plane symmetric sudden expansion, Int. J. Heat Mass Transfer 48 (2005) 3128-3139.

[10] M. Thiruvengadam, B.F Armaly, J.A. Drallmeier, 2007, Three-dimensional mixed convection in plane symmetric-sudden expansion: Bifurcated flow regime, ASME J. Heat Transfer 129 (2007) 819 – 826.

[11] A. Li, B.F. Armaly, Mixed convection adjacent to 3-D backward-facing step, Proceedings of the ASME-IMECE Conference, ASME HTD, 366-2, New York, 2000, pp. 51 – 58.

[12] R.K Shah, M.S. Bhatti, Laminar Convective Heat Transfer in Ducts: S. Kakac, R. K.Shah, W. Aung (Eds.), Handbook of Single-Phase Convective Heat Transfer, John Wiley & Sons, New York, 1987, pp. 3.45-3.47.

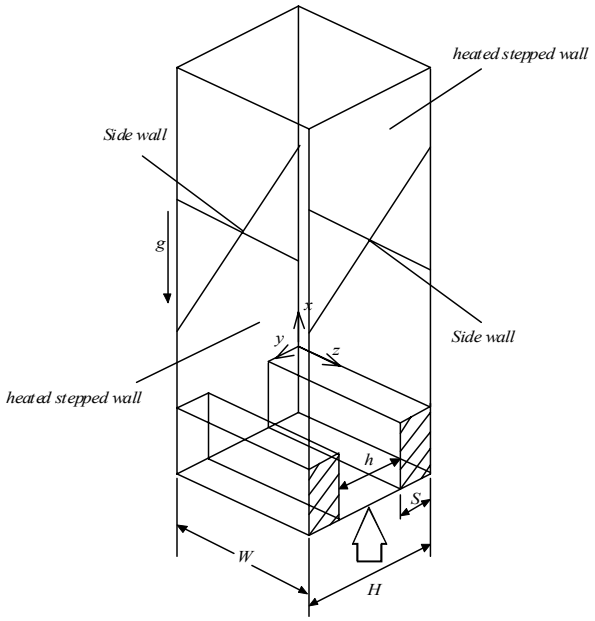

Fig. 1 Schematic of the computational domain

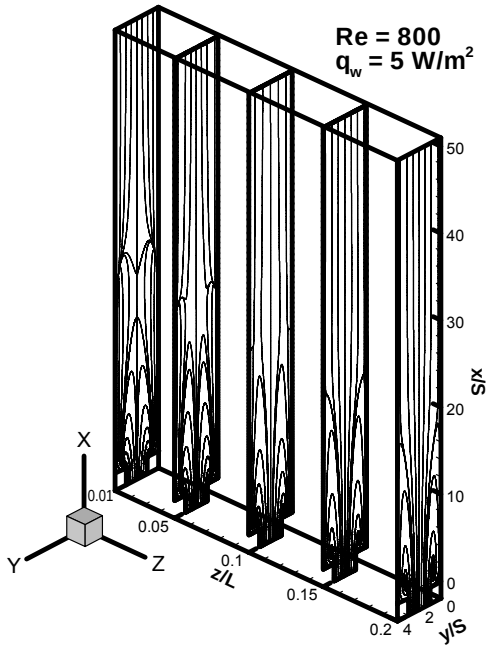

Fig. 2 General flow behavior for q_w = 5 W/m^2

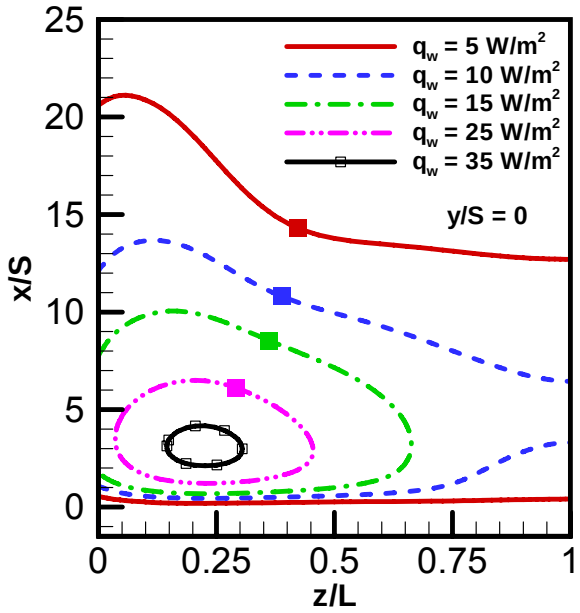

Fig. 3 Distribution of the x_u lines on the stepped wall
(■ Location of the "jet-like" flow impingement)

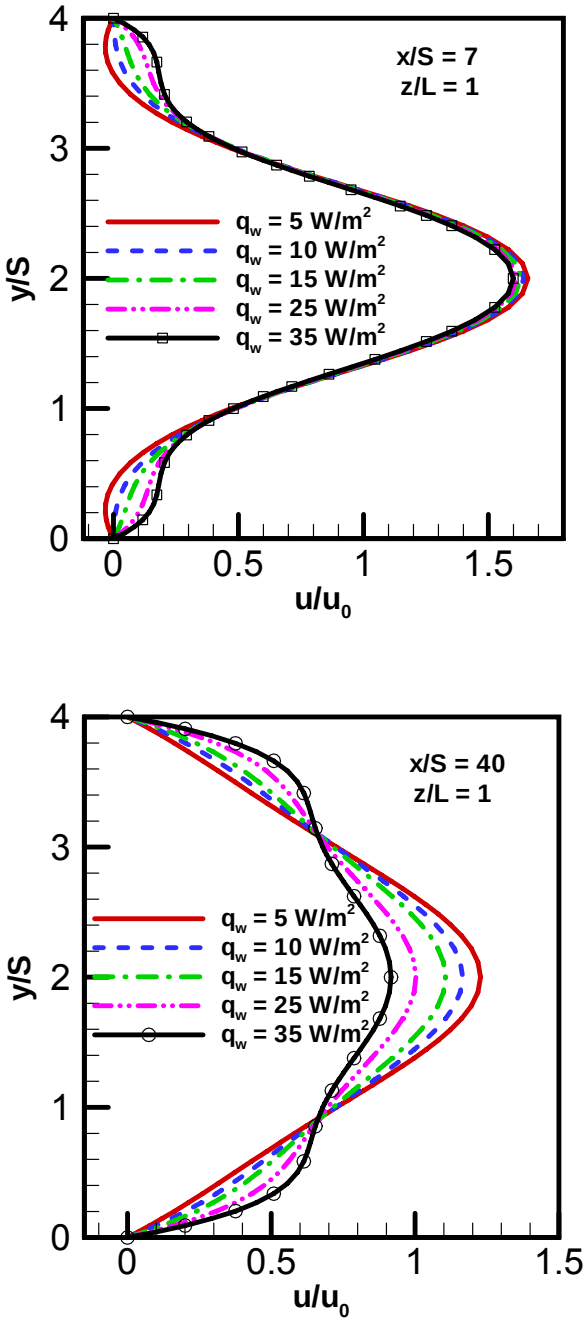

Fig. 4 Streamwise velocity distribution

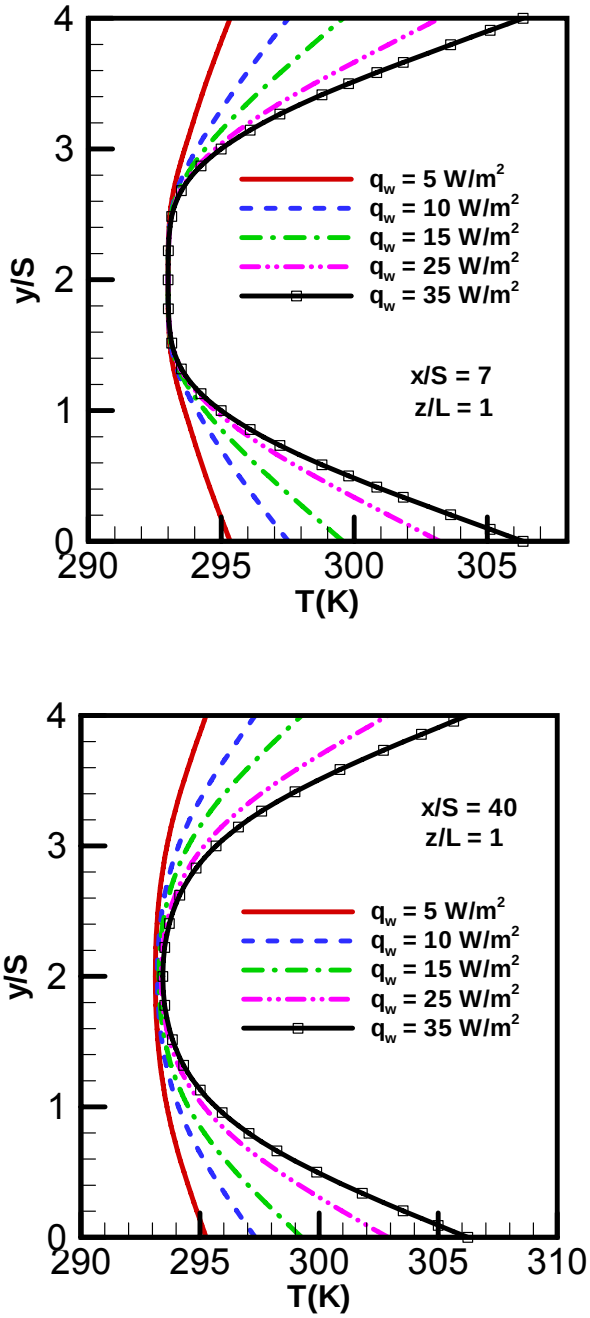

Fig. 5 Fluid temperature distribution

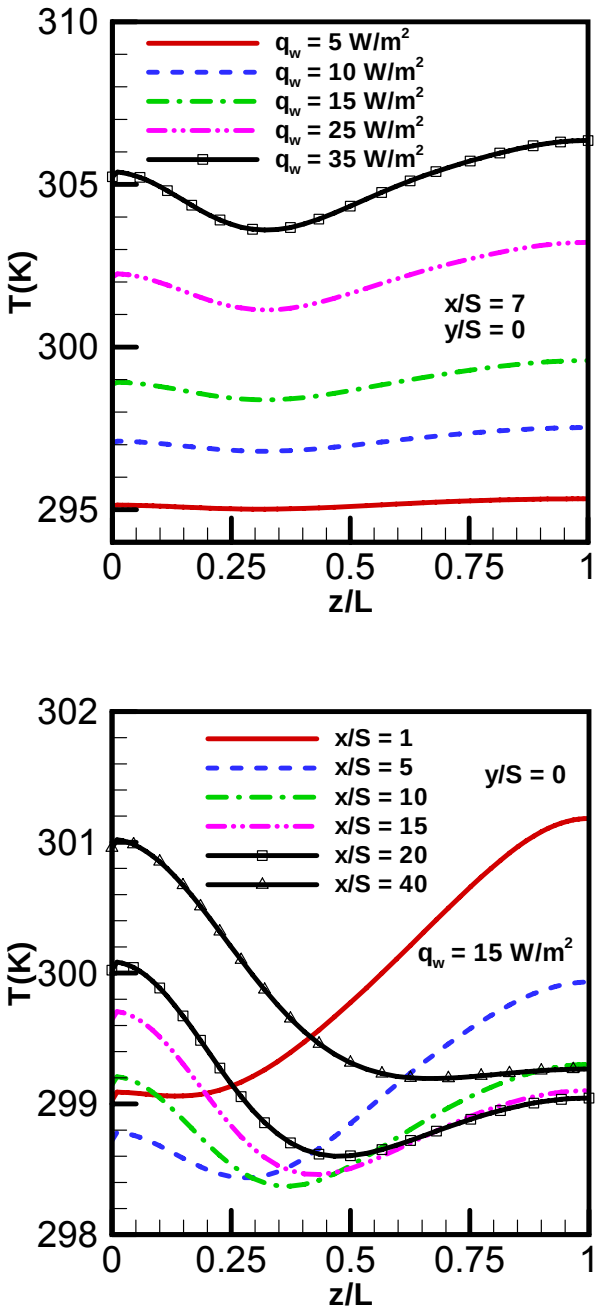

Fig. 6 Spanwise distribution of the stepped wall temperature

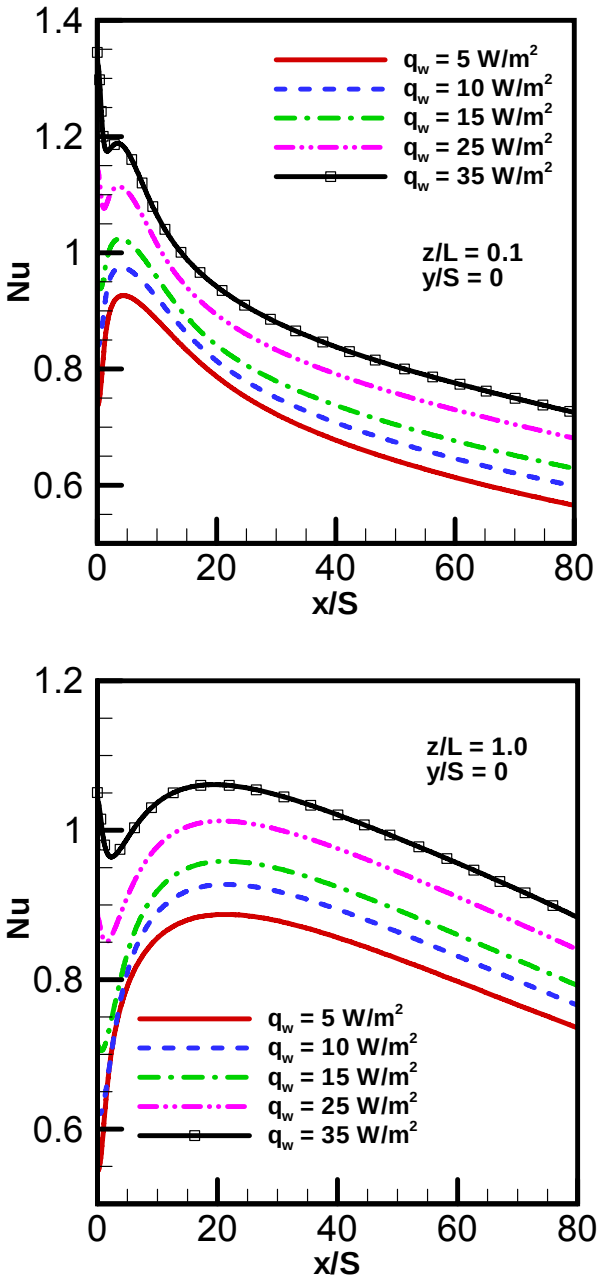

Fig. 7 Local Nusselt number distribution

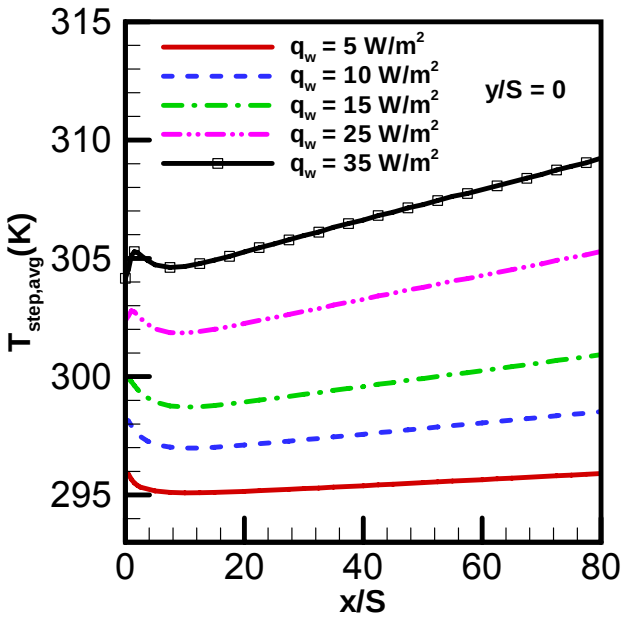

Fig. 8 Streamwise distribution of the average stepped wall temperature

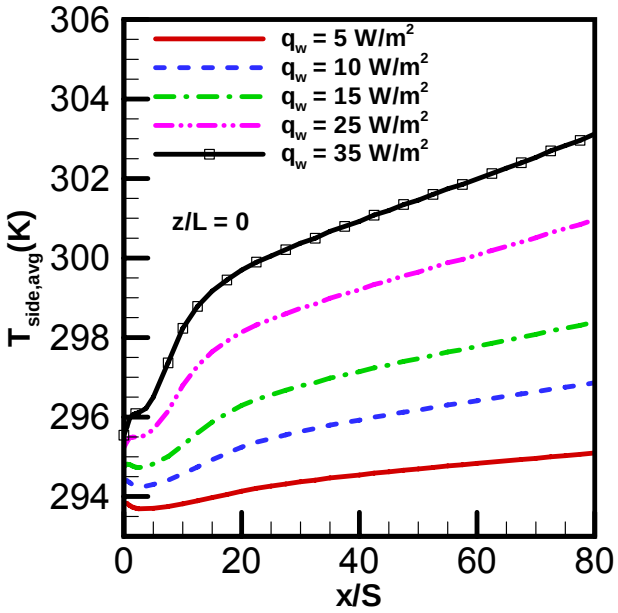

Fig. 9 Streamwise distribution of the average side wall temperature

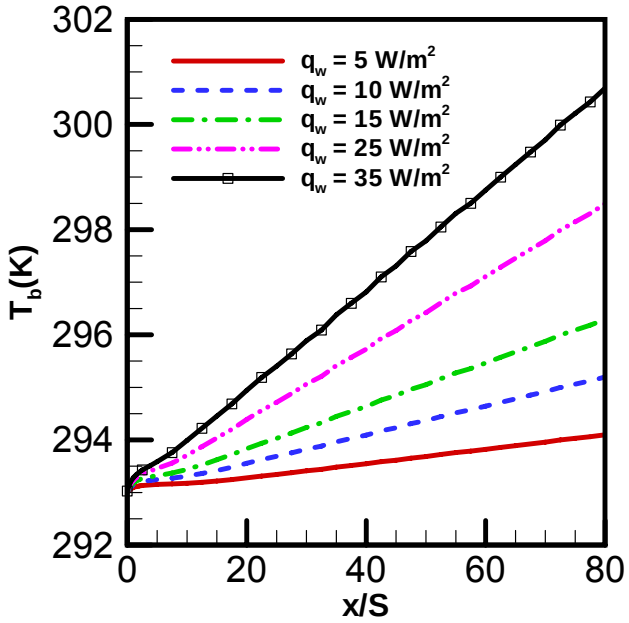

Fig. 10 Streamwise distribution of the bulk fluid temperature

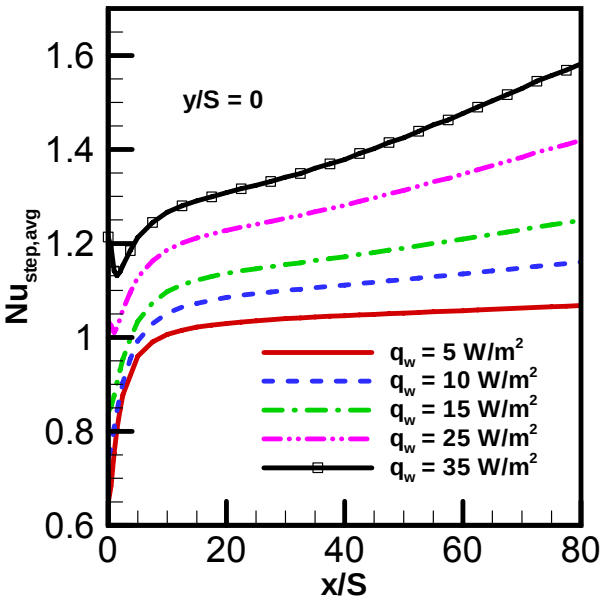

Fig. 11 Streamwise distribution of the average Nusselt number

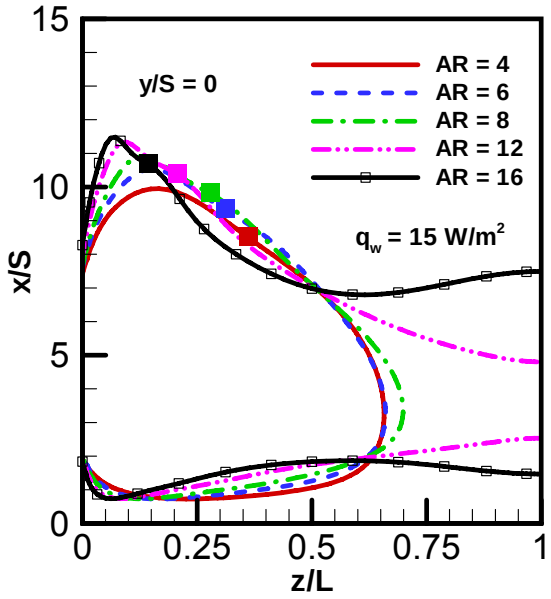

Fig. 12 Effect of aspect ratio on the distribution of the x_u lines
(■ Location of the "jet-like" flow impingement)

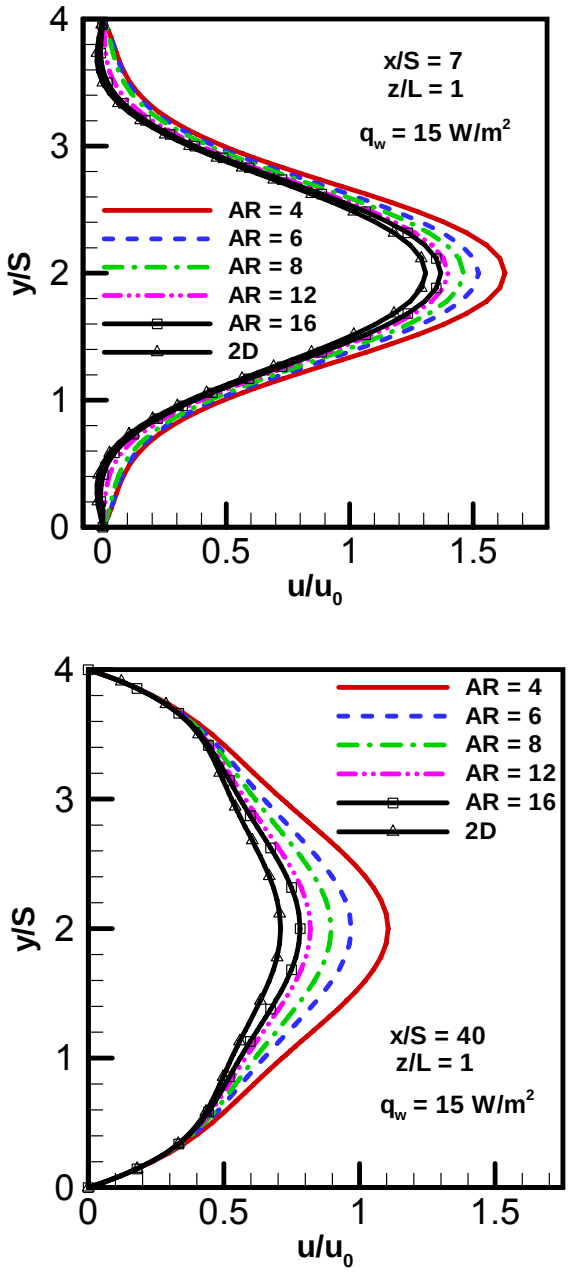

Fig. 13 Effect of aspect ratio on the transverse distribution of the streamwise velocity

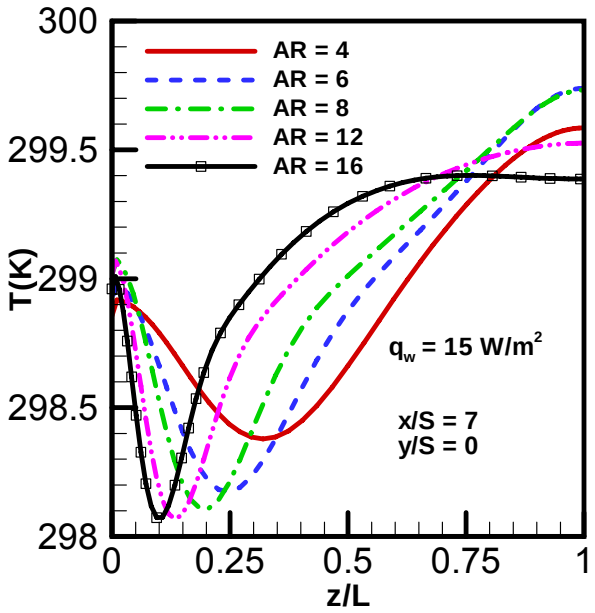

Fig. 14 Effect of aspect ratio on the spanwise distribution of the stepped wall temperature

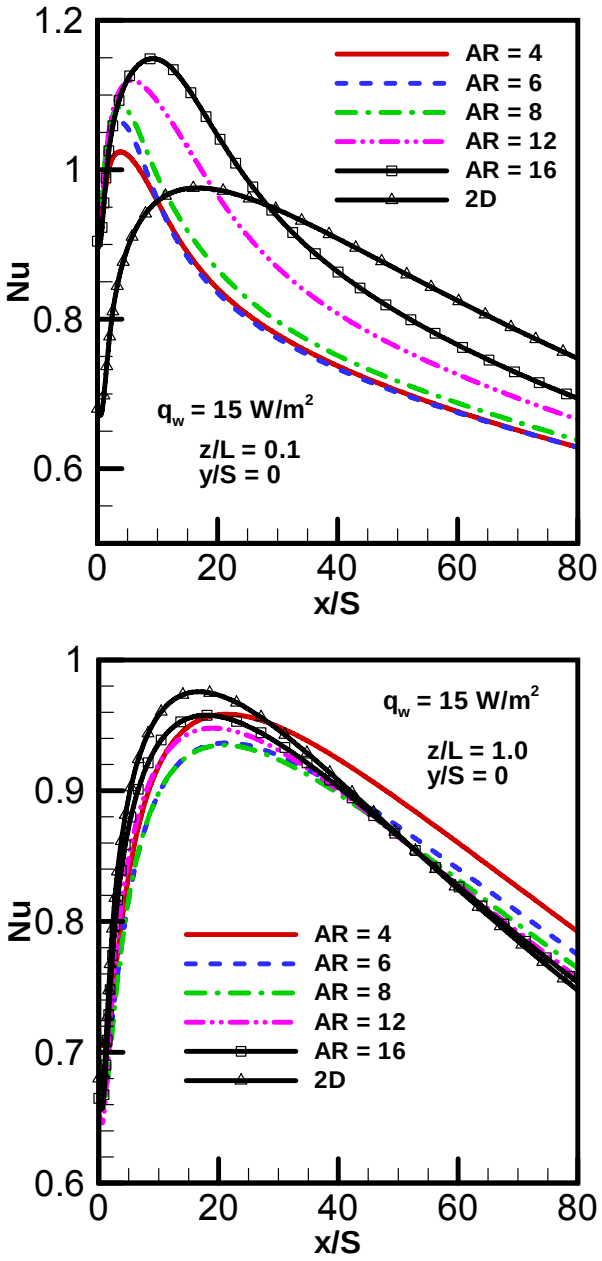

Fig. 15 Effect of aspect ratio on the local Nusselt number distribution

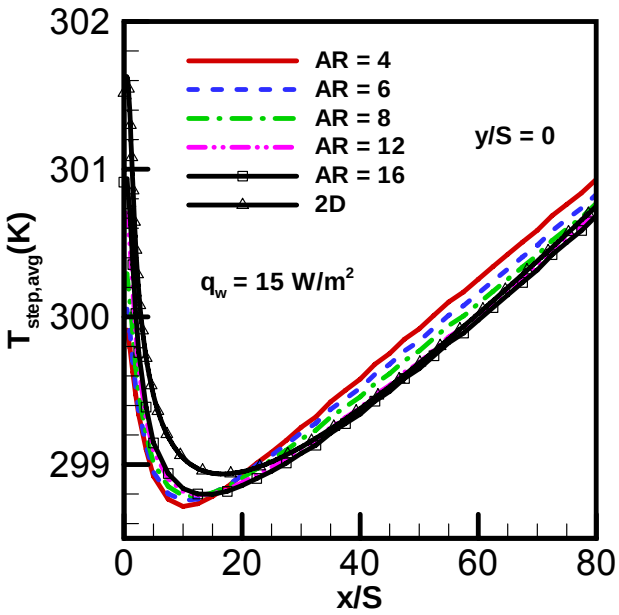

Fig. 16 Effect of aspect ratio on the streamwise distribution of the average stepped wall temperature

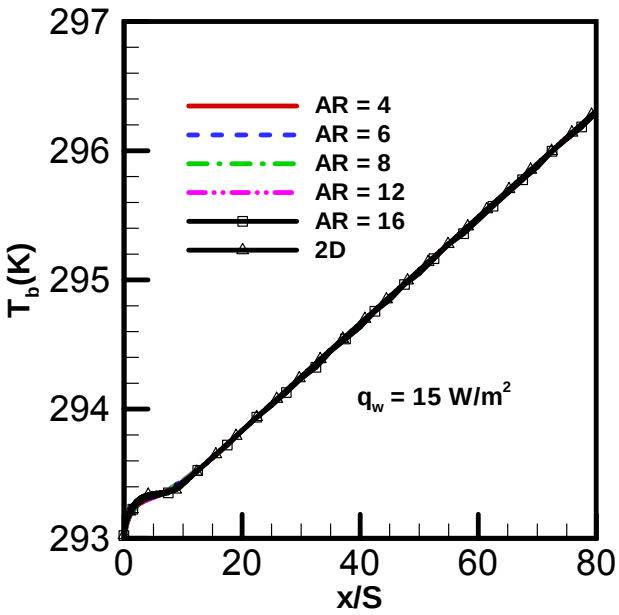

Fig. 17 Effect of aspect ratio on the streamwise distribution of the bulk fluid temperature

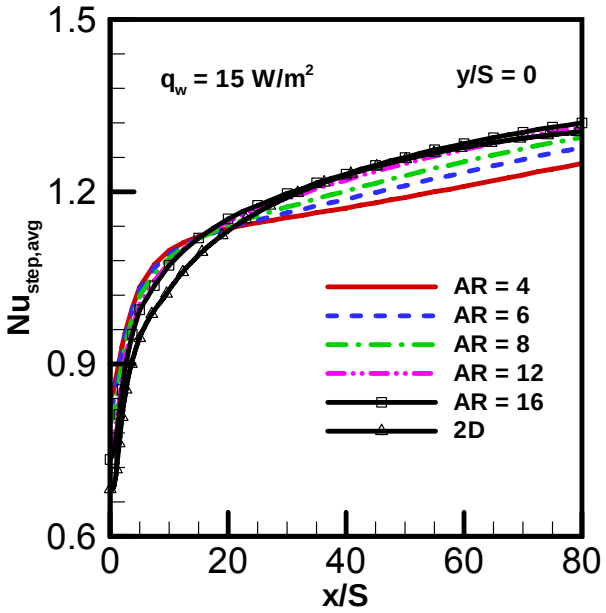

Fig. 18 Effect of aspect ratio on the streamwise distribution of the average Nusselt number

IV. Measurements in three-dimensional separated flow

M. Thiruvengadam, B. F. Armaly and J. A. Drallmeier
Department of Mechanical and Aerospace Engineering
Missouri University of Science and Technology, Rolla, MO 65401
Email: mtwv8@mst.edu, armaly@mst.edu and drallmei@mst.edu

Abstract

Velocity measurements in three-Dimensional (3-D) separated flow adjacent to backward–facing step are performed using 3-D Laser Doppler Velocimeter and the results are reported for Reynolds number ranging from laminar to turbulent flow. Measured reattachment length and its spanwise distributions along with the transverse distribution of the mean streamwise velocity component at the center of the duct at one streamwise location are presented for laminar, transition and turbulent flow regime. The reattachment length at the center of the duct increases with the increase in the Reynolds number in the laminar flow regime but starts to decrease as the transition regime develops and it becomes independent of the Reynolds number in the turbulent flow regime. The spanwise distribution of the reattachment length exhibits a peak at the center and a minimum near the side walls with its maximum value developing at the side wall for the laminar flow regime. The magnitude of the negative mean streamwise velocity component increases in the recirculation region as the Reynolds number increases. Turbulent flow measurements for one Reynolds number of 8631 and the three velocities components along with their turbulent Reynolds stresses are presented at different streamwise and spanwise locations in the separated flow regime. Measurements are compared with simulations using existing turbulence models that are available in the FLUENT CFD code.

Nomenclature

A Upstream duct cross-sectional area = W x h

AR Upstream aspect ratio = W/h

AR_1 Downstream aspect ratio = W/H

D_h Upstream duct hydraulic Diameter = $4A/P$

ER Expansion ratio = H/h

H Duct height downstream from the step

h Duct height upstream from the step

L Half width of the duct

P Upstream duct perimeter = $2(W+h)$

Q Volumetric flow rate

Re Reynolds number = $\rho u_0 D_h/\mu$

S Step height

$\bar{u}$ Mean velocity component in the x- coordinate direction = u_{avg}

$\overline{u'^2}$ Normal Reynolds stress component in the in the x- coordinate direction = u'^2_{avg}

k Turbulent Kinetic Energy = $\frac{1}{2}\left(\overline{u'^2}+\overline{v'^2}+\overline{w'^2}\right)$

u_0 Average inlet velocity

$\bar{v}$ Mean velocity component in the y- coordinate direction = v_{avg}

$\overline{v'^2}$ Normal Reynolds stress component in the in the y- coordinate direction = v'^2_{avg}

W Width of the duct

$\bar{w}$ Mean velocity component in the z- coordinate direction

$\overline{w'^2}$ Normal Reynolds stress component in the in the z- coordinate direction = w'^2_{avg}

$\overline{u'v'}$ Reynolds shear stress

x Streamwise coordinate

y Transverse coordinate

z Spanwise coordinate

x_u Locations where the streamwise wall shear stress is zero $\partial u/\partial y\big|_{y=0} = 0$

Greek symbols

μ dynamic viscosity

ρ density

1. Introduction

Flow separation and its subsequent reattachment occurs normally when sudden expansion in geometry occurs in both internal and external flow applications like electronic cooling equipment, cooling of turbine blades, combustion chambers and other heat exchanging devices. The flow and heat transfer in these devices exhibit three-dimensional behavior but most of the published results are two-dimensional. The backward-facing step geometry has been used extensively in benchmark studies of separated flow due to its relative simplicity [1-2] and several experimental and numerical studies have been published for two-dimensional laminar flow [3-5]. Armaly et al. [3] noted that 3-D features start to develop in such a geometry with aspect ratio of AR_1 =18 for Reynolds number greater than 600 -1000 where the flow starts its transition from laminar to turbulent and that a fully turbulent flow develops at Reynolds number greater than 7000. Three-dimensional flow behavior increases in significance as the aspect ratio decreases but only a limited number of results have been published for that case

particularly for turbulent flow. The laminar simulations of Iwai et al. [6] demonstrated that an aspect ratio of AR = 16 is needed to maintain two-dimensional flow at the center of the duct for Re = 250. Measurements by Shih and Ho [7] in such a geometry with small aspect ratio illustrated that the flow inside the recirculation region exhibit strong 3-D behavior. Similarly the measurements of Lim et al. [8] illustrate that the reattachment length in this geometry with small aspect ratio is shorter than its equivalent value for the two-dimensional case. Measurements by Papadopoulus and Ottugen [9] illustrate the effects of aspect ratio on the centerline velocities and Reynolds shear stresses. Two-component laminar velocity measurements by Armaly et al. [10] in a geometry with aspect ratio of AR = 8 revealed significant 3-D effects. The simulations of the same geometry as in [10] by Nie and Armaly [11] established that the two-dimensional definition for the location of reattachment region could not be used for the three-dimensional flow cases due to the strong spanwise velocity that develops inside the recirculation region near the wall. For the same geometry as in [10], Nie and Armaly [12] presented a limited number of measurements for the spanwise distributions of the reattachment line as a function of the Reynolds number. In the present study, measurements in the same geometry are expanded to include additional Reynolds numbers that cover the laminar, transition, and fully turbulent flow regimes along with some streamwise velocity components. In addition, the turbulent flow in this geometry at Reynolds number of Re = 8631 is examined in more details by measuring the three velocity components and their fluctuations at different streamwise and spanwise locations in order to deduce the mean velocities, Reynolds stresses, and turbulent kinetic energy distributions in the separated flow region. To the authors knowledge such measurements

have not been reported in the literature for this geometry and that motivated the present study.

2. Experimental facilities and procedures

2.1. Air tunnel system

A schematic of the air flow path from the high pressure tank of the compressor to and through the test section of the air tunnel is shown in Fig. 1. The air flow passes through a pressure regulating valve, flow rotameters section, jet atomizer section, and a mixing tank prior to its entry into the inlet section of the air tunnel. The pressure regulating valve is used to maintain a constant inlet air pressure at 50 psig. A set of three calibrated rotameters that are connected in parallel with each other through control valves are used to measure and adjust the volume air flow rate. Only one of the three rotameters is activated for a particular level of air flow rate while the other two rotometer are isolated from the flow path. The jet atomizer section consists of six jets that can be independently controlled, is used to seed part of the air flow that is diverted into the atomizer with olive oil particles that have an average diameter of 0.6μm and are used to facilitate scattering for LDV measurements. The fraction of the air flow that is diverted through the atomizer section is controlled and varied depending on the total air flow rate. The mixing tank mixes the air stream that passes through the atomizer with the one that bypassed the atomizer to generate a uniformly mixed air flow that enters the inlet section of the air tunnel. This air flow path is an open path and is vented from the exit section of the air tunnel to the outside ventilation system. The flow is maintained at a constant rate throughout a given experimental run.

A schematic of the air tunnel is shown in Fig 2 and it consists of an inlet treatment section, a developing flow section, a test section and an exit section. The flow treatment section consists of a diverging-converging nozzle that is connected by a short straight duct. The diverging part of the nozzle is packed up with fine steel wool mesh for the purpose of breaking up any large oil particles that might have developed in the seeded air flow. The straight duct is packed with plastic honey-comb material to straighten the flow before it enters into the converging nozzle. The converging nozzle has an area ratio of 10:1 and its smaller section is connected directly to the developing flow section of the air tunnel. That duct section, which has a width of 7.92 cm and a height of 0.96 cm, is 2 m long and connects the converging nozzle to the test section of the air tunnel. This length ensures that the inlet air flow to the test section is fully developed.

The test section of the air tunnel is equivalent to a backward- facing step in a duct and a schematic of that section is shown in Fig 3. This backward-step geometry has a step height (S) of 1.06 cm and the width (W) of 7.92 cm. The upstream connecting duct height (h) is 0.96 cm and the height of the downstream duct (H) is 2.02 cm. This provides an aspect ratio ($AR = W/h$) of 8.25 and expansion ratio ($ER = H/h$) of 2.1. The origin of the coordinate system and the directions of the streamwise (x), transverse (y) and spanwise (z) are shown in Fig 3. The air tunnel is made from Plexiglas sheets of 0.95 cm thick that are machined and assembled to form the desired geometry. The two sidewalls and the top wall of the test section are made of 0.6 cm thick optical glass. The use of the optical glass for these walls facilitates and improves the use of a 3-D Laser Doppler velocimeter (LDV) for measuring non-intrusively the three velocity components inside the test section. Three-dimensional traversing system is used with the fiber optics LDV system

to move the measuring probe to any desired location in the flow domain. The length of the exit section of the air tunnel downstream from the step is 1.0 m long and this length is sufficient to ensure that the air flow is fully developed at the exit plane of the tunnel. The air tunnel is supported by an aluminum frame and is placed in a vertical position for measurements.

2.2. Laser doppler velocimeter

A three-component LDV system is used to measure non-intrusively the instantaneous three velocity components at any desired point inside the flow domain. The basic components of this 3-D LDV system are an Argon-Ion laser, fiber drive with beam splitter, transmitting/receiving optics, photo detectors, signal processors and a data analysis system. The output from the Argon-Ion laser beam is split optically into two parallel beams with equal intensities and one of these beams is passed through a Bragg cell that is used to shift its frequency to a higher value. This optical path results in two parallel beams, one is shifted and the other is un-shifted. These two beams pass through prisms that are used to disperse each beam into its color spectrum. The Green (514.5 μm), Blue (488.0 μm) and the Violet (476.5 μm) color components from these beams are used in measuring the three velocity components u, v, and w, respectively. Each color pair from the shifted and un-shifted beams is guided by mirrors to produce a parallel pair of beams that passes through lenses to focus that pair into a fiber optics cable. Three separate fiber optics cables transmit the three different color beams to different transmitting optics. The transmitting optics expand the two shifted and un-shifted beams into two separated and parallel-coherent beams that are then focused by a lens to form the measuring probe volume. That probe volume that is formed by the intersection of the

shifted and un-shifted beams is moved to any desired point within the flow domain by a traversing system to measure the velocity component at the point. When the three pairs of colored beams are placed perpendicular to each other and focused at the same point, they form a probe volume that can be used to measure the three velocity components simultaneously at any point within the flow domain. When the two coherent beams (shifted and un-shifted) of a given color intersect at the probe volume, they form a moving grid pattern (an interference fringe pattern of alternating light and dark lines) and when the seeded air particle flow through that grid a frequency is generated that can be related directly to the magnitude of the velocity component that is perpendicular to that grid.

The concept of this measuring technique is based on the premise that the seeded particles in the air are flowing at the same velocity as the air, and that is why the proper seeding of the flow with small particles is essential for proper measurements. The LDV system that is used in this study operated in a back scattering mode, which means that the scattering frequency that is generated by the moving seed particle as it flows through the probe volume is detected by the same probes that are used to transmit the incident laser beams (backscattering direction). One of these probes handled both the Green and the blue color beams (four beams that include the shifted and the un-shifted beam from each color) that are utilized for measuring the streamwise velocity component (u) and the transverse velocity component (v), respectively. The second probe which is placed perpendicularly to the first probe handles the two violet color beams and they are used to measure the spanwise velocity component and this arrangement is shown in Fig. 4. The six beams are aligned to focus (intersect) at a common focal point (probe volume) that is

moved to any desired location for measuring the three velocity components simultaneously at the point. The back scattered light/frequency is captured by the transmission/receiving optics and focused on the photo detector producing a signal with a given frequency. Software is used to subtract the shifted frequency from the measured frequency thus generating the Doppler frequency f_D that is associated with the velocity. The velocity is calculated from the Doppler frequency and the fringe spacing that exists inside the probe volume. The fringe spacing that develops inside the control volume is determined from the frequency of the laser beams, the separation distance between the two beams and the focal length of the lens that is used to focus the two beams. The output from the three photo multiplier tubes are treated by three signal analyzers with appropriate software/hardware to generate the instantaneous and also the average velocity components from a large sample of data. During the measurement, the photo multiplier tube (PMT) voltage for each channel (*u, v & w*) is set to a value below the saturation level indicated by the LED on the signal analyzers. The sampling rates and low pass filters are adjusted to obtain good data rates and good signals for velocity measurements. Hardware coincidence is enabled in the LDV control system in the signal analyzer to obtain coincident measurements (i.e. measurements of *u, v* and *w* are made for the same particle that passes through the control volume). In that coincident mode of operation non-coincident signals are rejected from the sample set that is used to determine the instantaneous velocity component.

The two component probe that is used to measure *u* and *v* velocities has a transmitting lens with focal length of 250 mm. A single component probe measuring *w*-velocity has a transmitting lens with focal length of 100 mm. The two probes sits on the

traverse system and the measurement volume is moved to desired location inside the test section with an accuracy of 0.1 mm using three dimensional traverse mechanisms as shown in Fig. 4. The traverse system and real-time signal analyzers (RSA) are controlled by personal computer with Data-VIEW NT software. The traverse system is aligned with the air tunnel and made to move parallel to the system along all the axes.

2.3. Measurement procedures

The air flow rate (Q) through the tunnel is controlled by the control valve that is at the inlet of each flow meter and the desired value is set by the calibrated scale on each flow meter. The average velocity in the duct upstream from the backward-facing step (the developing length of the air tunnel) can be calculated from $u_0 = Q/A$ and the Reynolds number is calculated from its definition as $Re = \rho u_0 D_h/\mu$ where D_h is the hydraulic diameter of the upstream duct.

Velocity measurements in the fully developed flow regime inside the upstream duct from the backward step at three different spanwise locations were made to establish the appropriate number of LDV samples that are needed to accurately determine the average of each velocity component. Steady flow was established in the air tunnel and the maximum velocity inside the upstream duct in the fully developed regime was measured at 9.3 m/s. At that flow rate and at the measuring cross section, the flow is turbulent and fully developed with a Reynolds number of Re = 8631. From many repeated measurements in that fully developed turbulent flow regime, it was determined that 1000-5000 acceptable LDV samples are sufficient to accurately determine the local mean velocity components in the flow domain. A higher value will be needed in the separated flow region. From the repeatability of these measurements, it was determined

that the deviations of the mean velocities is within ± 0.025 m/s for the streamwise velocity component (u) and within ± 0.006 m/s for the transverse velocity component (v) and within ± 0.005 m/s for the spanwise velocity component (w) and that is equivalent to the uncertainty in these measurements.

Steady flow conditions were established for a given air flow rate by monitoring the average streamwise velocity component at x/S = -2 at the center of the upstream duct over a period of time. The repeatability of that measurement ensured that the flow is steady and measurements downstream from the step could be performed for that selected air flow rate

3. Results and discussions

The characteristics of the fully developed flow in the duct upstream of the step are measured and the results for laminar flow are presented in Fig. 5. As can be seen from that figure the inlet flow to the test section is symmetric relative to the center of the duct's width and the spanwise distribution of the streamwise velocity component is uniform in approximately 80% of the duct's width. Similarly, measured results in the upstream duct for turbulent flow (Re = 8631) are presented in Fig. 6 for the spanwise distributions of streamwise velocity component (u) and for the streamwise Reynolds stress component $\overline{u'^2}$ at the center of the upstream duct. These results also show that the turbulent flow is almost symmetric relative to the center of the duct's width. The upstream spanwise symmetry for both laminar and turbulent flow should result in spanwise symmetry also downstream from the backward-facing step. The measured transverse distributions of the inlet mean streamwise velocity component and the streamwise Reynolds stress component $\overline{u'^2}$ at the upstream duct at three different

spanwise locations, z/L = 1, z/L = 0.5 and z/L = 0.25 are presented in Fig. 7 for turbulent Reynolds number of 8631. The results show symmetry relative to the center of the duct's height and results at z/L = 1 and z/L = 0.5 show only minor difference, but noticeable difference appear in the results at z/L = 0.25 (decrease in the maximum velocity at the center of the duct and a decrease in the Reynolds stress near the sidewall. The Reynolds stress ($\overline{u'^2}$) is small at the center of the duct and increases gradually to a peak near the walls before starting to decrease again as the walls are approached. The transverse and the spanwise velocity components (v and w) are negligible at streamwise location of the upstream duct and for that reason they are not presented.

The mean streamwise velocity component in the separated and re-developing flow near the reattachment region adjacent to the stepped wall (y/S = 0.06) are measured to identify the location where that velocity component is equal to zero. That location identifies approximately the outer edge of the primary recirculation flow region that develops downstream from the backward-facing step. For a given z/L plane and y/S = 0.09, the mean streamwise velocity component is measured at different streamwise locations near the reattachment region. These measurements of negative and positive streamwise velocity component are used to locate, by interpolation, the location where the streamwise velocity component is equal to zero at that z/L location as shown in Fig. 8a. By performing such measurements at different z/L planes, the spanwise distribution of outer edge boundary of the primary recirculation flow region can be mapped for a given flow rate, and the line identifying this boundary is designated as the (x_u-line) for that flow rate. Results for (x_u-lines) for different Reynolds numbers are presented in Fig. 8b and 8c. These results show that the x_u-lines move further downstream (equivalent to a larger

recirculation flow region) as the Reynolds number increases in the laminar flow regime (Re < 600). The x_u-lines start moving gradually upstream as the Reynolds number increases in the transition flow region (600 < Re < 4000) and they become almost independent of the Reynolds number in the fully turbulent flow regime (Re > 4000). Significant and sudden decrease in the size of the recirculation flow region occurs at the end of the transition region or at $Re \approx 3500$. The spanwise distribution of the x_u-lines is symmetric in the laminar flow regime and exhibits a minimum near the sidewall and a maximum at the side wall with a local peak at the center of the duct's width. The x_u-lines in the transition regime have greater uncertainty and are more difficult to measure due to higher fluctuation and turbulence in the velocity and some un-symmetry might develop in these lines. The peaks and the valleys disappear from the spanwise distribution of the x_u-lines in the fully turbulent flow regime and these lines become flat (constant value) through most of the duct width.

The transverse distributions of mean streamwise u-velocity component inside the recirculation flow region at $x/S = 2.83$ and at the center of the duct ($z/L = 1$) are presented in Fig. 9 for different Reynolds numbers. The maximum magnitude in both the positive and negative directions increases with increasing Reynolds number. The significant changes in the distributions between the case for Re = 3483 and 4056 reflects the end of the transition regime and the beginning of the fully turbulent flow regime in this geometry. The transverse distributions of the mean streamwise velocity component in the fully turbulent flow regime at Re = 8631 are presented in Fig. 10 for different spanwise (z/L = 1, z/L = 0.5 and z/L = 0.25) and streamwise (x/S = 2.83, x/S = 6.604 and x/S = 10.377) locations. The three streamwise locations represent one inside the primary

recirculation region, one at the outer edge of that region and one in the re-developing flow region. For this Reynolds number the reattachment length is at x/S = 6.844 and appears to be constant in most of the spanwise direction. The maximum mean streamwise velocity component in both the positive and negative directions decrease as the distance from the backward-facing step increases due to increase in the cross sectional area. The velocity distributions are similar for different spanwise locations but the magnitude of the maximum velocity decreases as the distance to the sidewall decreases. A comparison between velocity distributions at one streamwise location inside the recirculation region (x/S = 2.83) at three different spanwise location show little difference between each other. The behavior is true for other streamwise locations and for that reason such results are not presented.

Transverse distributions of the mean transverse v-velocity component are presented in Fig. 11 for three streamwise (x/S = 2.83, x/S = 6.604 and x/S = 10.377) and three spanwise (z/L = 1, z/L = 0.5 and z/L = 0.25) planes. The development of a relatively strong positive (away from the stepped wall) flow is evident at x/S = 2.83 inside the recirculation flow region and a relatively strong negative (toward the stepped wall) flow is evident at x/S = 6.604 near the reattachment line in these results. It should be noted that the magnitude of that upward flow and the downward flow are higher at a spanwise location of z/L = 0.25 than the other two spanwise locations. The strong downward flow at z/L = 0.25 results from the "jet-like" flow that develops in the separating shear layer near the sidewall in this geometry [11]. The geometry of the test section and the focal length of the transceiver lens of the LDV system made the measurements near the stepped wall (y/S = 0) and near the upper flat wall (y/S = 1.91) impossible because the

optical beams become blocked by the walls of the test section. A comparison between *v*-velocity distributions at one streamwise location inside the recirculation region (*x/S* = 2.83) at three different spanwise location is also presented in this figure and the results show a similar general behavior and illustrate more clearly the higher upward flow and higher downward flow that develops near the sidewall at *z/L* = 0.25. Similar measurements were performed for the mean spanwise *w*-velocity component and those results are presented in Fig. 12. These measurements show a greater degree of scattering and possibly uncertainty in these results but the trend clearly shows a strong variation of that velocity component in the transverse, spanwise and streamwise directions. The transverse distribution shows that near the walls (top and bottom walls) that velocity component increases rapidly to a peak value, and then starts to decrease at approximately one third of a step height away from these walls and in some cases becoming negative at the center height of the duct. A larger variation in its magnitude is seen at a streamwise location inside the recirculation region (*x/S* = 2.83) than near the reattachment region (*x/S* = 6.604). The spanwise variation of that velocity component shows that near the side wall (*z/L* = 0.25) the magnitude is significantly greater near the stepped wall (*y/S* = 0) than near the flat wall (*y/S* = 1.91).

The normal Reynolds stress and the Reynolds shear stress were deduced from the instantaneous measurements of the velocity components and these results are presented in Figs. 13 – 16. The transverse distribution of the normal Reynolds stress component in the *x*-direction ($\overline{u'^2}$) is shown in Fig. 13 for spanwise locations of *z/L* = 1.0, 0.5 and 0.25 and for streamwise locations of *x/S* = 2.83, 6.604 and 10.377. These results show this component increases gradually as the distance from the stepped wall (*y/S* = 0) increases

developing a peak near the edge of the shear layer at approximately $y/S = 1$. That trend is followed by a decrease to a minimum value at approximately $y/S = 1.5$ and that is followed by the development of another peak in that distribution before decreasing to zero at the upper flat wall ($y/S = 1.91$). The behavior for $y/S > 1$ is similar to the one shown in Fig. 7 for fully developed duct flow. It magnitude decreases as the streamwise distance from the step increases. Its magnitude does not depend significantly on the spanwise coordinates (within the measured range) as shown in the figure for $x/S = 2.83$.

The transverse distribution of the normal Reynolds stress component in the y-direction ($\overline{v'^2}$) is presented in Fig. 14 at the same spanwise and streamwise locations that were shown in the previous figure. The magnitude of that component is a maximum near the edge of the developing shear layer and as a result the location of that maximum becomes closer to the stepped wall as the streamwise distance from the step increases. Similarly the magnitude of that maximum decreases as the distance from the step increases. Steep rise in its magnitude develops near the stepped wall while it is increasing toward its peak value, but the rate of increase near the flat wall is significantly smaller. The distribution is not significantly sensitive to the changes in the spanwise coordinates, but slightly smaller maximum develops near the sidewall. Similar results are presented for the transverse distribution of the normal Reynolds stress component in the z-direction ($\overline{w'^2}$) in Fig. 15. The distribution of this component is similar to the one discussed for the ($\overline{v'^2}$). A local small peak develops near the flat wall and that is followed by a local minimum as the distance from the flat wall increases. The sensitivity of that component to the streamwise location is negligible (within the measured range).

Similar results are presented for the Reynolds shear stress ($\overline{u'v'}$) and for the turbulent kinetic energy ($k = \frac{1}{2}\left(\overline{u'^2} + \overline{v'^2} + \overline{w'^2}\right)$) in Figs. 16 and 17. Measurements very close to the stepped and the flat walls could not be made because the walls of the test section interfere with some of the LDV beams (*v*-velocity component) as discussed earlier. The transverse distribution of the Reynolds shear stress $\overline{u'v'}$ that is presented in Fig. 16 does not show the regions close to the walls, but it shows that its magnitude decreases as the distance from the stepped and the flat wall increases and that minimum absolute value occurs at approximately the location where the mean streamwise velocity is zero (a line passing through the middle of the recirculation flow region). Its absolute magnitude decreases as the distance from the step increases. The variation of other Reynolds shear stresses $\overline{u'w'}$ and $\overline{v'w'}$ are not presented here because their magnitudes are much smaller (close to zero) and the resulting relative errors in their evaluation is significant. The trends for the turbulent kinetic energy that are shown in Fig. 17 are similar to the normal Reynolds stress component in the *x*-direction ($\overline{u'^2}$) because it is the dominant component in the turbulent kinetic energy calculations. Its magnitude does not appear to be sensitive to the spanwise coordinate inside the recirculation region for the results presented in this study.

4. Numerical simulation

An effort is made to simulate the measured results in the fully turbulent flow regime in this geometry for Reynolds number *Re* = 8631 using some of the existing turbulence models in the FLUENT CFD code. The schematic of the test section is shown in Fig. 3 and its dimensions have been presented earlier. The length of the computational domain is chosen as 50 times the step height (0.53 m) downstream from the step and two

times the step height (0.0212 m) upstream of the step respectively, i.e. $-2 \leq x/S \leq 50$. The width of the computational domain is chosen as half of the actual width of the duct ($L = W/2$ =0.0396 m) due to the spanwise symmetry of the velocity field. The three dimensional time averaged steady Navier-Stokes and continuity equations for turbulent incompressible flow are solved using the finite volume method. The turbulence in the flow is modeled using Reynolds stress model (RSM) with linear pressure strain model, AKN low Reynolds number turbulence model and the SST k-ω turbulence model and these three models predicted different reattachment lengths at the center of the duct. The Reynolds stress model (RSM) was also selected for this simulation because it is the only one that generates directly the normal and the shear Reynolds stresses for comparison with the measurements. The low Reynolds number model results in a reattachment length at the center of the duct $x_u/S = 6.234$; the results from the k-ω turbulence model is $x_u/S = 9.296$; and the results from the RSM turbulence model is $x_u/S = 5.213$. This difference in predicting the reattachment length at the center of the duct amplifies the need for turbulence model improvements and the measurements needed to guide and validate such improvements. The physical properties of air is treated as constants and evaluated at the inlet air temperature of $T_0 = 20^{\circ}$C. Inlet flow ($x/S = -2$, $1 \leq y/S \leq 1.91$, for all z) is considered to be isothermal ($T_0 = 20^{\circ}$C), hydrodynamically steady and fully developed. The fully developed turbulent inlet air flow distributions (streamwise velocity component (u), transverse velocity component (v), spanwise velocity component (w), turbulent kinetic energy (k), dissipation rate (ε), specific dissipation rate (ω), the normal and the shear Reynolds stresses are generated by using a separate simulation of air flow using three turbulence models in a duct having the same height and width as the upstream duct

that is used in the experiment. The length of the duct that was used to generate the fully developed velocity profile at the inlet to the test section is 150 times the step height with the inlet condition chosen as uniform streamwise velocity for Re = 8631 (based on D_h) and 5% turbulence intensity. The no-slip boundary condition is applied to all of the solid wall boundaries, and fully developed flow condition is imposed at the exit section of the computational domain.

Numerical simulation of the time averaged governing equations and boundary conditions were performed using the commercially available CFD code Fluent 6.3.26. The mesh is generated using FLUENT's pre-processor GAMBIT 2.4.6 and hexahedron volume elements are used in the simulation. At the end of each iteration, the residual sum for each of the conserved variables is computed and stored, thus recording the convergence history. The convergence criterion required that the scaled residuals be smaller than 10^{-10} for the mass, momentum, turbulent k-ε equations and Reynolds stresses. Calculations are performed on NIC-cluster's parallel computation facility with 8 processors and the CPU time for converged solution for Re = 8631 is approximately 16 hours for Reynolds stress model, 11 hours for SST k-ω model and 3-1/2 hours for AKN low-Re k-ε model. The SIMPLEC algorithm is used for the pressure velocity coupling. The momentum, turbulent kinetic energy, turbulent dissipation rate, specific dissipation rate and Reynolds stress equations are discretized with the second order upwind scheme in order to improve the accuracy of the simulations. Detailed descriptions of the CFD code, Reynolds stress turbulence model and the solution procedures may be found in the FLUENT manual.

The computational grid is generated using boundary layer meshes to ensure high density near the bounding walls and in the regions of the sudden expansion where high gradients exist in order to improve the accuracy of the simulations. Grid independence tests were performed using different grid densities and distributions for Re = 8631 for Reynolds stress model and the results for reattachment length at z/L = 1 and y/S = 0 is shown in Table 1. Comparison of grid 2 and grid 3 shows less than 1% difference for reattachment length. Therefore grid 2 (170 x 84 x 50) is used downstream of the sudden expansion and a grid of 30 x 40 x 50 is used upstream of the sudden expansion for all the simulation results that are presented in this paper.

Table 1 Reattachment length at z/L = 1 and y/S = 0 for different computational grids

Grid	x x y x z Grid size (downstream)	x_u/S at z/L = 1 and y/S = 0
1	150 x 64 x 40	5.1221
2	170 x 84 x 50	5.2130
3	190 x 104 x 60	5.2594

5. Comparison with measured results

Simulated and measured results for the fully developed streamwise velocity component and the normal Reynolds stress component in the x-direction are compared in the upstream duct at (x/S = -1.89) in Fig. 18. These results are used as the inlet condition for simulating the separated flow downstream from the backward-facing step. The velocity distribution near the center of the duct compares very well with measurements for k-ω model for all the spanwise locations but some difference appears for the velocity near the side wall (z/L = 0.25) for Reynolds stress model. The normal Reynolds stress component in x-direction show similar trends as the measured values with a peak

developing near the walls but some difference develop near the center height of the duct. The normal Reynolds stress results show that they are almost not sensitive to changes in the spanwise location for the range presented in this figure.

Simulated results for the spanwise distribution of the x_u-line downstream from the step are compared with measurements in Fig. 19. The Reynolds stress model (RSM) and AKN low Reynolds number model under predicts the reattachment length at the center of the duct (z/L = 1) by 24% and 8.9% and k-ω model over predicts the reattachment length by 26%. The simulated increase in the x_u-line near the side wall could not be verified due to the low quality of the LDV signal in that region of the flow. Measurements indicate that the x_u-line is approximately constant through most of the duct width.

The simulated transverse distributions of the mean velocity components *u, v* and *w* are compared with measurements in Fig. 20 at spanwise location of z/L = 0.5. Due to the difference in the simulated and measured reattachment length, these results are compared at the same ratio of x/x_R where x_R is the reattachment length at the center of the duct (simulated value of x_R differs from measured value). Relatively strong spanwise flow develops inside and outside the recirculation region in the flow. Reasonable comparison between measured and simulated results appears to exist outside the recirculation flow region but poor comparisons inside that region. The Reynolds stress model seems to predict the measured mean transverse and spanwise velocities more accurately than the k-ω model.

Simulated results for the normal Reynolds stresses components $\overline{u'^2}$, $\overline{v'^2}$ *and* $\overline{w'^2}$ from the Reynolds stress model (RSM) are compared with measurements in Fig. 21 at spanwise location of z/L = 0.5. The trends are similar but the difference is significant

where the simulations are higher than measurements. The difference is high near the stepped wall and in the center height region of the duct (Maximum difference of 44%), but becomes smaller near the flat wall. The difference between the two results could also be attributed to the quality of the turbulence model which predicts significantly lower reattachment length than the measured value. Similar results are presented for the Reynolds shear stress component $\overline{u'v'}$ in Fig. 22 using RSM and for the turbulent kinetic energy (*k)* in Fig 23 using both RSM and *k-ω* model. Here again the simulated trends are similar to the trends in the measured values but significant difference appears in the center height of the duct where the simulated results using RSM are higher than the measured values. The difference could be attributed to problems in the turbulence model that is used in the simulation. The turbulence kinetic energy prediction from the *k-ω* model is better than the Reynolds stress model.

6. Conclusions

Flow measurements in three-dimensional separated flow adjacent to backward-facing step using three components laser Doppler velocimeter are reported. The spanwise distributions of the reattachment line are presented for different Reynolds numbers covering the laminar, transition and turbulent flow regimes These results show that the size of the recirculation flow region increases rapidly as the Reynolds number increases in the laminar flow regime ($Re < 600$), decreases gradually as the Reynolds number increases in the transition flow region ($600 < Re < 3500$) and decreases suddenly and becomes almost independent of the Reynolds number in the fully turbulent flow regime (Re > 4000). The spanwise distribution of the reattachment line in the laminar flow regime exhibits a minimum near the sidewall and a maximum at the side wall with a

local peak at the center of the duct's width, but in the fully turbulent flow regime these lines become flat (constant value) through most of the duct width. Measurements of the three mean velocity components, normal Reynolds stresses components, Reynolds shear stress component and turbulent kinetic energy are presented for Reynolds number of Re = 8631 at different planes downstream from the backward-facing step. The results reveal that strong spanwise and transverse flow develops reflecting the three-dimensional flow that develops it. The results of simulating the experimental turbulent flow by using three different turbulence models differed significantly from each other. They simulate reasonably well the mean velocity components but fail to simulate the measured reattachment length or the turbulent quantities (normal and shear Reynolds stress components). This highlight the needs to improving these turbulence models for better predictions of drag and heat transfer in three-dimensional separated flow in complex geometries. The reported measurements can be utilized as a benchmark in developing improvements to these turbulence models.

Acknowledgement

This work has been supported in part by a DOE-Basic Energy Sciences grant No. DE-FG02-03ER46067, and by an NSF grant No. CTS-0352135.

References

[1] B.F. Blackwell, D.W. Pepper (Eds.), Benchmark problems for heat transfer codes, HTD-vol. 222, American Society of Mechanical Engineers, New York, NY, 1992.

[2] B.F. Blackwell, B.F. Armaly (Eds.), Computational aspects of heat transfer-Benchmark problems, HTD-vol. 258, American Society of Mechanical Engineers, New York, NY, 1993.

[3] B.F. Armaly, F. Durst, J.C.F. Pereira, B. Schonung, Experimental and theoretical investigation of backward-facing step flow, J. of Fluid Mech. 127 (1983) 473-496.

[4] J.K. Eaton, J.P. Johnson, A review of research on subsonic turbulent flow reattachment, AIAA J. 19 (9) (1981) 1093-1100.

[5] S. Jovic, D.M. Driver, Backward-facing step measurements at low Reynolds number, Re_h=5000, NASA Technical Memorandum 108807, National Aeronautics and Space Administration, 1994.

[6] H. Iwai, K. Nakabe, K. Suzuki, Flow and heat transfer characteristics of backward-facing step laminar flow in a rectangular duct, Int. J. Heat Mass Transfer 43 (3) (2000) 457-471.

[7] C. Shih, C.M. Ho, Three-dimensional recirculation flow in a backward facing step, ASME J. Fluids Eng. 116 (2) (1994) 228-232.

[8] K.S. Lim, S.O. Park, H.S. Shim, A low aspect ratio backward-facing step flow, Exp. Thermal Fluid Sci. 3 (5) (1990) 508-514.

[9] G. Papadopoulus, M.V. Ottugen, Separating and reattaching flow structure in a suddenly expanding rectangular duct, ASME J. Fluids Eng. 117 (1) (1995) 17-23.

[10] B.F Armaly, A. Li, J.H. Nie, Measurements in three-dimensional laminar separated flow, Int. J. Heat Mass Transfer 46 (19) (2003) 3573-3582.

[11] J. H. Nie, B. F. Armaly, Reattachment of three-dimensional flow adjacent to backward-facing step, ASME J. Heat Transfer 125 (3) (2003) 422-428.

[12] J. H. Nie, B. F. Armaly, Reverse flow regions in three-dimensional backward-facing step flow, Int. J. Heat Mass Transfer, 47 (2004) 4713-4720.

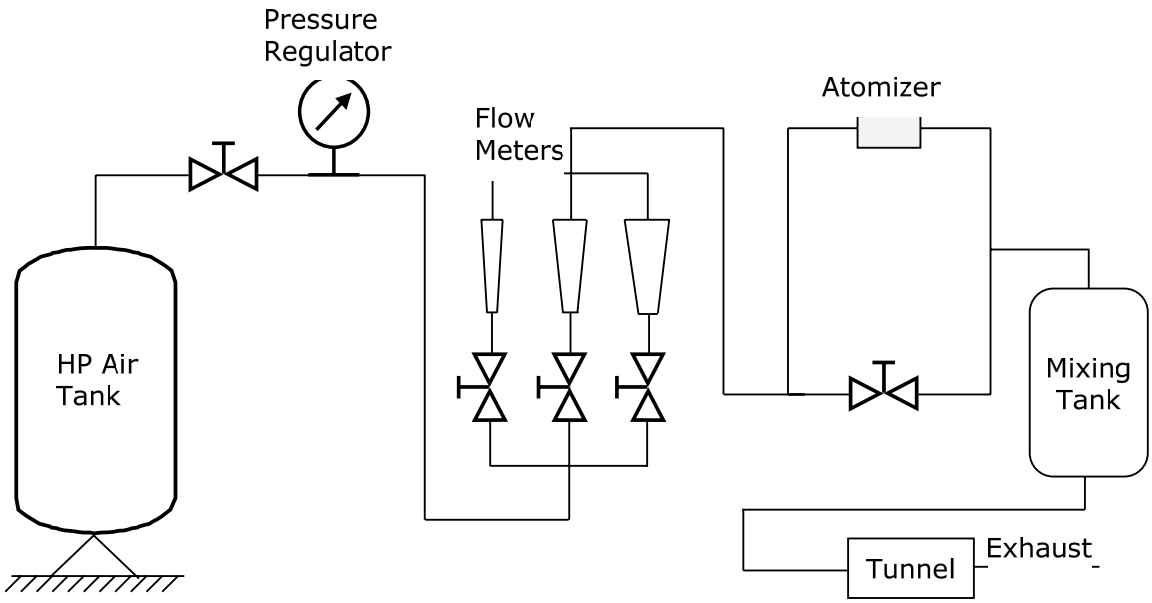

Fig. 1 Schematic of the air flow path to the wind tunnel

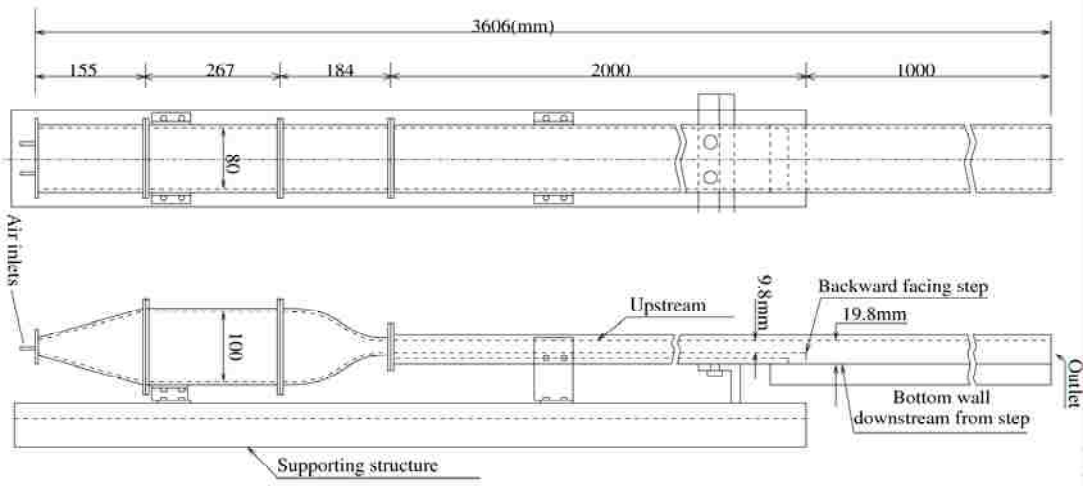

Fig. 2 Schematic of the air tunnel

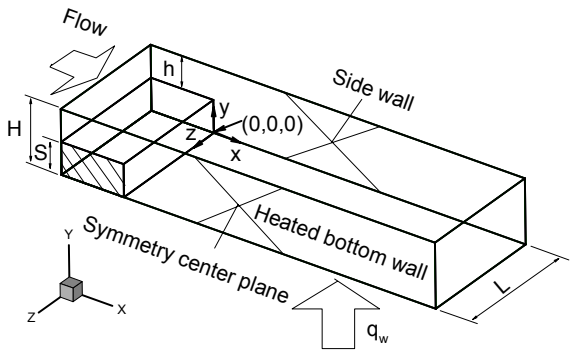

Fig. 3 Schematic of the backward facing step (test section)

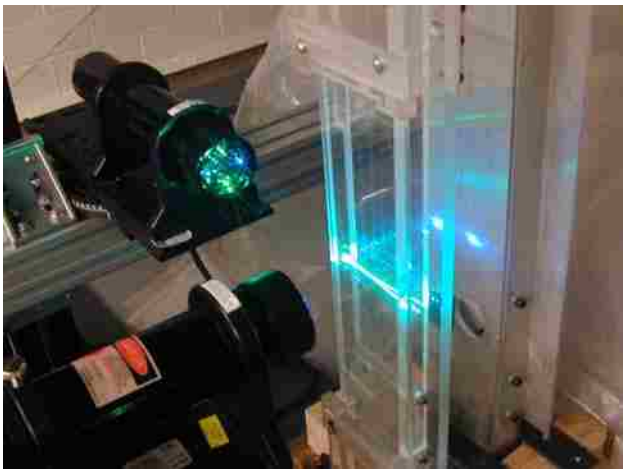

Fig. 4 Transmitting and receiving optics of the 3-D LDV system and the air tunnel

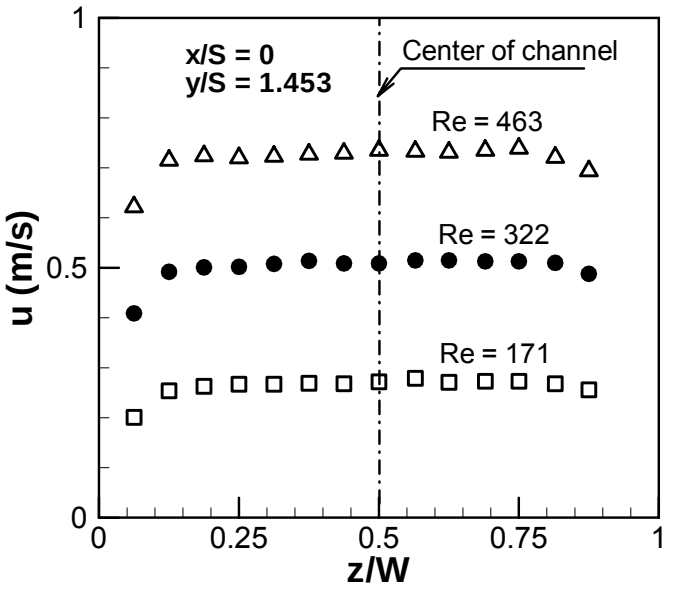

(*a*) Along the spanwise direction at y/S =1.453

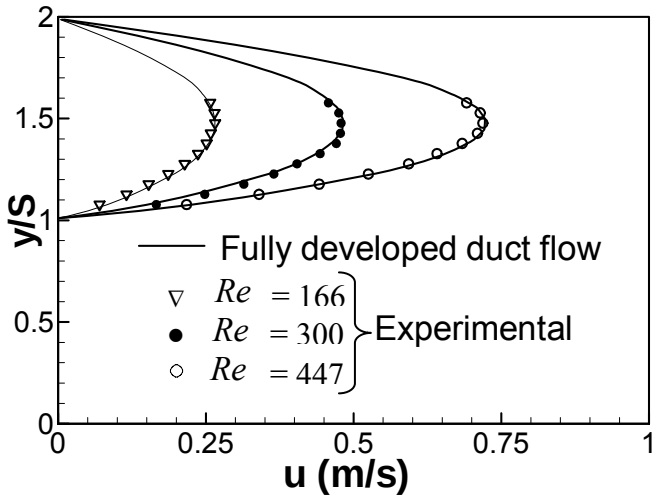

(*b*) Along the transverse direction at z/W = 0.5

Fig. 5 Distributions of streamwise *u*-velocity component at the step

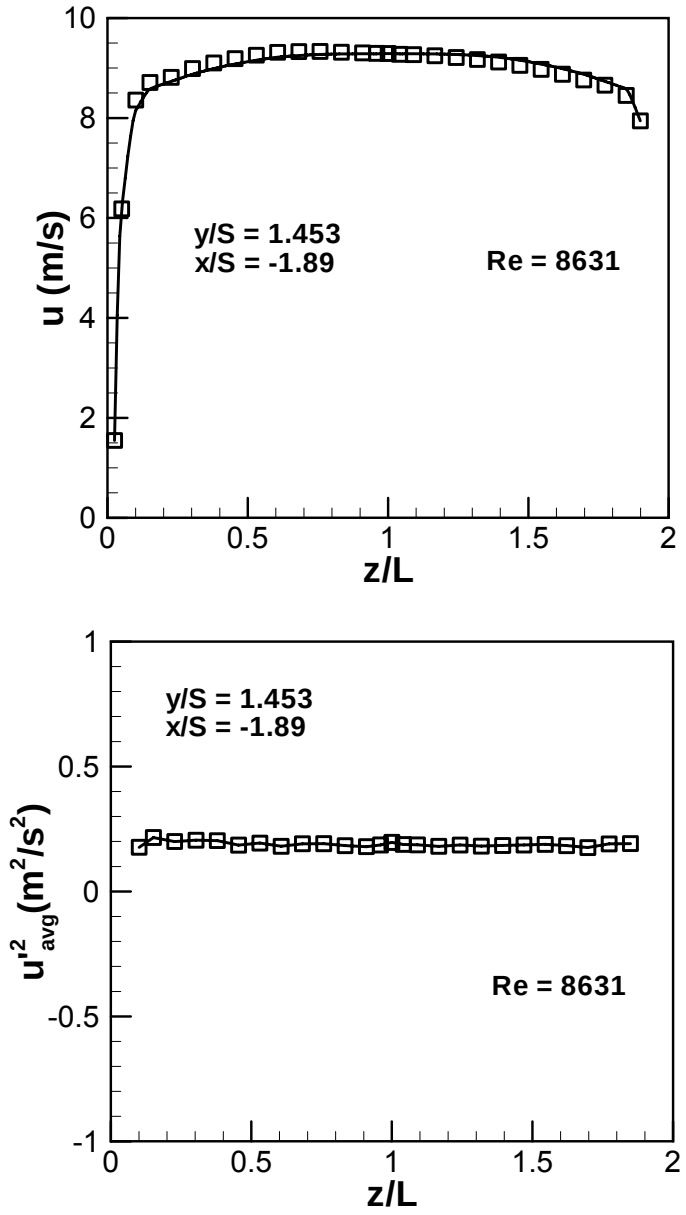

Fig. 6 Spanwise distributions of mean streamwise velocity component and streamwise Reynolds stress upstream of the step

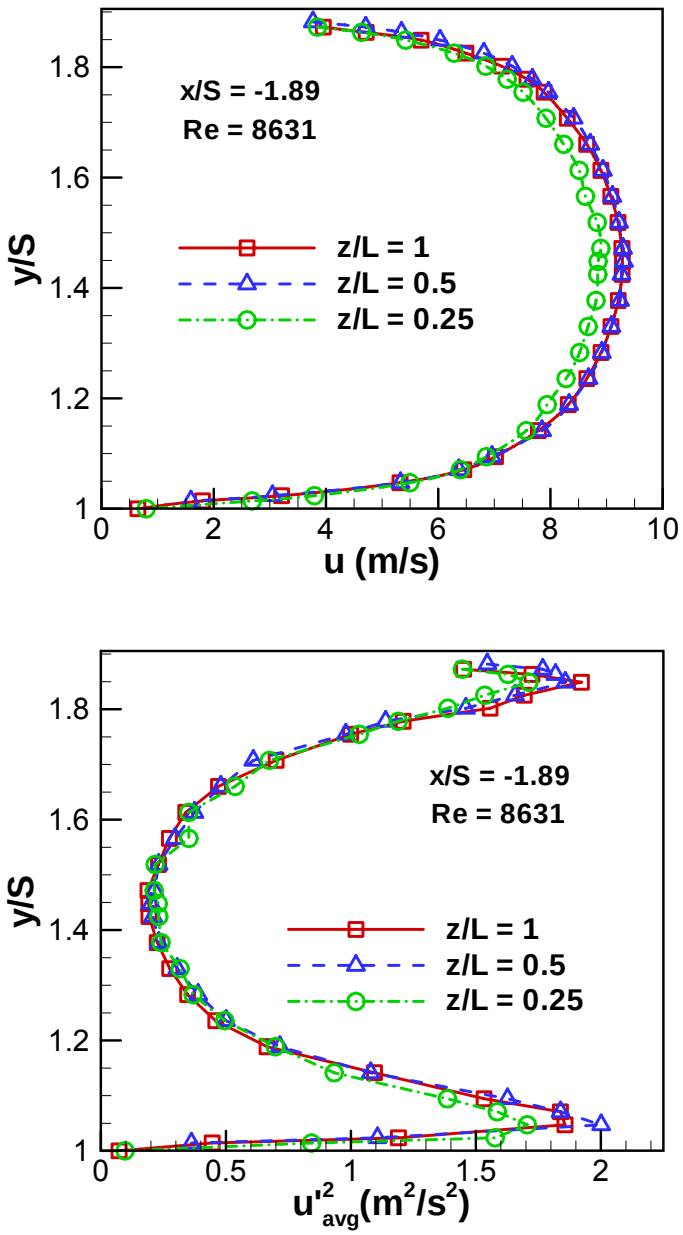

Fig. 7 Transverse distributions of mean streamwise inlet velocity profile and streamwise Reynolds stress ($\overline{u'^2}$) upstream of the step for different spanwise locations

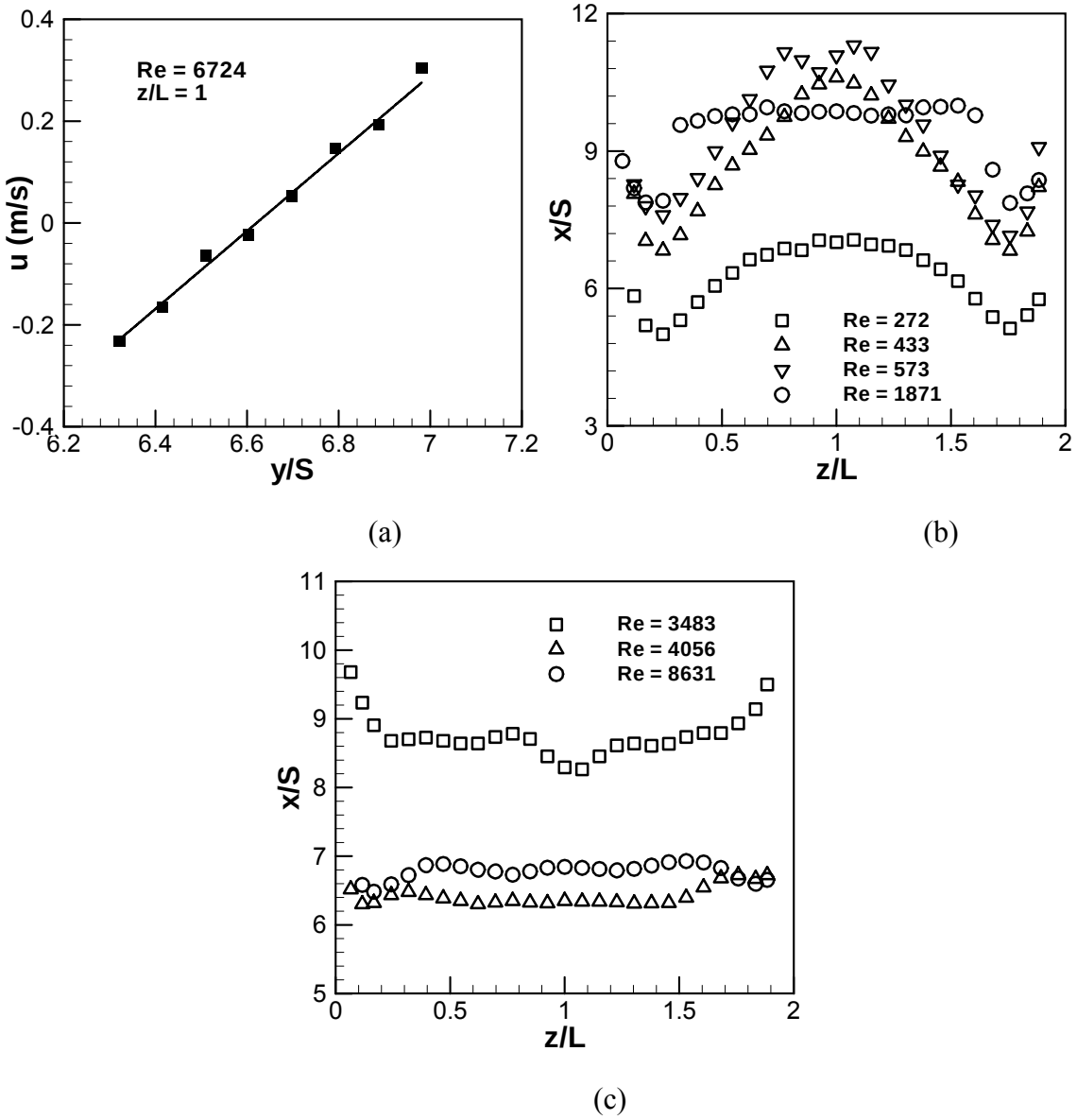

Fig. 8 Spanwise distributions of x_u-lines adjacent to the stepped walls for different Reynolds numbers

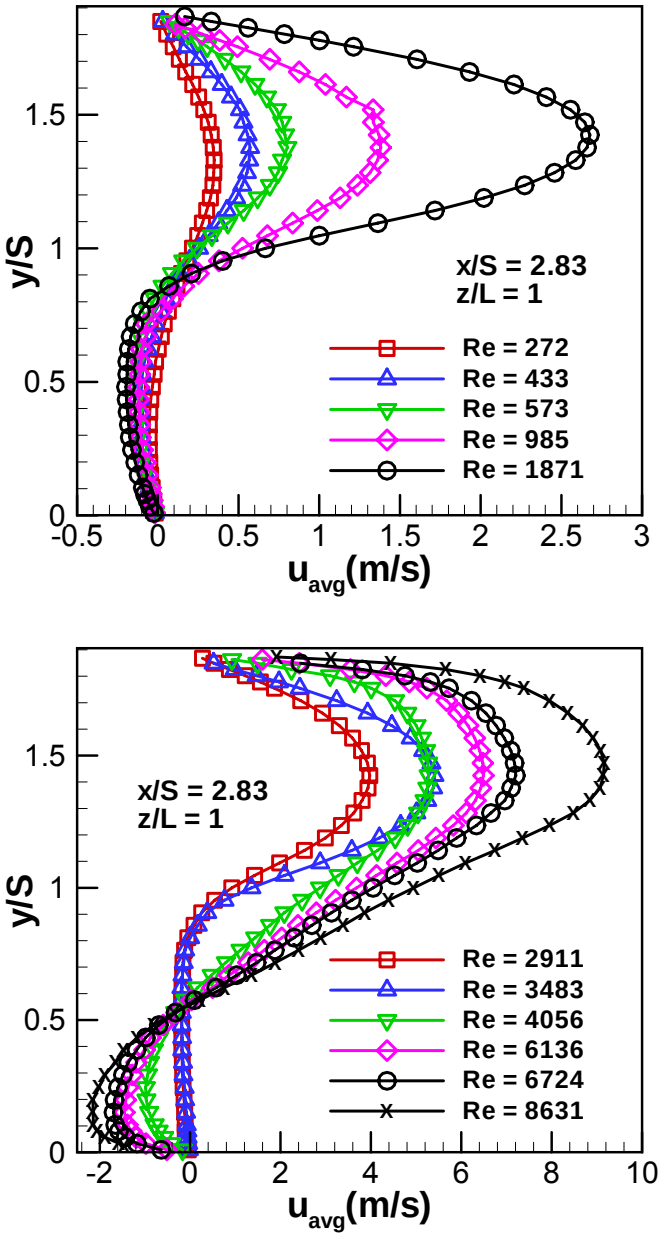

Fig. 9 Transverse distributions of mean streamwise *u*-velocity component for different Reynolds numbers

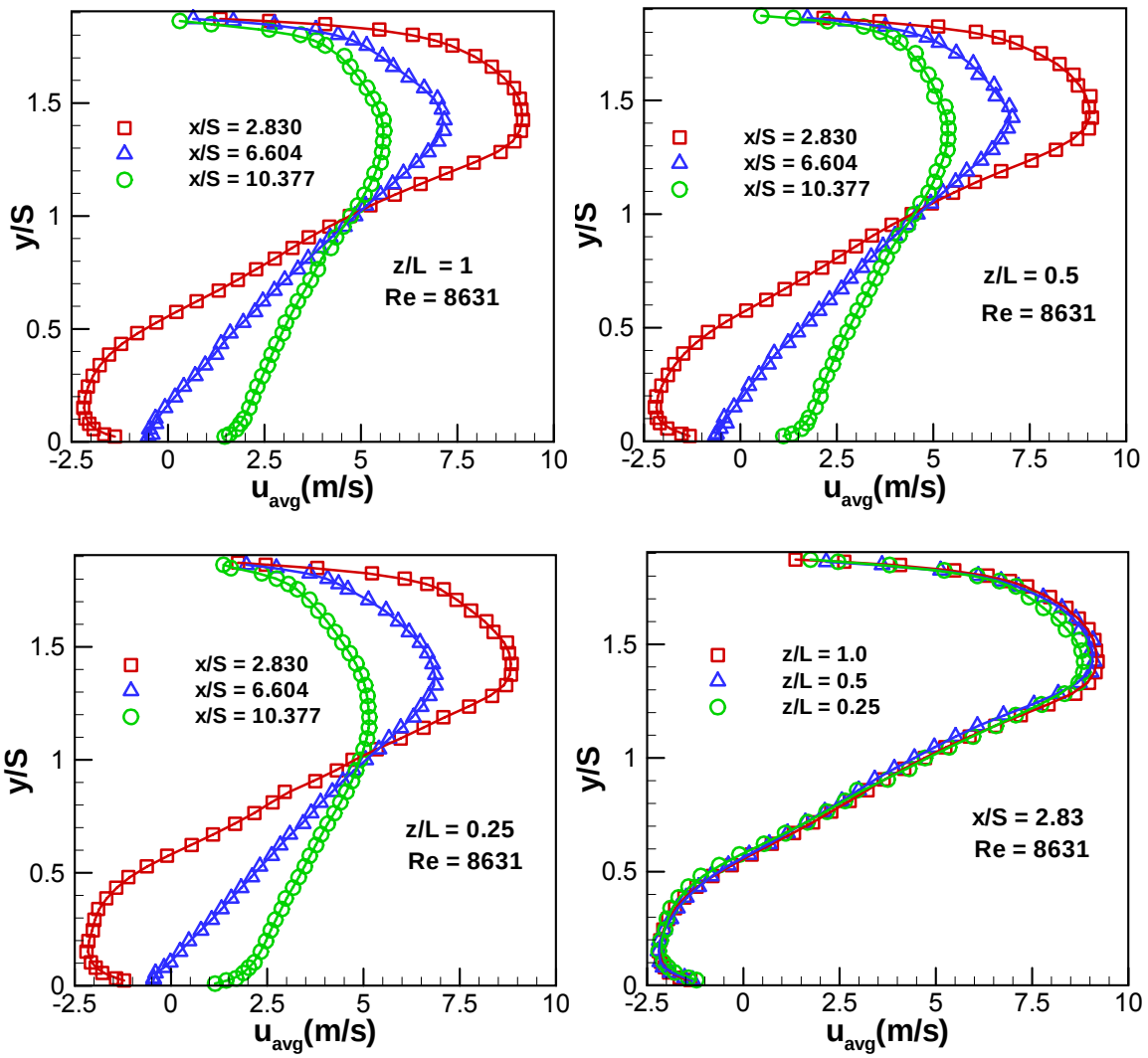

Fig. 10 Transverse distribution of the mean streamwise *u*-velocity component

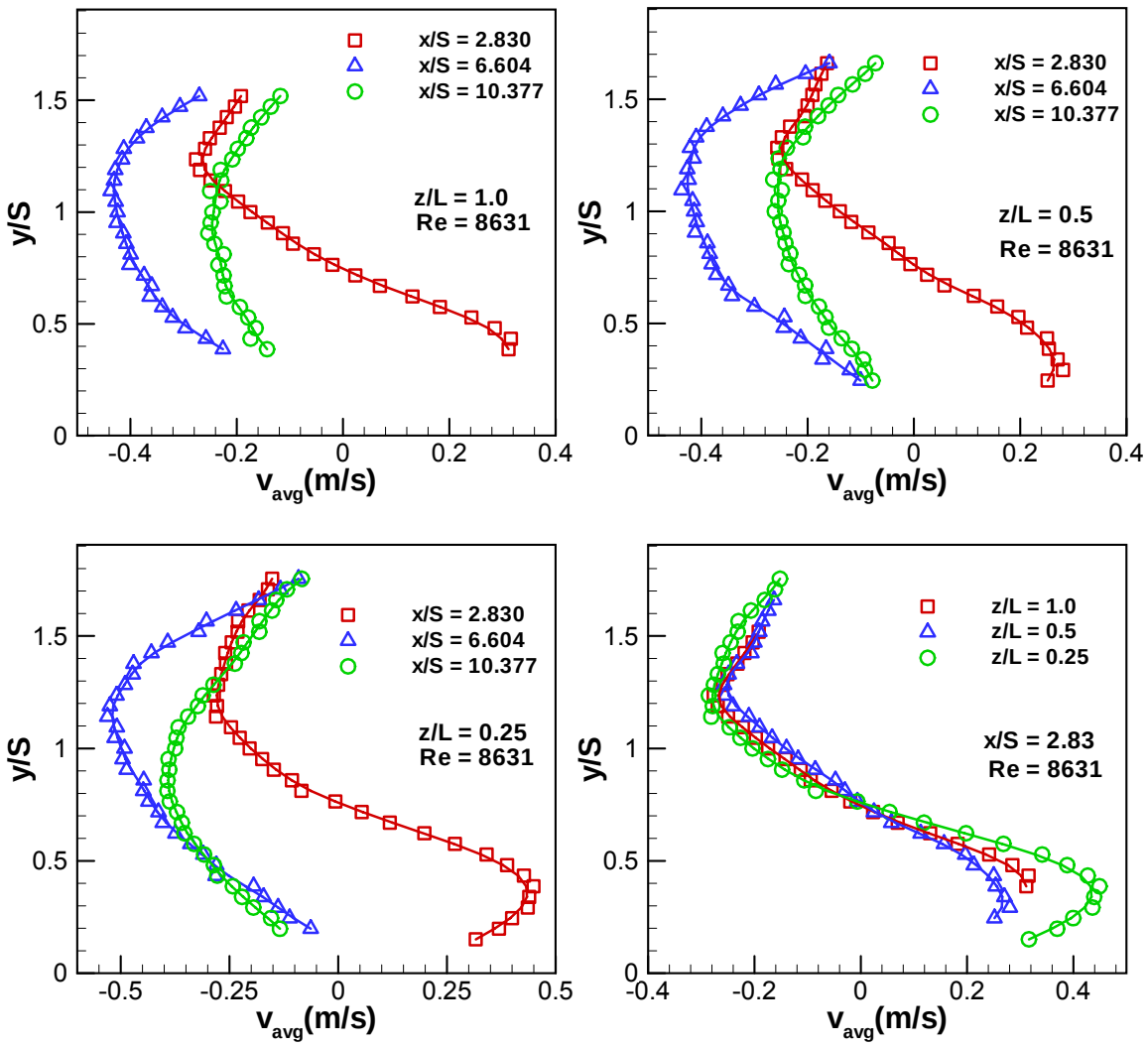

Fig. 11 Transverse distribution of the mean transverse *v*-velocity component

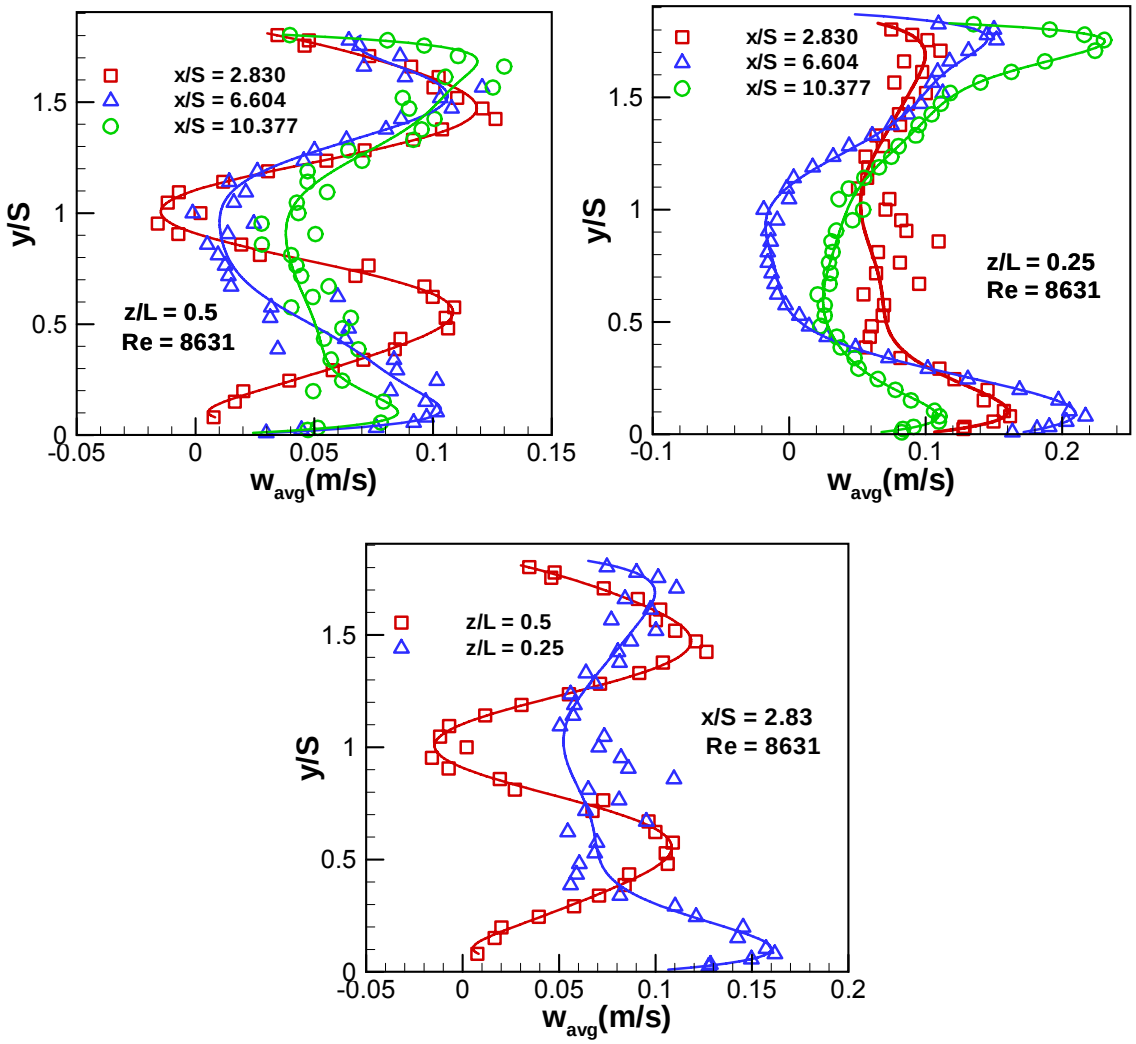

Fig. 12 Transverse distribution of the mean spanwise *w*-velocity component

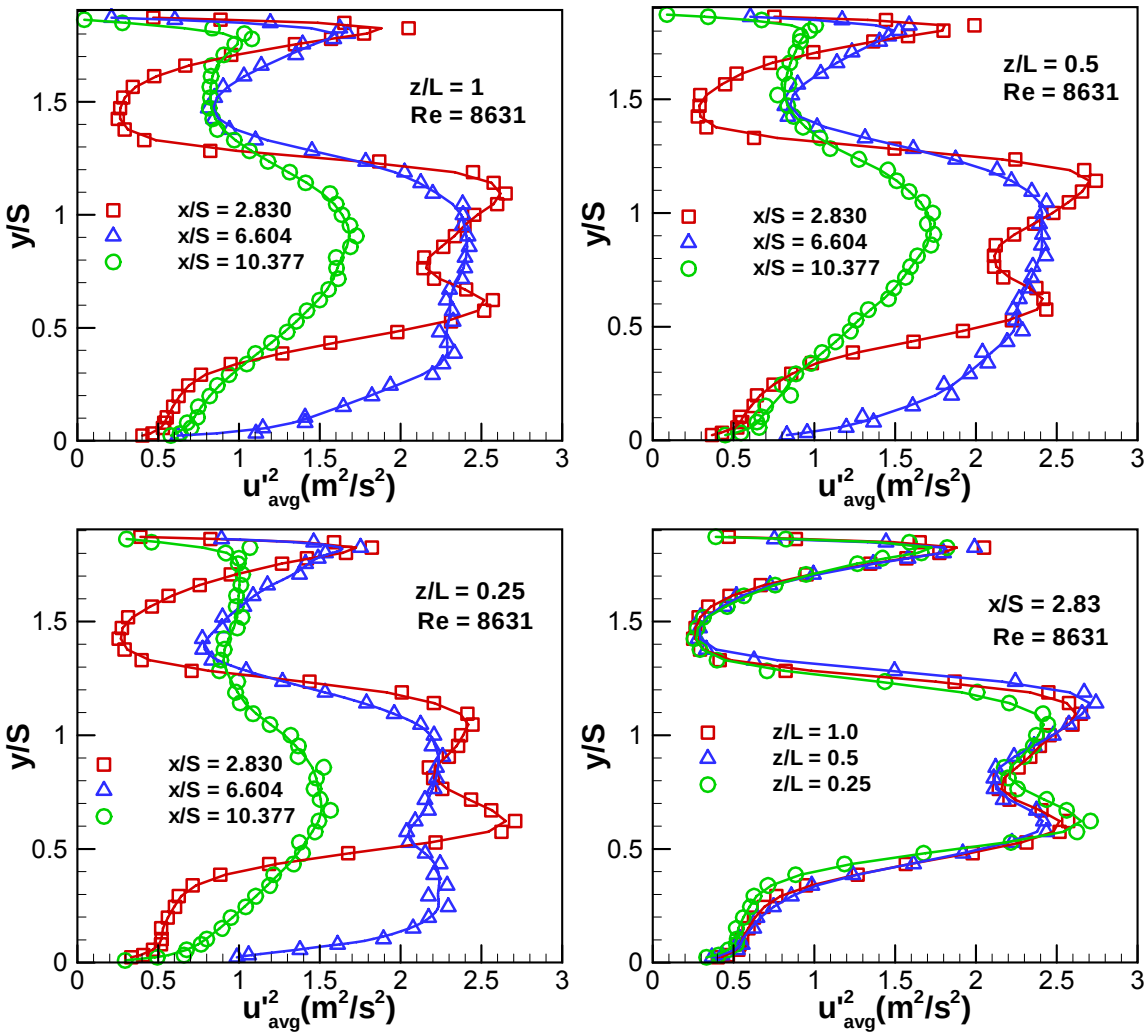

Fig. 13 Transverse distribution of the streamwise component of the normal Reynolds stresses ($\overline{u'^2}$)

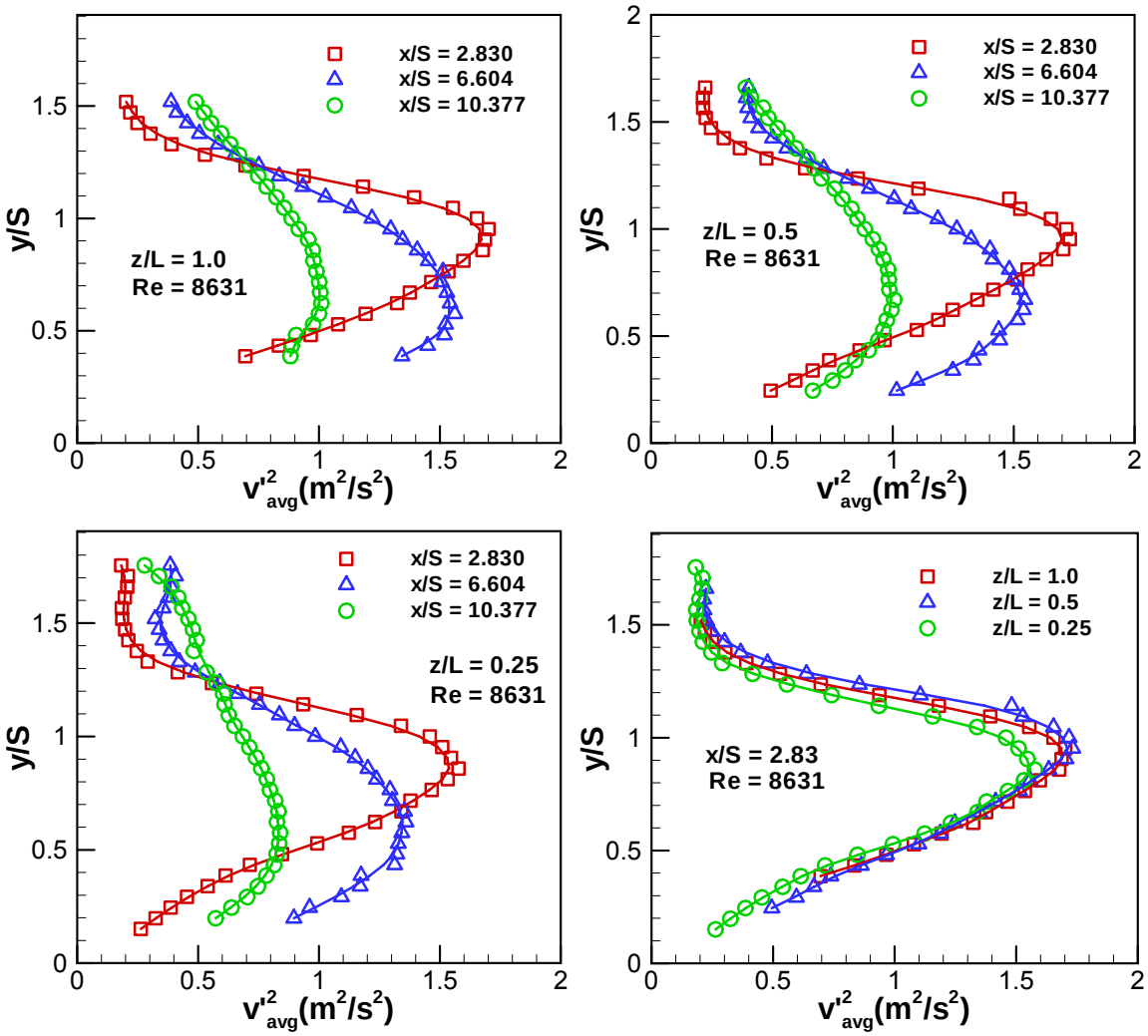

Fig. 14 Transverse distribution of the transverse component of the normal Reynolds stresses ($\overline{v'^2}$)

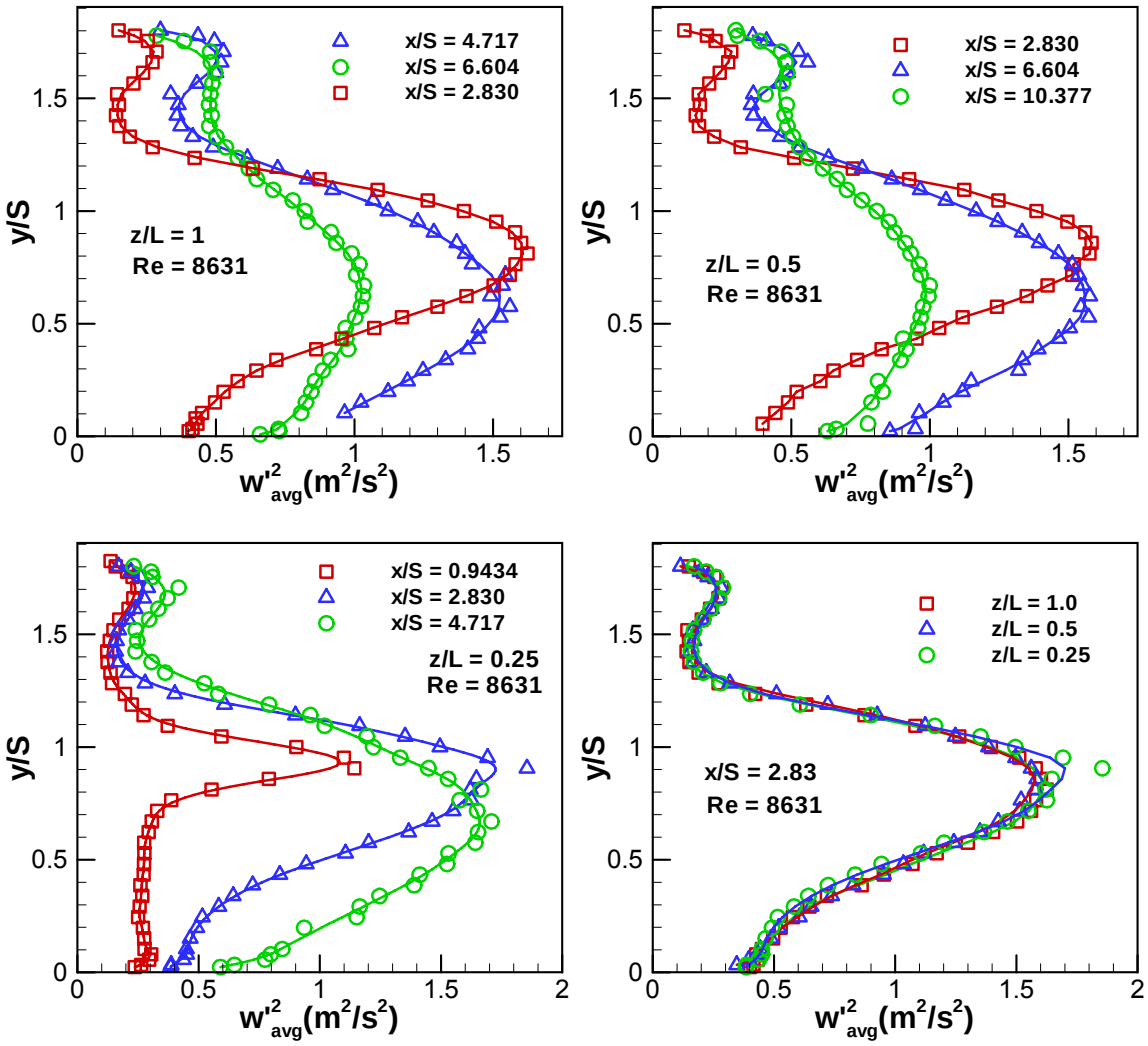

Fig. 15 Transverse distribution of the spanwise component of the normal Reynolds stresses ($\overline{w'^2}$)

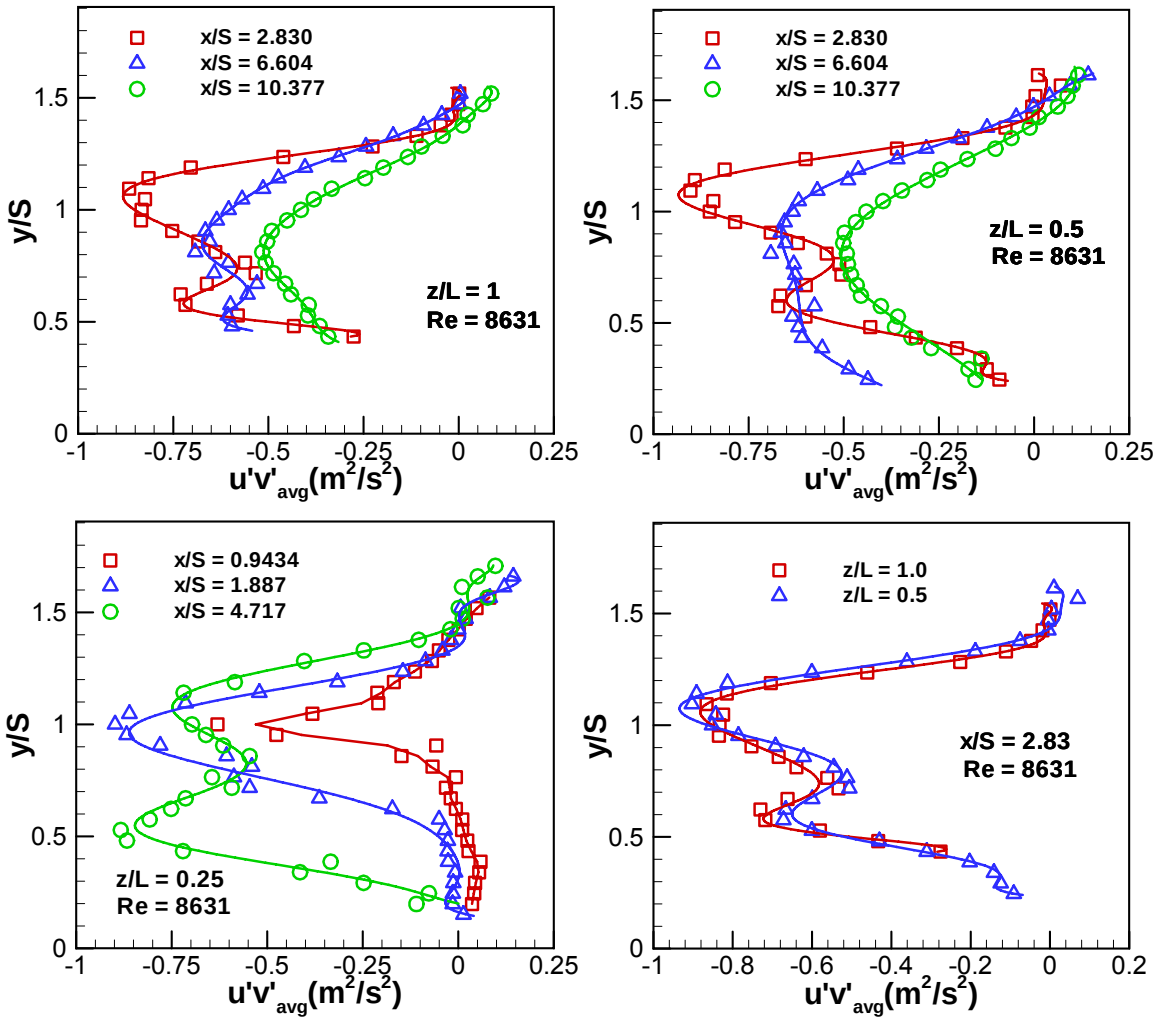

Fig. 16 Transverse distribution of the Reynolds shear stress ($\overline{u'v'}$) at different spanwise locations

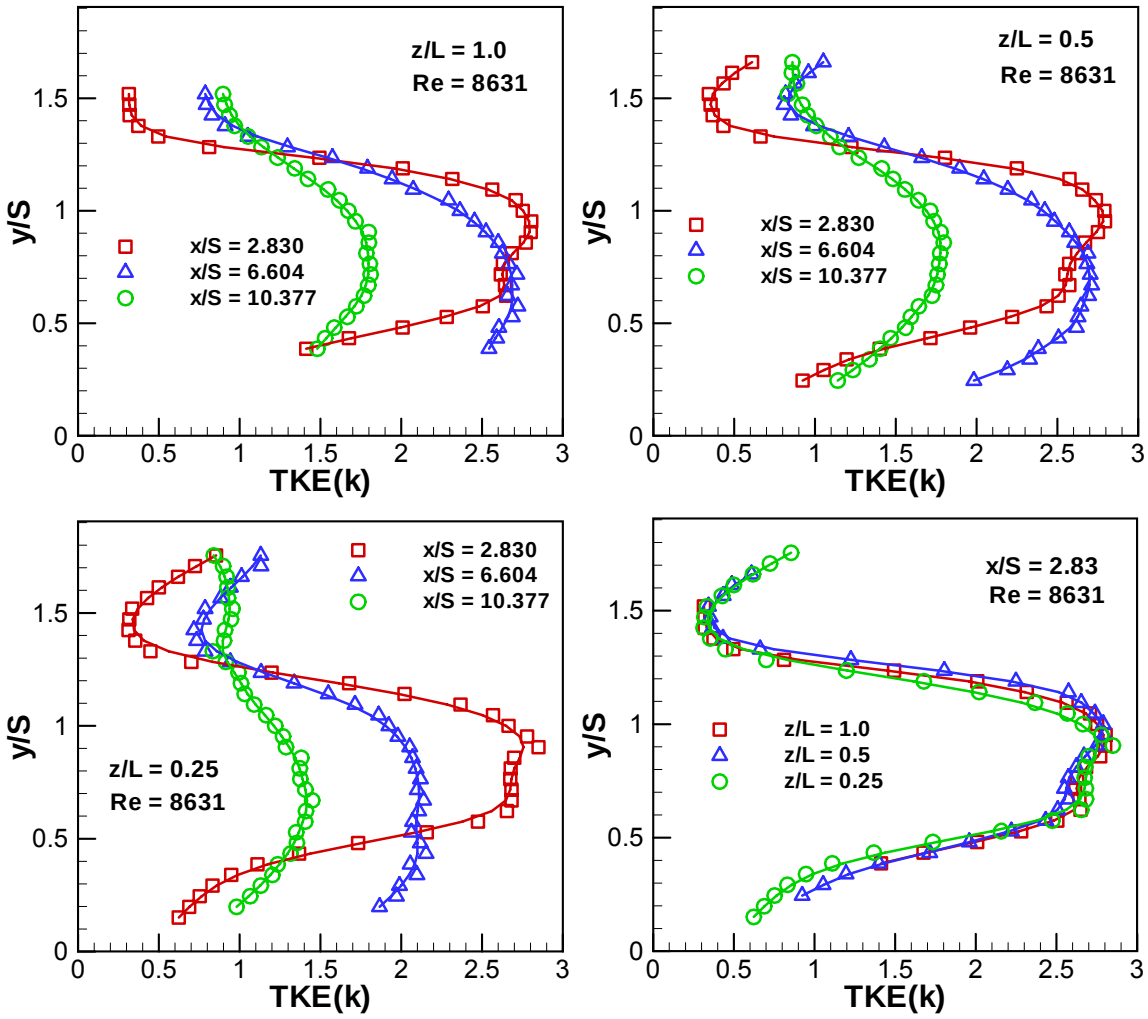

Fig. 17 Transverse distribution of the turbulent kinetic energy (*k)* at different spanwise locations

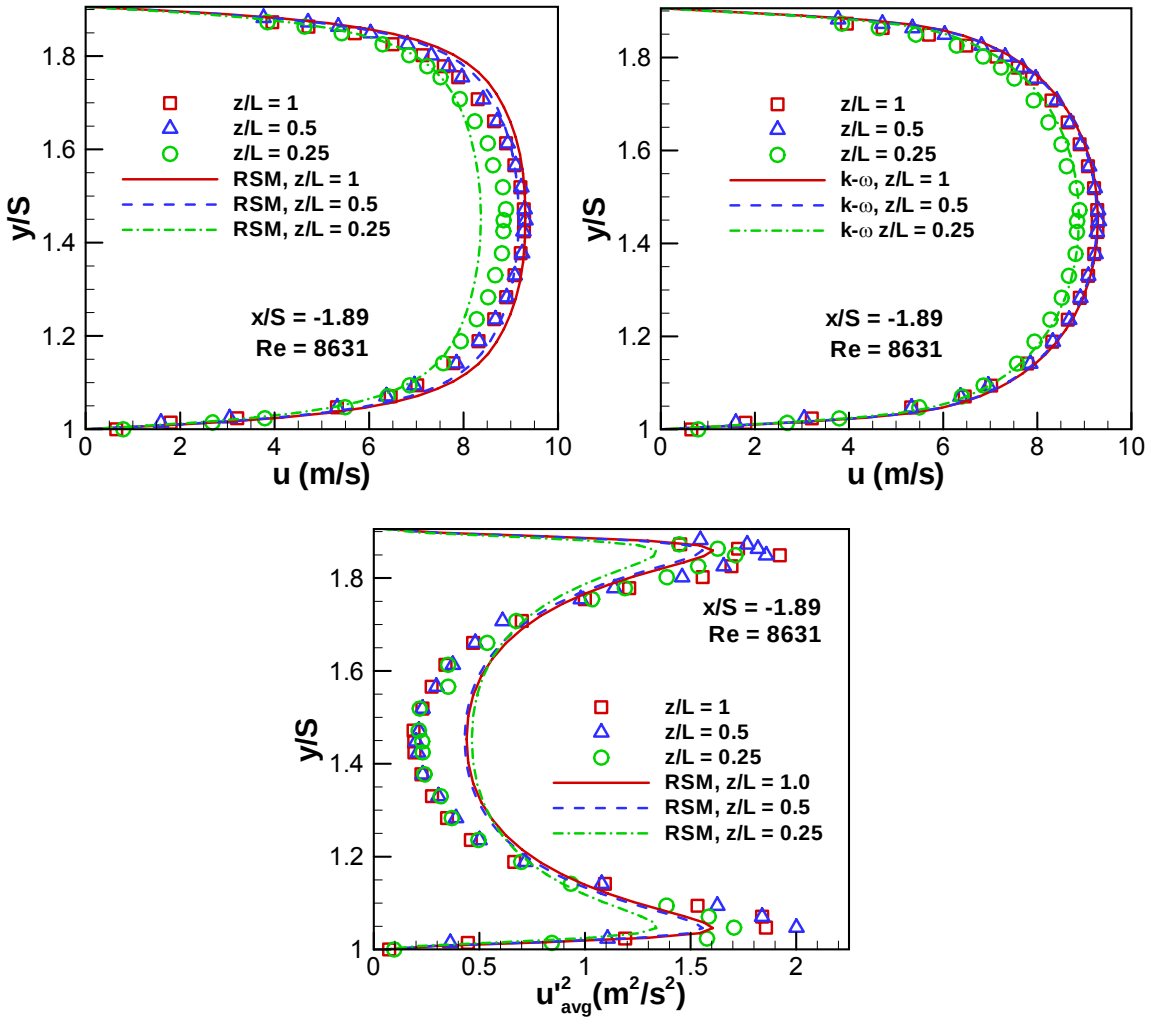

Fig. 18 Comparison of inlet mean streamwise velocity $\bar{u}$ and the streamwise component of the normal Reynolds stresses $\overline{u'^2}$ with predicted results

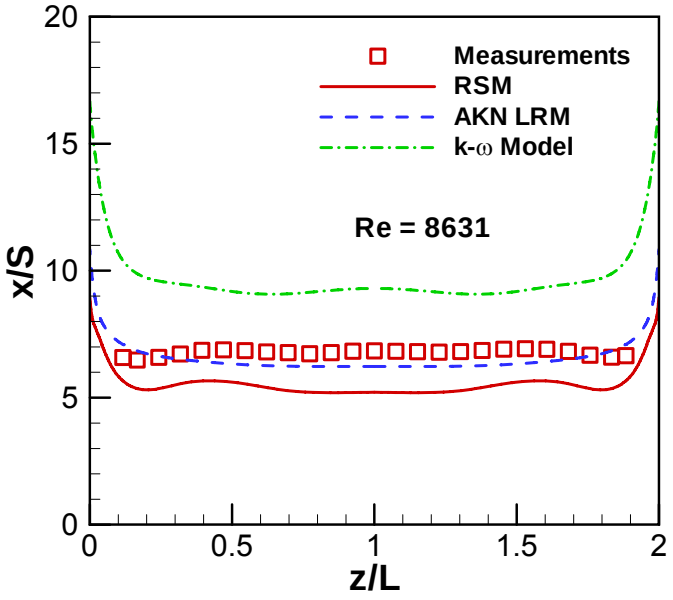

Fig. 19 Comparison of x_u-lines with predicted results

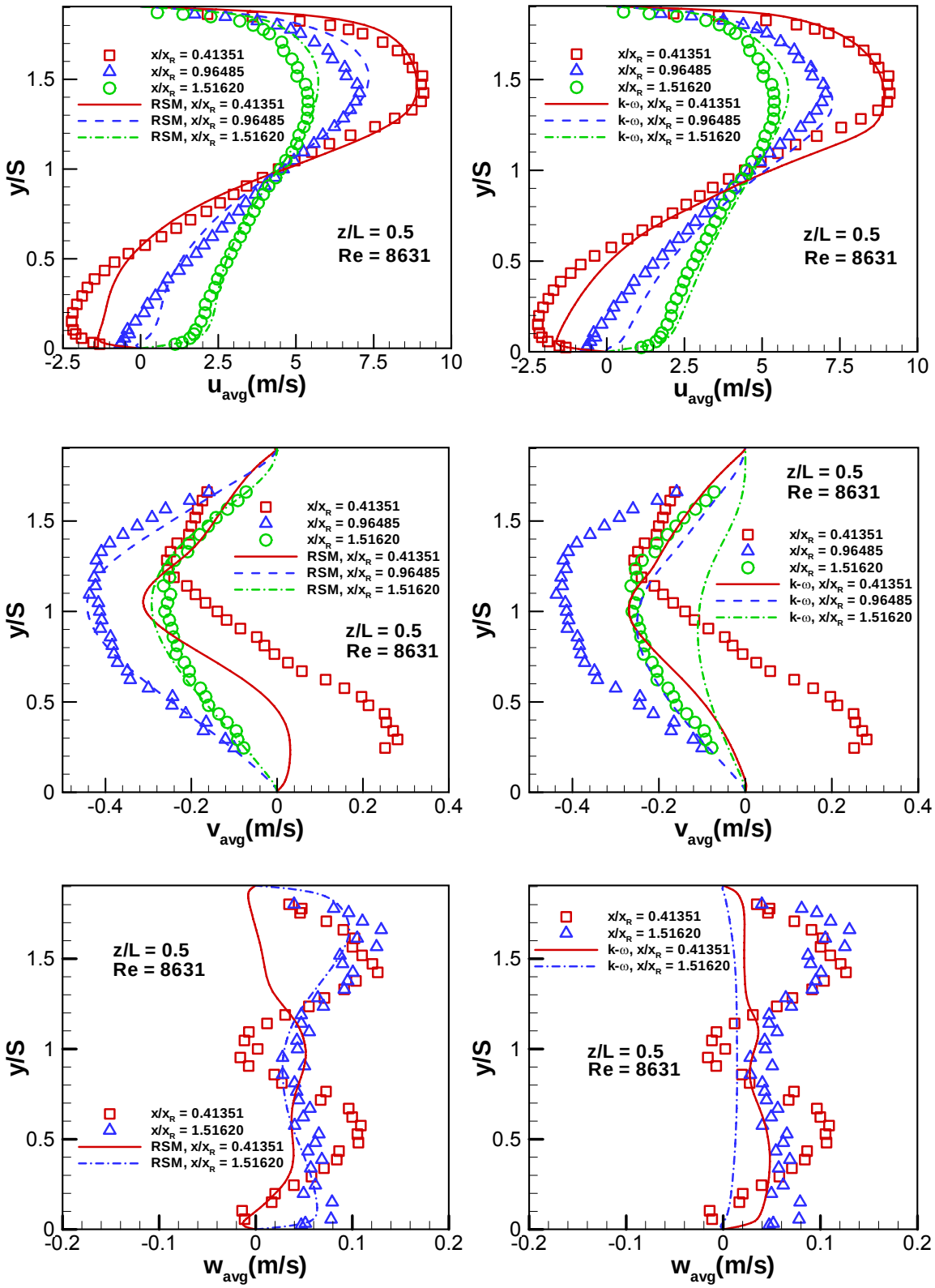

Fig. 20 Comparison of mean velocity components *u, v* and *w* with predicted results

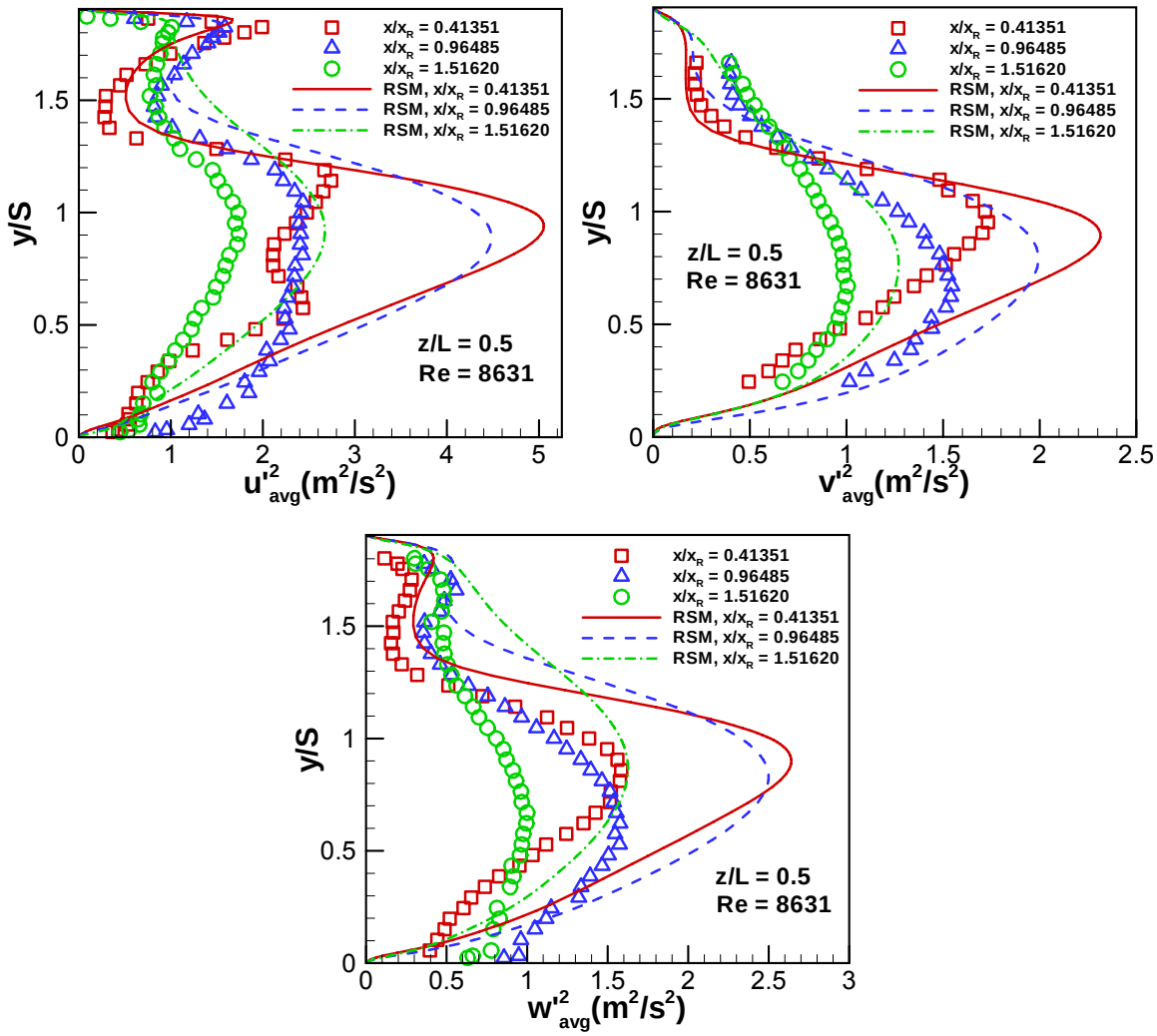

Fig. 21 Comparison of normal Reynolds stresses with predicted results

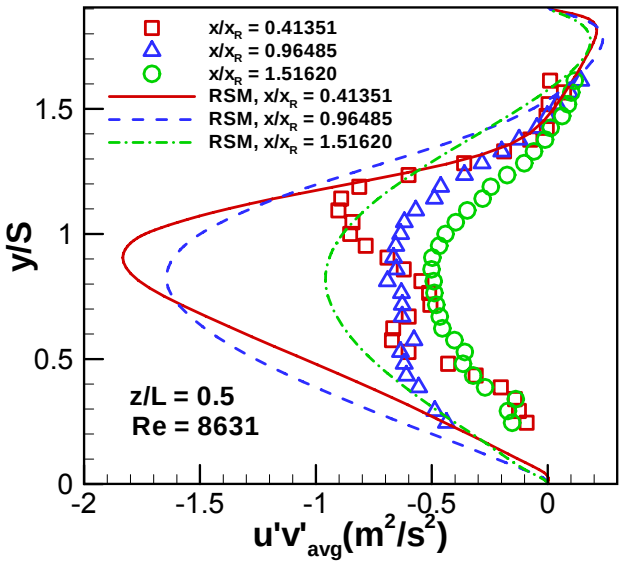

Fig. 22 Comparison of Reynolds shear stress ($\overline{u'v'}$) with predicted results

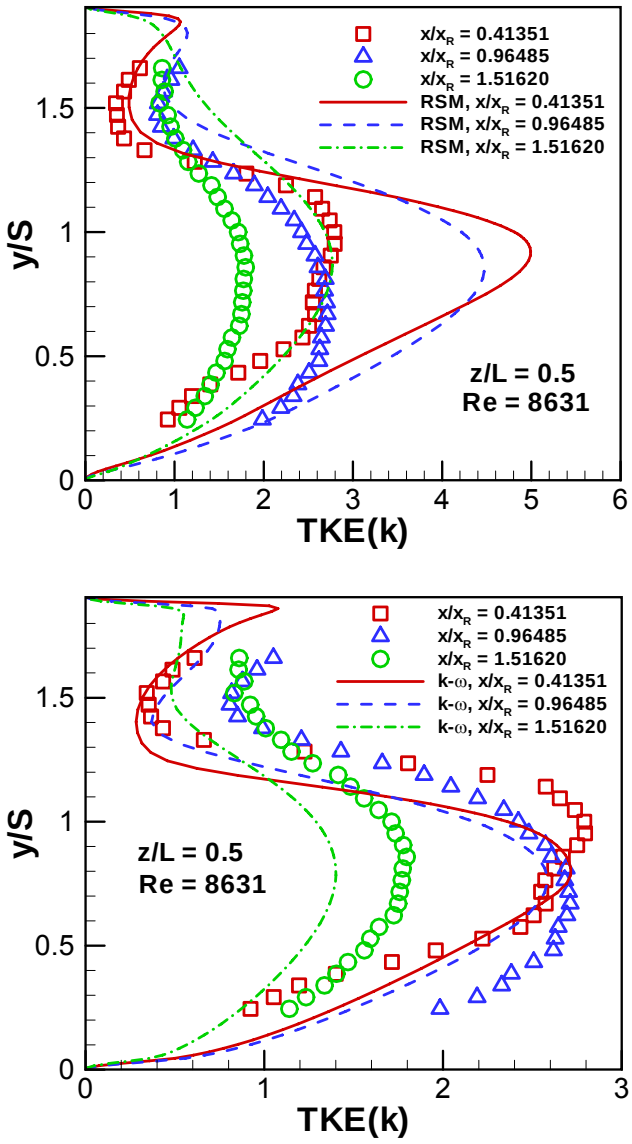

Fig. 23 Comparison of the turbulent kinetic energy (*k)* with predicted results

V. SHEAR-DRIVEN LIQUID FILM IN A DUCT

M. Thiruvengadam, B. F. Armaly and J. A. Drallmeier
Department of Mechanical and Aerospace Engineering
Missouri University of Science and Technology, Rolla, MO 65401, United States
Email: mtwv8@mst.edu, armaly@mst.edu and drallmei@mst.edu

ABSTRACT

Two-dimensional flow simulations of shear-driven thin liquid film by turbulent air flow in a duct is performed using the Reynolds Averaged Navier Stokes and continuity equations along with the Low Reynolds number k-ε turbulence model and the Volume of Fluid (VOF) model that are part of the FLUENT-CFD code. The purpose of this study is to determine the suitability of using this Code/model for predicting the measured results of Wittig et al. (1992). Both the laminar and the turbulent liquid film flow assumptions were considered in this study. Simulated results for the liquid film velocities along with the liquid film thickness as a function of inlet air velocities and liquid film flow rates are presented. Simulated results compared favorably with measured values.

Key words: Shear-Driven, Thin film, VOF model, Laminar and turbulent film, film thickness, film surface velocity.

1. INTRODUCTION

Shear-driven thin liquid film by turbulent air-flow in a duct is of considerable interest and has many engineering applications that are associated with film breakup and atomization. Such films atomize/breakup as they encounter a sudden expansion in geometry as is the case in fuel and air mixtures preparation for spark ignition engines, atomizer, refrigerant flows in evaporators, and film drag over wetted surfaces. The liquid

film that is considered in these studies can be classified as thin (~ 100 μm), and shear-driven by an adjacent gas flow. The characteristics of the film, thickness and velocity distribution prior to atomization, influence significantly the atomization/breakup process. Numerous publications have appeared in the literature on this general topic. Specifically, Wittig et al. (1992) measured and predicted the flow of shear-driven liquid film in a duct. The "rough wall" two-layer model developed for their simulation treats the film-covered wall of the duct as a rough surface with roughness being a function of the interfacial shear stress and the average liquid film thickness. The liquid film is treated as laminar boundary layer flow with linear velocity distribution and the resulting interfacial shear stress provides the coupling between the liquid (one layer) and the gas flow (second layer) through an iterative scheme. The results from this model compared favorably with measured values, but its use is limited to two-dimensional flow. Buelow et al. (2001) used FLUENT-CFD code along with the VOF model to simulate three-dimensional turbulent two-phase flow through fuel-swirler and prefilmer of a pure-airblast atomizer and their results compared favorably with measured values. Their work differs from this study by the fact that it is not a shear-driven liquid film flow and the liquid film is not bounded by a solid wall, except on the short "prefilmer".

2. PROBLEM STATEMENT AND SOLUTION PROCEDURE

Two-dimensional, steady state isothermal flow simulation of a shear-driven thin liquid film by an adjacent turbulent gas flow in a duct is performed using FLUENT-CFD code, along with the Volume of Fluid (VOF) model that has been used in simulating two-phase flow. The liquid film phase in this study is water, which is introduced through a region at the bottom wall of a horizontal duct with relatively low velocity in a direction

normal to the gas flow. The gas phase, which is air in this study, enters the duct with a relatively high velocity and has a fully-developed turbulent velocity distribution. The developing interfacial shear stress between the gas and the liquid drives the liquid in the streamwise direction, resulting in a moving thin liquid film on the bottom solid boundary of the horizontal duct. Mass and heat transfer between the liquid film and the gas is neglected in this study and a schematic of the computational domain is shown in Fig. 1.

The height "h" of the duct that is selected for this simulation is the same as the one used in the experimental study of Wittig et al. (1992) and it is fixed at "h" of 0.0043m. The other dimensions that are used in the simulation are a film injection region "L_1" of 0.0013m, a length upstream of the film injection region "L_3" of 0.02m, and a computational domain length "L_2" of 0.5m as shown in Fig. 1. The physical properties of air and liquid film (i.e. density (ρ) and dynamic viscosity (μ) are treated as constants and evaluated at the inlet temperature of T_0 = 20˚C. The fully developed turbulent inlet air flow distributions (streamwise velocity component (u), turbulent kinetic energy (k) and dissipation rate (ε)) are generated by using a separate simulation of a single-phase air flow in a duct having the same height as the experimental one. The other velocity component (v) is set to be equal to zero at that inlet section. Uniform inlet film velocity is supplied at the injection region, in the bottom wall of the duct. The no-slip boundary condition is applied to all of the solid boundaries, and fully developed flow condition is imposed at the exit section of the duct.

The VOF model has the capability of determining the position of the interface between the liquid film and the air by determining the liquid volume fraction (α_f) in each computational cell. A single set of momentum equations and turbulence model is shared

by the liquid and by the gas, and the two-phase flow is treated as quasi-single phase with variable properties. These properties, like density and viscosity, are a function of the individual properties of the gas and the liquid along with the volume fraction of the liquid in each computational cell, and are evaluated by using volume-fraction-weighted averaging method. The volume fraction of the liquid (α_f) in each computational cell is tracked throughout the computational domain during the simulation and is used to calculate the properties for that cell. The volume fraction of the liquid (α_f) in each computational cell can vary between zero and unity, and the volume fraction of the gas in each computational cell equals unity minus the volume fraction of the liquid in that cell. The AKN low Reynolds number turbulence model (1994) is used in these simulations in order to capture the velocity distribution inside the very thin liquid film. Both turbulent and laminar liquid film is considered in this study. For the case of laminar liquid film a laminar region is created by disabling the turbulent quantities. The VOF model is solved using implicit scheme along with implicit body force formulations. Second order upwind scheme is used for the volume fraction, the momentum and the turbulence scalar equations in order to improve the accuracy of the simulations. The SIMPLE algorithm is used in coupling the computations between flow field and pressure field. Description of the VOF model, the turbulence model, and the other governing equations for the velocity; volume fraction; and the quasi-single phase properties, along with the solution procedure, can be found in the FLUENT manual (2004). The problems encountered while using the VOF model for simulating interfacial boundaries between two phases with large difference in densities have been discussed by Gerlach et al. (2006).

Grid independence studies were performed for turbulent film using several grid densities and distributions as shown in table 1, and grid #1 (537 x 175) with 24 grid points inside $y^+ = 10$ region is selected as being suitable for generating grid independent results for all the cases in this study. The results in this table are for air velocity of u_{air} = 30 m/s, and film flow rate per unit width of Q_f = 0.4 cm^2/s. The convergence criterion required that the scaled residuals be smaller than 10^{-5} for all the equations.

Table 1 Results for different computational grids

Grid	*x* x *y* Grid size	First grid point distance (μm)	Rate of growth	Film thick.(h_f)(μm)	Film vel.(u_f) (m/s)
1	537 x 175	3	1.0	74.561	0.819
2	509 x 150	5	1.0	74.215	0.823
3	448 x 120	10	1.0	72.355	0.837

The liquid film interface (film thickness) is identified in this study as the location where the computational cell has a liquid volume fraction of α_f = 0.5. The results in Fig. 2 illustrate that the selection of this criterion ensures that 95% of the injected mass flow rate into the duct is captured within the film boundary in the fully developed regime. A change in this criterion for α_f between 0.1 and 0.9 results in less than 15 μm change in the film thickness. (In the figure 2, the Mass Fraction (%) is equal to $\dot{m}/\dot{m}_{fi}$ x 100, where $\dot{m}$ is equal to the film mass flow rate in the fully developed flow regime for a given interfacial volume fraction α_f criterion and $\dot{m}_{fi}$ is the injected liquid mass flow rate into the duct). The steady-state nature of this simulation does not produce the interfacial waviness/instabilities that do appear in the experimental results.

3. RESULTS AND DISCUSSION

The gravity force and the surface tension force are included in this two-dimensional simulation. But simulations were also carried out without surface tension effect and the film thickness results showed that the surface tension has no effect for this two-dimensional study. The surface tension coefficient and the contact angle will play an important role in the three-dimensional simulation of this problem where both film thickness and width are of interest. The general features of the simulated shear-driven liquid film are presented in Fig. 3 (not to scale). An overshoot develops in its thickness in the region where the film is injected but the film thickness reaches its fully developed value (constant film thickness) rapidly after that region. Results from using different criterion on α_f for determining film thickness are shown in this figure to illustrate its effect in the range between 0.1 and 0.9. Simulated film thickness and surface film velocity are presented in Figs. 4 and 5 respectively, for a fixed air velocity and different liquid film flow rates. Similarly, the same parameters are presented in Figs. 6 and 7 respectively, for a fixed liquid film flow rate and different air velocities. The results presented in Figs. 4 - 7 assume turbulent flow exist in both the liquid film and the air. Increasing the liquid film flow rate increases the film thickness and its surface velocity. Increasing the air flow rate decreases the film thickness but increases it surface velocity due to the increased interfacial shear stress that develops with increased air velocity. The film becomes fully developed within 20% of the computational length of the duct. Results similar to those in Figs. 4 - 7 are generated for different inlet air velocities and liquid film flow rates, but are not presented because they exhibit similar behavior.

Simulation results for the liquid film velocity distribution are presented for a fixed air velocity and different liquid film flow rates in Fig. 8, and for a fixed liquid film flow rate and different air velocities in Fig. 9. The no film case in Fig. 8 represents the single phase turbulent air flow and for that case the VOF multiphase model is disabled during the simulation. The interface between the liquid film and the air (film thickness) for each case is identified by an arrow in these figures, and that location is at approximately the lower edge of the knee in the curve where the velocity starts to increase at a much higher rate. A higher liquid film flow rate results in a higher film thickness and higher surface film velocity. A higher air velocity results in a smaller film thickness and higher surface film velocity. The results from using the Low Reynolds number turbulence model in simulating the turbulent liquid film flow that is shown in these figures illustrate that the turbulent liquid film velocity distribution is non-linear.

The effect of the liquid film flow rate on the air velocity distribution in the duct is presented in Fig. 10 for the case of average inlet air velocity of 30 m/s. The case for a zero liquid film flow rate (no film) is also presented in this figure for comparison. The results clearly show that the air velocity distribution is effected significantly by the presence of the liquid film. The distribution is not symmetric with respect to the center height of the duct, and the degree of asymmetry increases as the liquid film flow rate/thickness increases. The energy that is extracted from the air flow in the process of driving the liquid film decreases significantly the air velocity in the lower half of the duct, and in order to conserve its mass flow rate its velocity increases in the upper half of the duct. The maximum air velocity in the duct when the liquid film is present is higher than what develops in the duct when no liquid film is present due to the resulting

asymmetry in the velocity distribution. The maximum velocity in the duct increases as the liquid film flow rate/thickness increases as demonstrated in the figure.

4. COMPARISON WITH MEASURED RESULTS

4.1 Turbulent liquid film flow assumption

Comparisons of measured and simulated results are presented in Figs. 11 and 12 for turbulent liquid film and air flow. The simulated results for the film thickness are lower than the measured values but exhibit the same trend. The percentage difference between the predicted and measured values decreases with increasing air velocity. On the other hand, the simulated results for the liquid film surface velocity compare well with measured value. It should be noted, that the selection of a lower value for the liquid volume fraction as a criteria for locating the interface would increase the film thickness and also increase the surface film velocity. Measured surface film velocities for the case of air velocity of 90 m/s are not available for comparison with predicted values. Measured film surface velocities for the case of air velocity of 60 m/s and liquid film flow rates larger than 0.6 cm^2/s exhibit a dramatic jump. At these high air and liquid film flow rates, interface instabilities/waviness becomes so large (experimentally) to cause changes in the film flow regime and increase significantly the uncertainties in these measurements.

4.2 Laminar liquid film flow assumption

The effects of considering the liquid film flow as laminar rather than turbulent (as was done in the above paragraph), while keeping the air flow as turbulent is examined only for the air velocity case of 30 m/s. The results from such a simulation are presented (in dashed lines) in Figs. 8 and 9 and show better agreement with the measured data. The

laminar region (height above the wall) that is used in the simulation was selected (after several iterations for each liquid film flow rate) to ensure that the mixture density at the upper edge of that region, which is evaluated by using the volume-fraction-weighted averaging method, is slightly higher (less than 0.25 percent) than the air density. The turbulent kinetic energy and the turbulent dissipation rate calculations were deactivated in this laminar film region during the simulation and the liquid film thickness is determined by using the criterion for the liquid volume fraction of $\alpha_f = 0.5$ (the same criterion that was used in the turbulent liquid film flow simulation). The laminar film assumption resulted in linear velocity profile inside the liquid film region as shown in Fig. 13 but the turbulent flow assumption resulted in a non-linear velocity profile in that region. The air velocity distribution in the duct for different liquid film flow rates is presented in Fig. 14 for the case of average inlet air velocity of 30 m/s similar to the results presented in Fig 10 for turbulent liquid film. The results clearly show that the air velocity distribution is less skewed for the laminar liquid film assumption as compared with the case for turbulent liquid film assumption. The asymmetry in the distribution remains almost constant as the liquid film flow rate/thickness increases which is different than the case for turbulent liquid film assumption. The laminar liquid film assumption results in a larger film thickness and surface film velocity and seems to provide a better agreement with measured results as shown in these figures. Wittig et al. (1992) also showed in their calculations that treating the liquid film as laminar provided better agreement with measured film thickness and surface velocity than treating the film as turbulent using their two layer rough wall model in these ranges of flow conditions. This could be due to

the fact that the film remains mostly laminar and does not become turbulent due to its interactions with the turbulent gas phase flow.

5. CONCLUSIONS

The suitability of using the Volume of Fluid (VOF) model that is part of the FLUENT-CFD code for simulating shear-driven liquid film by turbulent air flow in a duct is explored in this study. Simulated results compare favorably with measured values. Increasing the liquid film flow rate increases both the film thickness and its surface velocity. Treating the liquid film flow as laminar instead of turbulent resulted in a thicker film with higher surface velocity and improves the agreement with measured results. Increasing the air flow rate decreases the film thickness but increases its surface velocity. The VOF steady-state simulation model does not predict surface instabilities that are observed experimentally and these instabilities increase significantly the experimental error and contribute to the difference between measured and predicted results. The present simulation scheme could be extended easily to simulate three-dimensional shear-driven flow.

ACKNOWLEDGEMENTS

This work has been supported in part by an NSF grant No. CTS-0352135 and by a DOE-Basic Energy Sciences grant No. DE-FG02-03ER46067.

REFERENCES

1. Abe K, Kondoh T, Nagano Y (1994). A new turbulence model for predicting fluid flow and heat transfer in separating and reattaching flows - I. Flow field calculations, Int. J. Heat Mass Transfer 37(1): 139-151.

2. Buelow PEO, Mao CP, Smith S, Bretz D (2001). Application of two-phase CFD analysis to a prefilming pure-airblast atomizer, 37th AIAA/ASME/SAE/ASEE Joint Propulsion Conference, Salt Lake City, Utah, 1-10.

3. Fluent Inc. (2004). Fluent 6.2 User's Guide.

4. Gerlach D, Tomar G, Biswas G, Durst F (2006). Comparison of volume-of-fluid methods for surface tension-dominant two-phase flows. Int. J. Heat Mass Transfer 49: 740-754.

5. Wittig S, Himmelsbach J, Noll B, Feld HJ, Samenfink W (1992). Motion and evaporation of shear-driven liquid Films in turbulent gases. J. Engineering for Gas Turbines and Power 114: 395-400.

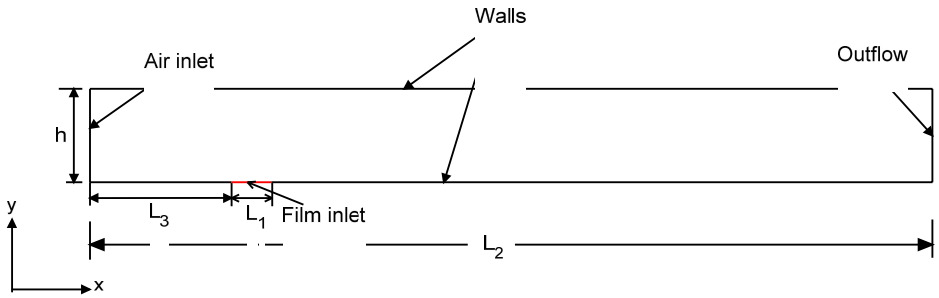

Fig. 1 Schematic of the computational domain

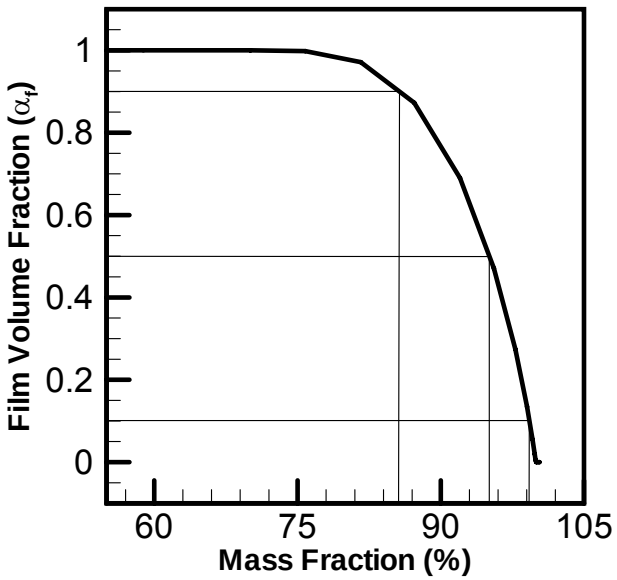

Fig. 2 Liquid mass fraction captured for a given volume fraction

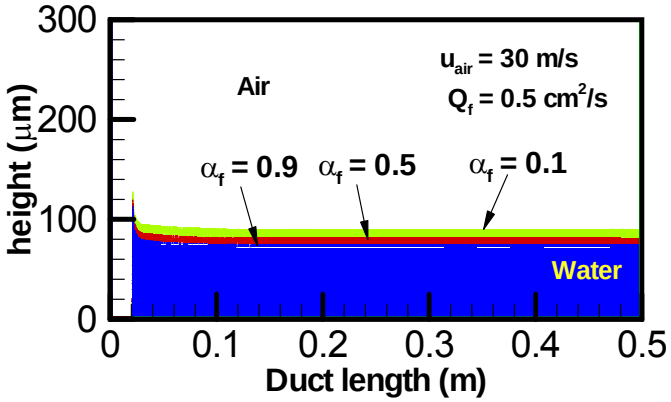

Fig. 3 General features of the flow and the interface

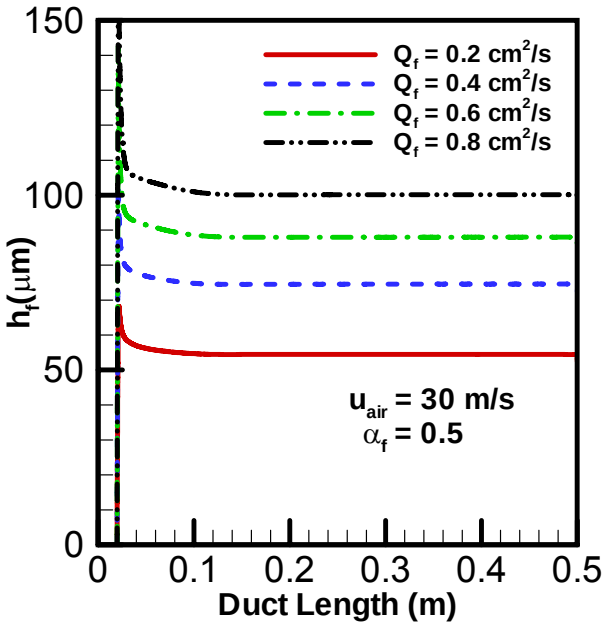

Fig. 4 Film thickness

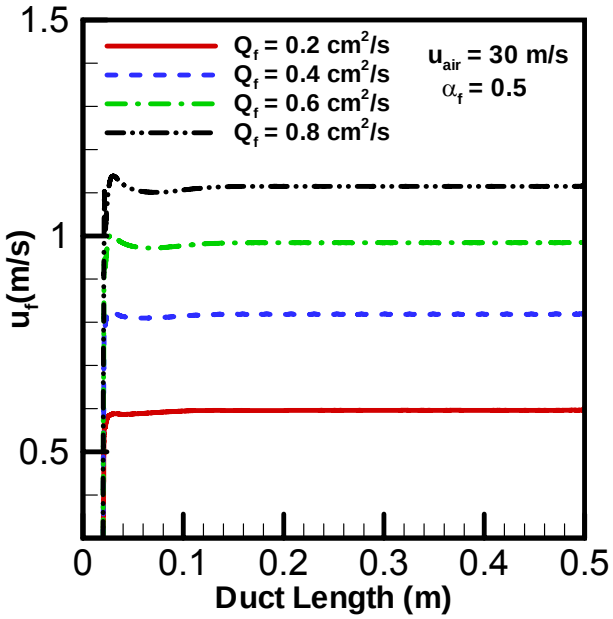

Fig. 5 Film surface velocity

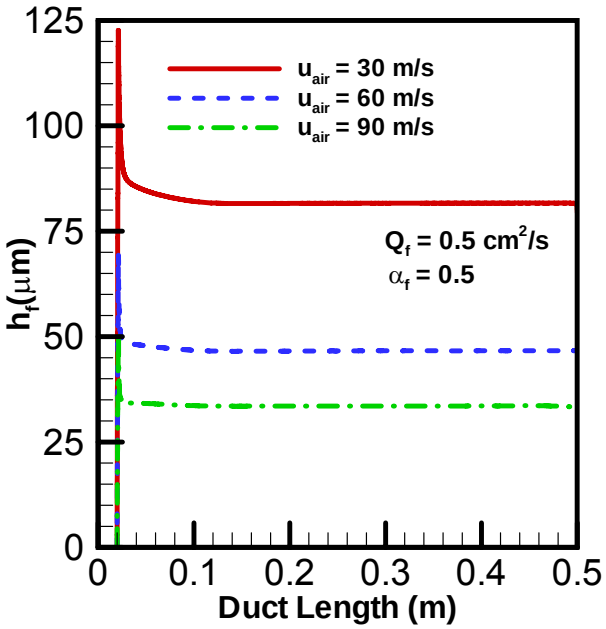

Fig. 6 Film thickness

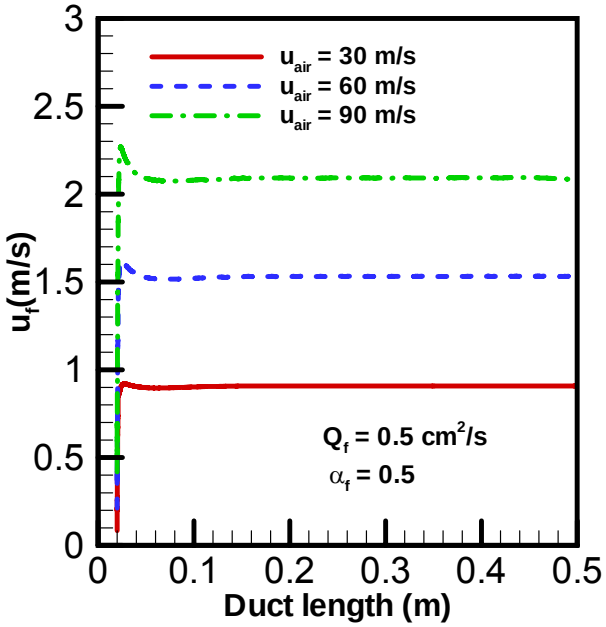

Fig. 7 Film surface velocity

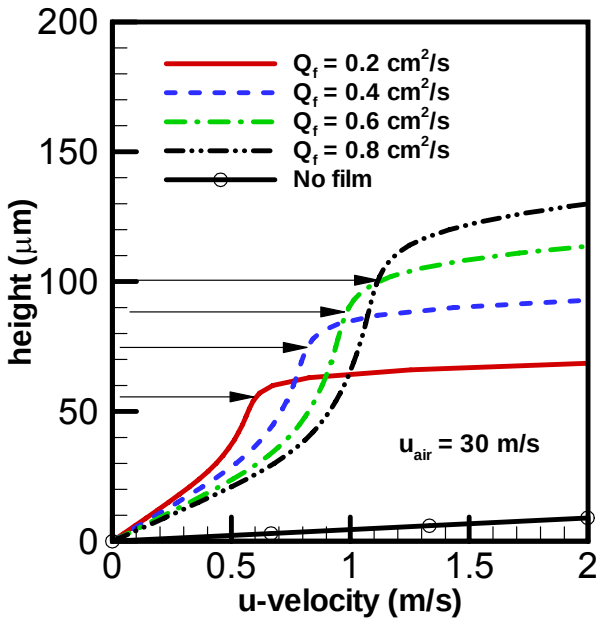

Fig. 8 Velocity distributions inside the turbulent liquid film

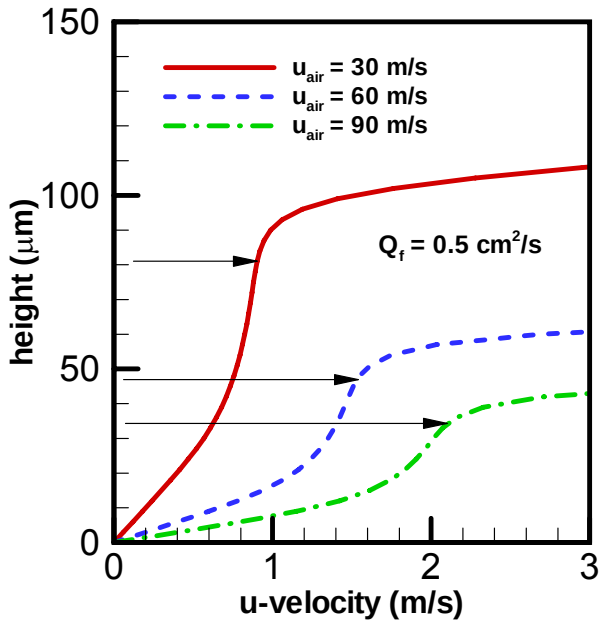

Fig. 9 Velocity distributions inside the turbulent liquid film

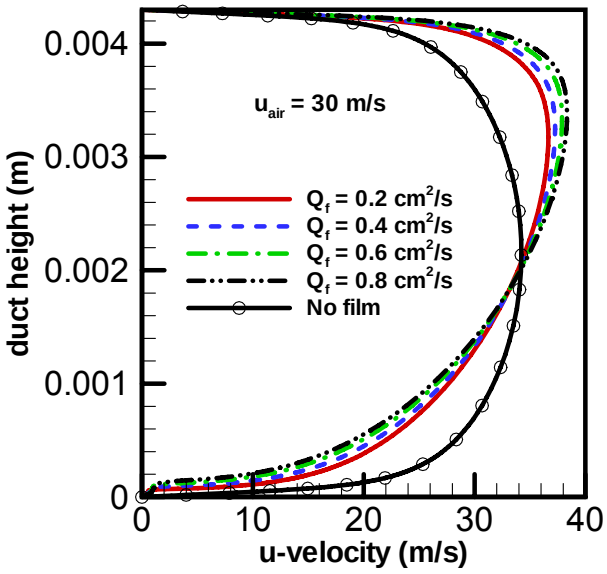

Fig. 10 Effect of film flow rate on the air velocity distribution (turbulent film)

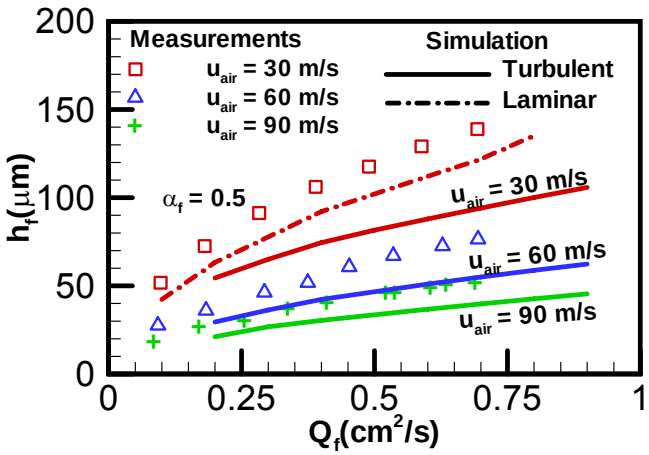

Fig. 11 Comparison of film thickness with measured results

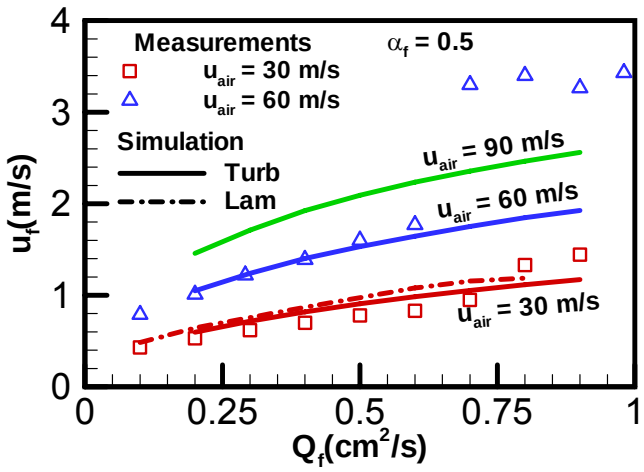

Fig. 12 Comparison of surface film velocity with measured results

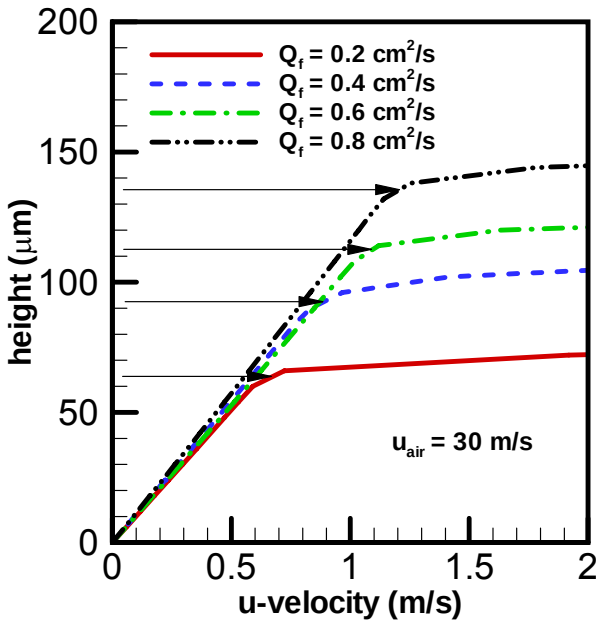

Fig. 13 Velocity distributions inside the laminar liquid film

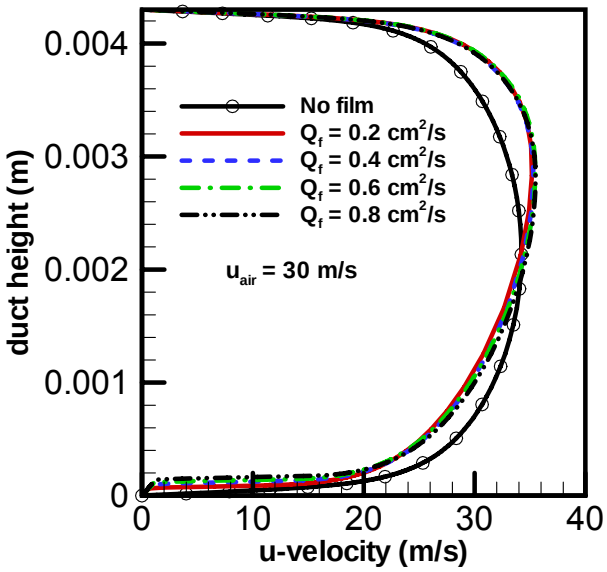

Fig. 14 Effect of film flow rate on the air velocity distribution (laminar film)

BIBLIOGRAPHY

1. Durst, F., Melling, A., and Whitelaw, J.H., 1974, "Low Reynolds Number Flow over a Plane Symmetric Sudden Expansion," J. Fluid Mech., 64, pp. 111-128.

2. Cherdron, W., Durst, F., and Whitelaw, J.H., 1978, "Asymmetric Flows and Instabilities in Symmetric Ducts with Sudden Expansions," J. Fluid Mech., 84, pp. 13-31.

3. Durst, F., Pereira, J.C.F., and Tropea, C., 1993, "The Plane Symmetric Sudden-Expansion Flow at Low Reynolds Numbers," J. Fluid Mech., 248, pp. 567-581.

4. Fearn, R.M., Mullin, T., and Cliffe, K.A., 1990, "Nonlinear Flow Phenomena in a Symmetric Sudden Expansion," J. Fluid Mech., 211, pp. 595-608.

5. Drikakis, D., 1997, "Bifurcation Phenomena in Incompressible Sudden Expansion Flows," Phys. Fluids, 9(1), pp. 76-87.

6. Hawa, T., and Rusak, Z., 2001, "The Dynamics of a Laminar Flow in a Symmetric Channel with a Sudden Expansion," J. Fluid Mech., 436, pp. 283-320.

7. Tsui, Y.Y., and Shu, S.J., 1998, "Effects of Buoyancy and Orientation on the Flow in a Duct Preceded with a Double-Step Expansion," Int. J. Heat Mass Transfer, 41, pp. 2687-2695.

8. Alimi, S.E., Orfi, J., and Nasrallah, S.B., 2005, "Buoyancy Effects on Mixed Convection Heat and Mass Transfer in a Duct with Sudden Expansions," Heat Mass Transfer, 41, pp. 559-567.

9. Nie, J.H., and Armaly, B.F., 2004, "Three-Dimensional Forced Convection in Plane Symmetric Sudden Expansion," ASME J. Heat Transfer, 126, pp. 836-839.

10. Armaly, B. F., Li, A., and Nie, J. H., 2003, "Measurements in Three-Dimensional Laminar Separated Flow," Int. J. Heat Mass Transfer, 46, pp. 3573-3582.

11. Nie, J. H., and Armaly, B. F., 2003, "Reattachment of Three-Dimensional Flow Adjacent to Backward-Facing Step," ASME J. Heat Transfer, 125, pp. 422-428.

12. Nie, J. H., and Armaly, B. F., 2004, "Convection in Laminar Three-Dimensional Separated Flow," Int. J. Heat Mass Transfer, 47, pp. 5407-5416.

13. Li, A., 2001, "Experimental and Numerical Study of Three-Dimensional Laminar Separated Flow Adjacent to Backward-Facing Step," Ph.D. thesis, University of Missouri, Rolla, MO.

14. Nie, J. H., and Armaly, B. F., 2004, "Reverse Flow Regions in Three-Dimensional Backward-Facing Step Flow," Int. J. Heat Mass Transfer, 47, pp. 4713-4720.

15. Wittig, S., Himmelsbach, J., Noll, B., Feld, H.J., and Samenfink, W., 1992, "Motion and Evaporation of Shear-Driven Liquid Films in Turbulent Gases," J. Engineering for Gas Turbines and Power, 114, pp. 395-400.

VITA

Magesh Thiruvengadam was born on July 1, 1976 in Trichy, Tamilnadu, India. He completed his higher secondary education in Chennai, India in 1994. He joined College of Engineering, Anna University in Chennai in India and obtained his Bachelor of Engineering degree in Mechanical Engineering in 1998. He then joined Indian Institute of Technology, Madras, India and obtained his M.S. by research in Mechanical Engineering in November 2001. Mr. Thiruvengadam later enrolled for his Ph.D. in Mechanical Engineering at University of Nevada Las Vegas in August 2003 and transferred to Missouri S&T in January 2004 to continue his Ph.D. degree in Mechanical Engineering. He has held the positions of Graduate Research Assistant and Graduate Teaching Assistant since January 2004 at Missouri S&T in the Department of Mechanical and Aerospace Engineering. He received his Ph.D. degree in December 2008.